12-2016

Optimal Grading for Strength and Functionality of Parts Made of Interpenetrating Polymer Networks: Load Capacity Enhancement

Zhong Chen
University of Nebraska-Lincoln, zhongchen128@gmail.com

Optimal Grading for Strength and Functionality of Parts Made of Interpenetrating Polymer Networks: Load Capacity Enhancement

by

Zhong Chen

A DISSERTATION

Presented to the Faculty of
The Graduate College at the University of Nebraska
In Partial Fulfillment of Requirements
For the Degree of Doctor of Philosophy

Major: Engineering

Under the Supervision of Professor Mehrdad Negahban

Lincoln, Nebraska
December, 2016

Optimal Grading for Strength and Functionality of Parts Made of Interpenetrating Polymer Networks: Load Capacity Enhancement

Zhong Chen, Ph.D.

University of Nebraska, 2016

Advisor: Mehrdad Negahban

Uniform parts with stress concentrations or singularities are prone to failure under relatively small loads, which motivates researchers to seek methods to enhance the strength of these parts. This dissertation studies the optimization of material grading to design parts made of functionally graded interpenetrating polymer networks (FG-IPNs) to improve their load capacity.

An acrylate/epoxy IPN with variations of elastic Young's modulus, Poisson's ratio, and ultimate stress at failure is used for optimization of a plate with stress concentration. The grading is optimized by attaching the finite element method (FEM) solver to a general purpose bound-constrained optimizer. Two examples, a plate with a hole and a bent bracket, show more than 100% improvement in the part's load capacity when compared to the uniform IPNs.

Parts with stress singularities are studied using a PMMA/PU IPN system. For this system, we have the elastic modulus and the critical stress intensity factor K_{IC} as a function of the concentration of the components. A material mesh is utilized to control the grading near the crack tip and uniform material is assumed outside the tip area. The displacement correlation technique (DCT) is used to calculate stress intensity factors and the maximum hoop stress criterion is selected as the fracture criterion. Parts with edge cracks, interior cracks and interacting cracks under tension are considered. For the PMMA/PU IPN system, improvements in load capacity in the order of one hundred percent were commonly obtained through grading the region around the crack tip, compared to both optimal uniform plates, and plates with simple toughening of the region around the crack.

In addition, in FEM modelling of FGM part with graded elements, the polynomial interpolations used in such elements can be prone to oscillations that can result in regions of negative elastic modulus, even with only positive nodal values of elastic moduli. The result of these negative modulus regions, even if the region is small, can be unexpected singularities in the solution. To avoid this potential problem, conditions for robust higher order materially graded elements were developed.

Acknowledgements

First, I would like to thank my advisor, Dr. Negahban, who kept leading me on the way of research in the past four years since I was a complete novice. He helped me not only experience the excitement and pleasure of discovery, but also understand the perspiration and hard work required to do academic research. It happened countless times that he explained the concepts in computational mechanics to me, noted the mistakes I had in my presentations, paper drafts and programming codes, with enormous patience, and gave me valuable advices when I got stuck or felt lost in the research maze. I believe what he taught me has become a seed inside my heart and will exert an influence in all my research carrier. I am very lucky to have a good advisor like him.

Sincere thanks should also be given to my teachers, colleagues and friends. Courses taught by Dr. Turner, Dr. Yang, Dr. Bobaru, Dr. Reid and others have helped build my solid background in my major and broadened my view. Their knowledges, passions, and personalities left strong impressions on me. Cooperation with colleagues in my research group has always been a pleasant time. I learned much from Mr. Wenlong Li, Mr. Zesheng Zhang, Mr. Walker Dimon, Mr. Evan Schwahn, Ms. Emily Bobo, Ms. Marzieh Bakhtiary, Mr. John Jasa, Dr. Nicolas Delpouve, Mr. Leandro Castro, Dr. Flavio Souza, Mr. Andrew MacKrell and others. Other friends also helped me a lot in my academic and everyday life. Their names are too many to list here but I will remember each single forever.

Without my family’s encourage and support, I don’t think I could have suceeded. Although my parents, Shengwu Chen and Yuzhi Li, never got a chance to go to college, they believe knowledge is the most valuable thing to pursue and it can change one’s life and even the world. My sister, Qiong Chen, always gave me confidence when I felt down. The smiles of my niece, Jiayun Zou, inspired my hope so many times. I am very happy and proud to be born in such a family full of love and kindness.

Last but not least, I would like to acknowledge the support of the China Scholarship Council (CSC) program, which helps many Chinese students travel to and learn from others in the whole world.

Table of Contents

List of Figures

List of Tables

Chapter 1 Introduction

1.1 General introduction

There are many examples in nature that illustrate the advantage of tools made to have varying material properties in space. For example, a hard squid beak is connected and manipulated by its soft body through a gradually hardening tissue that allows an otherwise soft creature to have and manipulate a hard tool [1]. Such examples of functional grading are abundant in nature and seem to be more the norm than the exception as one sees them in teeth structure, in most bones, in plant stems such as bamboo, etc. [2]. It would be hard to imagine how some of these solutions would come about without material grading and how effective other solutions would be in creating the vast variety of living creatures existing today. It seems natural then to wonder how grading can improve many of our current engineering solutions [3].

Very similar to shape optimization [4-7], given a finite set of available materials, grading provides one additional dimension in ideas and tools for designing parts. Grading in a part can be manipulated to obtain a better functioning solution. Such a part is considered a Functionally Graded Material (FGM) part. With recent progress in manufacturing technology, humans are now designing and building FGMs to take advantage of using functionality that can result from variation of the distribution of properties [3-6]. As will be shown, real solutions exist that manipulate grading to achieve parts that function substantially better than any uniform part made from the same material system. If these ideas and results can be implemented, such as by 3D printing as shown

by Bartlett et al. [8], Shin et al. [9], Shah et al. [10], Mahamood et al. [11], Carvalho et al. [12], and Li et al. [13], one could see hundreds of percent improvement in functionality and/or gain substantial weight saving.

The optimal grading of a part is directly controlled by the material grading options, which can be vastly different for different material systems and grading methods. One can use many different methods to get grading ranging from simple heat treatments [14] to mixing and sintering [15-17] and controlling reinforcements [12]. One can also grade different properties to achieve thermal, mechanical, electrical, magnetic and other gradients. In this thesis we focus on mechanical grading achieved through varying the component fraction of interpenetrating polymer network (IPN) systems [18-24]. As the name suggests, IPNs are constructed from growing two or more polymer networks together such that they are entangled in space. This close physical proximity of the networks allows one to get properties that are different from those expressed by the individual networks. The fraction of each component can be used to vary properties of the material and its variation in space can produce a controlled grading [3]. This particular solution for grading allows the variation to be at the molecular network level, which is on the nanometer scale for many IPN systems. In addition, this technology has the potential for implementation in 3D printing for obtaining arbitrary grading through controlled stereolithography [13, 25].

Functionally graded IPNs (FG-IPNs) have been the focus of many publications. For example, Lyudmyla et al. [26] synthetized semi-IPN materials that have spatially varying damping obtained through control of the fraction of PHEMA, Mallikarjuna et al.

[27] made IPN hydrogel membranes for controlled release of anticancer drugs by using variation of the fraction of gelatin. Esen et al. [28] obtained controlled and patterned variation of refractive index across a lens surface via the use of gradient IPNs. Li et al. [13] show controlled continuous grading in stereolithography of acrylate/epoxy systems showing two orders of magnitude change in properties. Inspired by the possibility to print prescribed grading, this dissertation considers the problem of finding the optimized grading to print. In particular, optimization of the FG-IPN distribution of a part is considered with the goal of obtaining the largest load capacity. Two different classes of problems are studied. One is for parts with stress concentration, and the other is for parts with single or multiple cracks. In each case a different strategy is developed to find the optimal FG-IPN grading and the results show substantial improvements of load capacity directly resulting from the grading.

1.2 Outline

Chapter 2 discusses the concept of FGMs, including its definition, distinguishing features, research history, fabrication methods and applications.

Chapter 3 discusses IPNs, contains its definition, properties, brief history, classification, and instances in different application areas.

Chapter 4 focuses on modelling of FGMs. It discusses parameterization of the different types of the material and methods to model its grading in space. The former uses modeling of experimental results or componential multi-scaling to parameterize the macroscopic properties. The latter models the response of an FGM part based on the

FGM properties at all the control points, which are adopted to describe the material variation of the part.

Chapter 5 develops the conditions for robust higher order materially graded elements using macroscopic modelling of FGMs in FEM analysis. Polynomial interpolations used for interpolation of properties in FEM modeling of grading can be prone to oscillations that can result in regions of negative elastic modulus in the element, even with only positive nodal values of elastic moduli. The result of these negative modulus regions can be unexpected singularities in the solution. In this chapter, we demonstrate the issue using three-node quadratic Lagrange interpolations of material grading in otherwise isoparametric p-type elements and show how to avoid this problem.

Chapter 6 looks into optimization of material grading to design parts with substantially improved load capacity by optimizing FG-IPN structure. This is done in the context of acrylate/epoxy IPNs. The epoxy fraction of the acrylate/epoxy IPNs controls both rigidity and the strength at failure. This fraction is grading over a part to obtain the grading with optimal load capacity. These gradings show substantial improvements over the best associated uniform IPN. The optimization of the grading was achieved by attaching a customized higher-order (p-type) finite element method (FEM) solver to a general purpose bound-constrained optimizer. The FEM solver used grading-enabled elements based on interpolation of nodal properties. Linear scaling of the solution for each selected material grading was used in the optimization algorithm to obtain the load capacity at each optimization step from a single FEM solution. Demonstrations using a characterized acrylate/epoxy IPN system are given showing a potential doubling of the load capacity for a plate with a hole and for an L-shaped bracket.

Chapter 7 investigates functional grading around the crack tip to improve the load capacity of IPN parts made of poly(methyl methacrylate) (PMMA) and polyurethane (PU). This is achieved by combining the displacement correlation technique (DCT) method for calculating stress intensity factors from FEM solutions, development of an Abaqus user material subroutine (UMAT) to directly introduce grading into the Abaqus FEM solver, and linear scaling to reduce the number of calculation. This combination allowed efficient use of a bound-constrained optimization program to study the effect of optimized functionally grading around crack tips in edge, internal and interacting edge cracks in plates under tension. In the context of the PMMA/PU IPN system, the FG-IPNs obtained through optimization showed substantially improved load capacity compared to both optimal uniform plates, and plates with simple toughening of the region around the crack.

Chapter 8 summarizes the dissertation and discusses the potential projects in the next few years based on or related to the current work.

Chapter 2 Functionally Graded Material (FGM)

2.1 Background

The term Functionally Graded Material (FGM) was first devised in 1986 after the fabrication of a high pressure thrust chamber using the cold isostatic forming method based on powder metallurgy [29]. Since then, FGM has been a major topic of discussion and study. Owing to gradually changing properties without introducing discontinuous interfaces, FGM parts can show much better performance compared to uniform or layered parts. Many designs using the FGM concept are inspired by the architecture of graded structures seen in living bodies. After billions of years of evolution, living organisms have successfully formed optimally graded structures designed to accommodate survival in complex environments. For instance, graded distribution of fibrous tissue, porosity and graded texture can gradually increase a tissue's strength and protect it against breakdown. The better performance of FGM parts has motivated interest of researchers and resulted in the study of the fabrication methods, applications, modelling methods and optimization of FGM parts, which may bring benefits to of human life and protect the environment by better using our resources.

2.2 FGM process and fabrication

Fabrication methods for constructing FGM parts have been a subject of study for years and novel methods are being developed continuously [30]. So far, based on when and how the material grading is introduced, most popular fabrication methods can be categorized into bulk, layer, preform, melt processing and advanced manufacturing techniques, each of which will be discussed in detail in the following sub-sections.

2.2.1 Bulk processing

Bulk processing adopts the methods that initially create a bulk material to grade porosity, composition, or phase configuration. This can be accomplished through forming of stacks of powder, fibers, or sheets under gravity or by centrifugal forces based on the density difference of the components, or in pressure induced flow. The stacks are usually then strengthened either by pore elimination or infiltration.

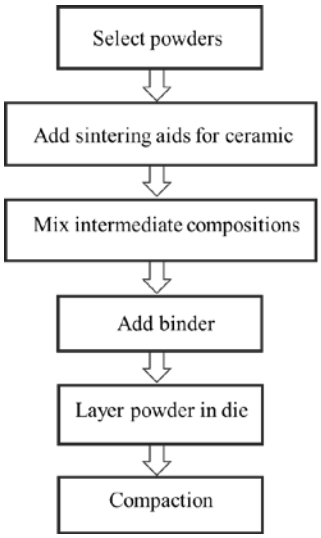

Figure 2.1 Flow chart of power stacking process to make FGM

The bulk processing of FGMs by powder stacking involves the following three steps if we take metal/ceramic FGM as an example. First, one determines the optimum distribution of the metal/ceramic composition for the FGM part. Second, one stacks the mixed metal/ceramic powder continuously according to the predetermined spatial distribution of the composition. Finally, one consolidates the powder stack [31]. FGM parts with a compositional gradient can be produced from powder that consists of at least two powder species with different chemical compositions. The chemical compositions of

the two pure powders are considered to stay unchanged after being mixed with defined volume ratios. To obtain a stable and smooth compositional gradients, two different powders are distributed in the FGM component in volume ratios with opposite gradients of the same magnitude. The controllable minimum size of the spatial distribution of the FGM depends on both the particle size of the mixed powders and the method of powder stacking. These steps are explained in detail in Fig. 2.1. The layer-by-layer stacking method enables a controllable size of 0.2 mm [32]. To obtain FGM components with density gradients, mixtures of two or more powders that fill the space in different ways can be chosen as ingredients.

Powder stacking by sedimentation processes can also form FGMs. In such processes, a powder or fiber stack is formed after removing the liquid. The conventional sedimentation method depends only on the force of gravity causing particles with different sizes, shapes, and densities to settle at different speeds to form graded materials. Now it is possible to control the sedimentation rates of different phases regardless of their relative particle size or density. If the sensitivity to the addition of agglomerating additives in the solvent is different for particles of different phases, then it is possible to control agglomeration by controlling the addition of such additives. When the sedimentation process was tested with a nickel aluminide/alumina ($NiAl/Al_2O_3$) powder mixture in a hydrophilic methanol solution, there was an obvious increase of the settling speed of the NiAl because of the presence of aqueous capillary bridges [33]. Researchers were able to eliminate phase separation during multi-compositional multilayer formation in spite of considerable differences in powder density and morphology. Variation of the initial alumina particle size also allowed for significant control of the final microstructure.

Characterization of composite mechanical properties was also carried out to verify the density and compositional gradients.

2.2.2 Layer processing

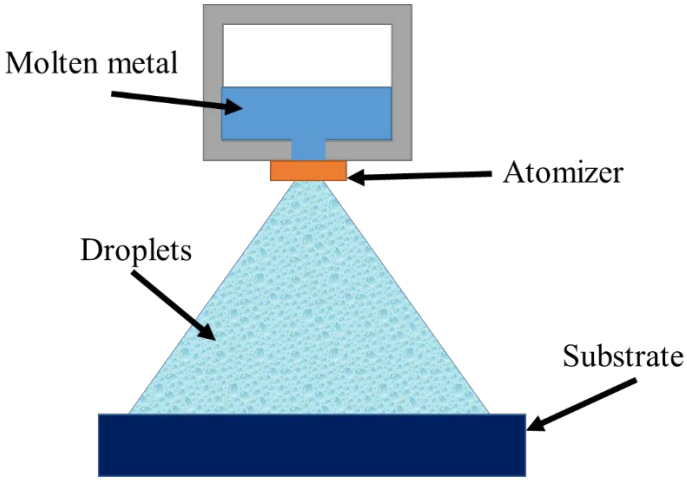

Figure 2.2 Spray forming process

Spray forming is an example of layer processing as displayed in Fig. 2.2. Initially, a metallic melt is atomized into a spray of small droplets, typically in the size of 100 μm. When the spray of such droplets in a partially liquid state is directed toward the substrate, the process is named spray forming [34]. Fine reinforcement particles, such as SiC or $A1_2O_3$, can be added either to the initial metal or to the spray. By continuously varying the quantity of the reinforcing particles added to the spray, well-designed FGM structures can be produced. Materials that can be spray formed successfully are those that are relatively unreactive and can be melted.

Deposition processes based on atomistic transport can also create FGMs. This can be widely utilized in coating a substrate, which is mainly used for protecting the substrate from oxidation and wear or preventing heat flowing in. A functional capability can be

added to the substrate by the coating layer itself or by the combined effect of both the coating and the substrate. Additional functions can be obtained with coatings that have different electric or magnetic properties. Thin layers in the nanometer range are usually deposited by atomistic transport processes through diffusion in the solid state, the liquid phase, or the vapor phase. To produce thicker coatings, higher deposition rates and thus lower costs are needed. They can be achieved by mechanical deposition processes that include microlamination, cladding, and spray deposition. Thin solid or liquid reaction layers also can be generated due to interdiffusion when two bulk materials with different compositions contact each other. The gradients can be controlled by the system and the processing parameters. Short processing time can produce transition layers, while longer processing time can result in the formation of graded bulk materials. Deposition processes based on atomistic transport are basically categorized into three kinds: those based on vapor transport, on diffusion in the solid or liquid states, and on electromigration processes.

2.2.3 Preform processing

Some preforms with determined shape or structures that do not contain gradients initially can be graded by preform processing with little or no change of the shape. One group of methods uses traditional transport mechanisms to create gradients in materials. For example, heat and mass diffusion has been used for years to create gradients in metals [35]. A second group of methods is based on the application of external stationary fields. For example, electrical fields can produce graded porosity when a porous preform is electrolytically dissolved, and a thermal gradient fields can be applied to sinter porous preforms to obtain graded densities. For graded preforms, preform processing can also be

utilized to enhance or reduce the grading effect. The preforms can be porous or dense, or may consist of homogeneous bulk materials or layers.

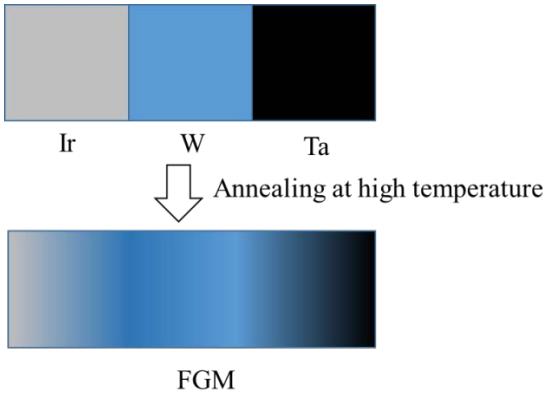

Figure 2.3 Solid state diffusion processing to make FGM

Solid state diffusion is one kind of preform processing methods to obtain FGMs. For instance, an iridium/tungsten/ tantalum graded-structure emitter has been successfully produced as illustrated in Fig.2.3 [36]. Tungsten was inserted as the intermediate layer between iridium and tantalum using hot isostatic pressing. After annealing at high temperature, the graded intermediate layer was formed. This structure was selected to enhance the thermal stability of the emitter because iridium exhibits excellent thermionic electron emission characteristics in a cesium plasma converter, owing to its low work function in cesium vapor. Thermal stresses are reduced due to graded-composition of the iridium/tungsten/tantalum system in the simulated model.

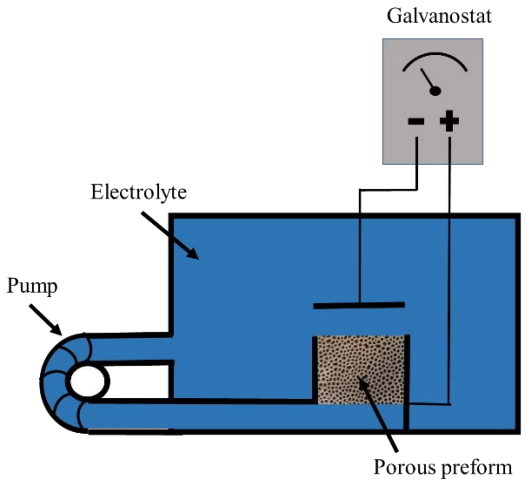

Figure 2.4 Fabrication of FGM from preform by electric field

A processing route using electric fields to manufacture FGMs from preform in chemical composition is presented in Fig. 2.4 [37]. As the potentials are usually position dependent, the electrochemical reaction will have different rates at different positions inside the porous electrode. This can cause the pores to be graded and another component can be infiltrated to make FGM. The method allows flexible control of the grading by adjusting experimental parameters, such as current density, electrode and electrolyte resistivity, and geometrical factors. Relevant electrode kinetics can be described by a macroscopic model which provides a prediction for the grading. Tungsten/copper graded materials with different variation profiles were produced and a comparison of the experiment with the model was accomplished.

A technique that fabricates a magnetically graded material by plastic deformation was also studied [38]. An initially wedge-shaped 304 stainless steel was rolled into a rectangular cross section. The saturation magnetization curve as a function of rolling ratio was found to have a positive curvature so the saturation magnetization could be

controlled to vary linearly as a function of distance. Furthermore, it was found that the hardness also varied gradually in the deformed specimen. This means the technique can fabricate an FGM that varies with space not only magnetically but also mechanically.

2.2.4 Melt processing

Melt processing is a method to form FGM parts when the different phases of the FGM part have considerably different densities. This process can happen under gravity or centrifugal forces. It is not widely used due to two shortcomings. Many phases in the molten state may be incompatible and it can be difficult to control the formation of extended compositional gradients in such melts. Gradual phase separation under normal or enhanced gravity can be similar to sedimentation. Mixtures of phases with considerably different densities may fall apart under normal gravity when kinetic conditions allow the heavier phases to settle first [39]. Settling under gravity can resemble powder settling and stacking from aqueous and non-aqueous particle dispersions.

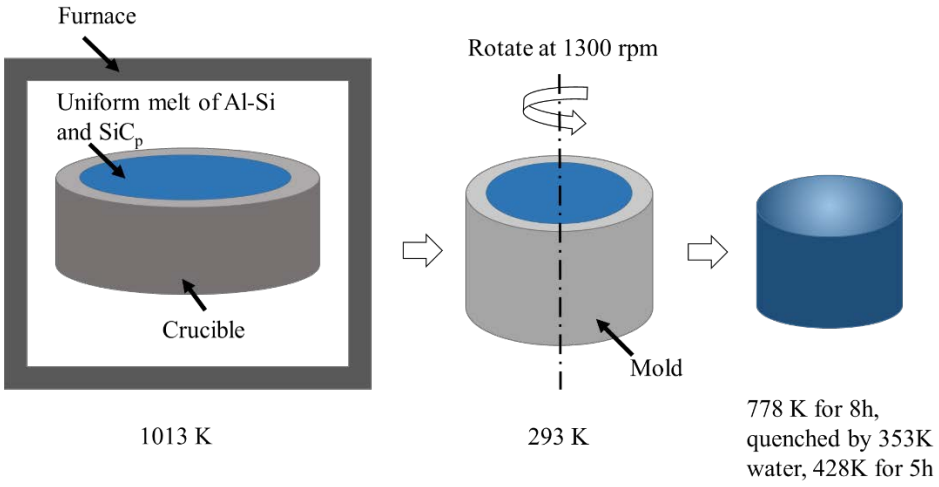

Figure 2.5 The melt processing of A319 Aluminum FGM with SiC_p reinforcements under centrifugal force

The melt processing of A319 Aluminum functionally graded metal matrix composites with 10 and 15 wt % SiC_p reinforcements under centrifugal force was studied and is displayed in Fig. 2.5 [40]. The liquid stir casting method was used for composite melt preparation followed by FGM formation by the vertical centrifugal casting method. The mold preheating temperature was 523 K, melt pouring temperature was 1013 K, and mold rotation speed was 1300 rpm. Heat treatment was also accomplished. The study analyzed the distribution and concentration of reinforcement particles in the radial direction of the FGM disk, and the effects of grading on density, hardness, mechanical strength, the variation in coefficient of thermal expansion and the wear resistance properties at different zones. Matrix-rich inner, transition, particles-rich outer, and chill zone of a few millimeters thick at the outer most periphery of the casting were formed. The mechanical characterization described enhanced properties for the particle-rich zone. The hardness showed a graded nature in correlation with particle concentration and a maximum hardness was obtained at the particle-rich region. The wear resistance was also

found highest and coefficient of thermal expansion lowest at the particle-rich zone of the FGM.

2.2.5 Advanced manufacturing techniques (Rapid prototyping)

In recent years, the rapid prototyping (RP) technology has been increasingly used in FGM fabrications. The technology is also called layer-based manufacturing or free-form fabrication. The driver is that RP, based on layer-based slicing and additive processes, is flexible to make various geometries with complex material heterogeneities [41-43]. A general RP machine to manufacture FGMs is shown in Fig. 2.6. Most RP machines to manufacture FGMs are in this form. Some may contain three components and some may not contain the laser transmitter, depending on what materials and methods they are using.

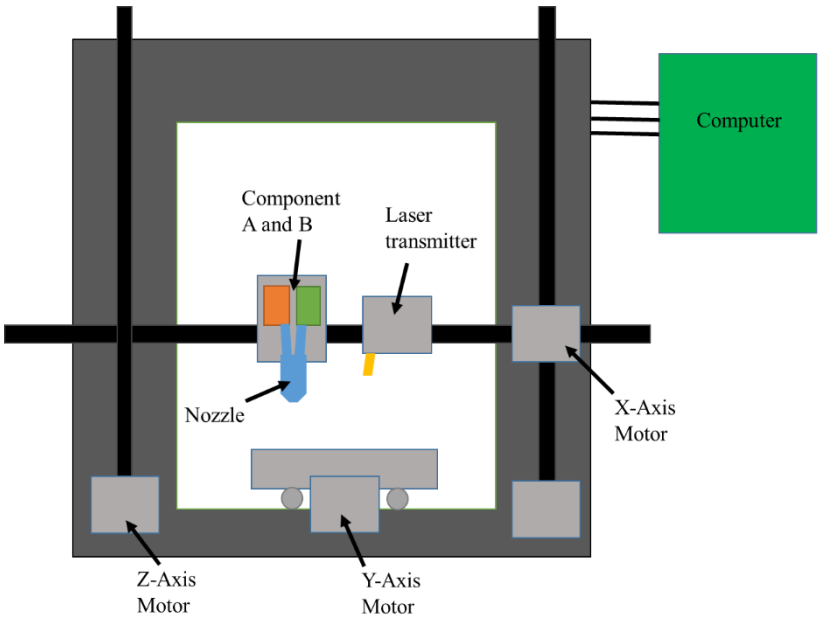

Figure 2.6 A general RP machine to manufacture FGMs.

Composition variations of different types were produced by means of a repetitive deposition process to manufacture FGMs from stainless steel 316L and stellite grade 12 by Yakovlev et al. [41]. Each layer of about 30μm thickness was created by coaxial powder injection into the working zone along with the laser beam through a specially designed nozzle. Pulse-periodic Nd:YAG with wavelength 1.06 μm was used as the laser source since it provided good beam quality for developing FGM components. The technique allowed predefined composition variations by a specific change of the powder mixture fraction during the layer deposition process. The layered FGM samples were tested by metallography, microhardness measurements and SEM analysis. The compositional variations could be either smooth or sharp. The SEM analysis showed that the minimal transition zone between two different alloys was only around 70μm. Fabrication of FGM structures by this process seemed feasible.

In order to achieve the rapid manufacturing of customized implants, Selective Laser Sintering (SLS) has been investigated for the production of bioactive implants and tissue scaffolds using composites of high-density polyethylene (HDPE) reinforced with hydroxyapatite (HA) [42]. Single-layer and multilayer block specimens made of HA-HDPE composites with 30 and 40 vol % HA were sintered successfully using the CO2 laser sintering system. The degree of particle fusion and porosity were highly influenced by the laser power and scanning speed, so material variations can be controlled by varying these laser processing parameters. Pores existed in the SLS-fabricated composite parts and an optimal fraction range of the pore sizes by controlling processing parameters could be found to facilitate tissue regeneration.

A Freeze-form Extrusion Fabrication (FEF) process capable of manufacturing FGM 3D parts and structures can be developed [43]. The study of this included the design and manufacture of a machine with a triple-extruder mechanism, and the electronics hardware and computer software to fabricate FGMs from multiple aqueous pastes. The pastes to be extruded should have an engineered composition and proper rheological behavior for extrusion through a fine hole to produce a 3D part. The paste recipes need to provide the paste with high solids loading, no phase separation under pressure, homogeneity of the paste throughout the extrusion process, and pseudoplastic behavior with a defined yield stress. To limit the difference in sintering shrinkage along the cross section of FGM components, $WC+ZrO_2$, W and ZrC were selected as the three pastes. A rheological behavior study with Al_2O_3/ZrO_2 paste was also performed to find an efficient binder for transforming the paste into a pseudoplastic with a high yield stress. The capability of the FEF system for fabricating 3D parts with desired material grading is validated by the color transitions and the corresponding extrusion velocity profiles in the fabricated limestone part and by measuring energy dispersive spectroscopy (EDS) peak intensities in the fabricated test bar with varying Al_2O_3/ZrO_2 ratios along the measurement direction.

2.3 Applications

The FGM concept can be applied to nearly all material fields. A variety of real and potential applications are described in the followings as examples. These include applications in transport systems, cutting tools and machine parts, and energy conversion systems. Other applications include semiconductors, optics, and biosystems [44]. In general, FGM applications include any engineering use that needs the gradual transition

of functions, or combinations of possibly incompatible properties such as refractoriness or hardness with toughness. With the rapid development of manufacturing techniques, it is reasonable to expect FGMs to have broader applications in the future.

2.3.1 Transport system and stealth

FGMs can be used as space vehicle components. For example, stealth missiles are now in great demand for militaries as modern weapons. One way to minimize wave reflection from a missile is to manufacture its parts from specific materials which can absorb electromagnetic energy emitted from an enemy's radar. Ceramic matrix composites reinforced with woven fabrics are the most promising option. The conducting properties of these ceramic composites are controlled by the properties of the fibers, the matrix, the interfaces, and the distribution of the various phases. Some specific distribution of the graded composites can prevent the electromagnetic wave reflection. Nicalon® SiC fibers, which are semiconducting, and Nextel® mullite fibers, which are completely dielectric, can be used in oxide matrix ceramic composites to get the desired effect. The Nasicon solid solution, with the structural formula $Na_{1+x}Zr_2Si_xP_{3-x}O_{12}$ ($0<x<3$), has an electrical conductivity that varies by four orders of magnitude by changing x. By varying electrical conductivity, Nasicon matrix composites reinforced with long semiconducting or dielectric fibers can have changing electrical properties designed to absorb electromagnetic wave energy at different microwave frequencies [45]. Material distribution optimization and delicate design can be accomplished for this material in ceramic matrix composites to absorb maximum electromagnetic energy at the frequencies of interest.

2.3.2 Cutting tools and machine parts

In modern factories, in order to improve machining efficiency, the cutting speeds and feed rates need to be substantially increased. As a result, modern cutting tools are required to withstand large thermomechanical stresses and withstand thermochemical reaction induced due to interaction with the parts being cut. Delicately tailored FGMs may reduce thermomechanical stresses significantly as shown in Figure 2.1. Various techniques to manufacture compositionally graded tools and methods for graded multilayer coatings have been developed to deal with the harsh working conditions at the cutting tool tip.

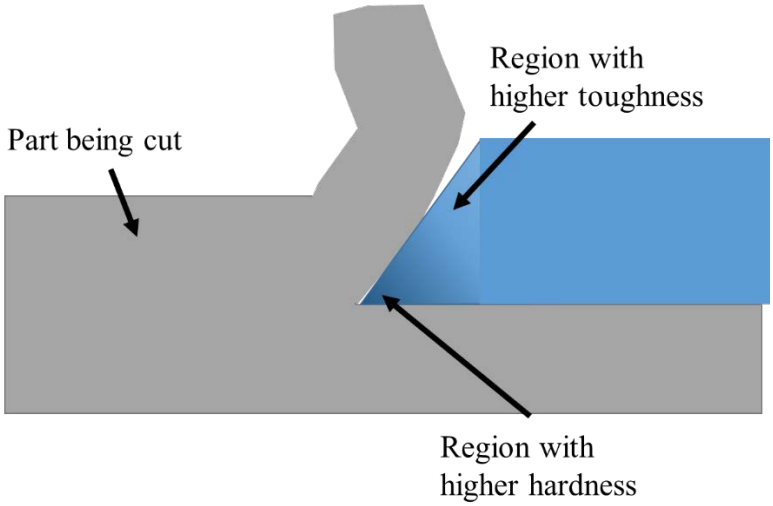

Figure 2.7 A cutting tool made of FGM

Cutting tools made of uniform materials generally cannot satisfy the needs of current working requirements. For example, cemented carbide (tungsten carbide-cobalt; WC-Co) tools often require extreme hardness at the cutting surface but higher toughness in the base material. If the size and configuration of the carbide particles remain the same,

the hardness of the WC-Co system has almost a linear relation with the binder (Co) content. On the other hand, at the same binder content, the hardness increases with decreasing grain size. Unfortunately, the transverse rupture strength and the fracture toughness (K_{IC}) decrease with increasing hardness almost independent of compositional and microstructural details. So an optimal cutting tool should have relatively smaller binder content and grain size on the tool cutting edge and have a gradual transition to more binder content and larger grain size in the core [46].

For machine parts, the major application of FGMs is for joints. These are mainly metal-ceramic joints for gas and steam turbines. The advantage of using an FGM joint is for thermal stress relaxation and improving the strength and toughness of the joints. For an alumina-nickel superalloy joint, the rupture strength of graded joints is 3-8 times higher than directly bonded joints, so FGM joints should have significantly longer life at high temperatures [47].

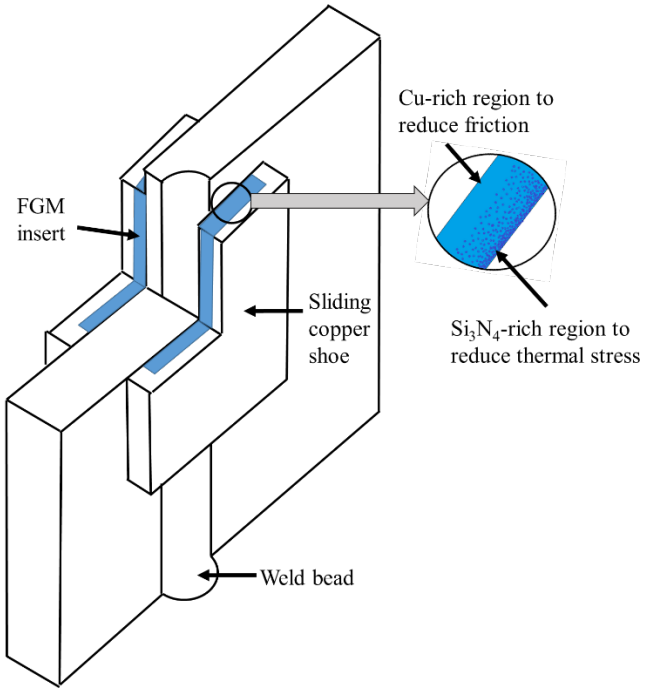

Figure 2.8 Automated electric arc welding of large aluminum sheets

Another FGM application is in the welding process to relax thermal stress and decrease the coefficient of friction. For instance, it can be used for automated electric arc welding of large aluminum sheets in building huge ships as displayed in Figure 2.8. This welding device uses sliding water-cooled copper shoes that move along the seam and support the molten aluminum bath. To prevent the shoes from sticking to the hot aluminum surface, the inserts are adapted, usually using silicon nitride to obtain a low friction coefficient and to induce a neat seam. However, their in-service life can be short under the thermal cycling conditions induced during the welding operation. This in-service life of the insert can be prolonged by using an Si_3N_4-Cu FGM, which is designed to retain the low coefficient of friction, improve the stability of the process and reduce the thermal stress [46].

2.3.3 Energy conversion system

Most current power stations are burning conventional fuels. By using advanced combustion techniques and combining stationary gas turbines with steam turbines, efficiencies of such systems have been raised to around 60%. Adoptions of FGMs can further improve the efficiency of these systems [46].

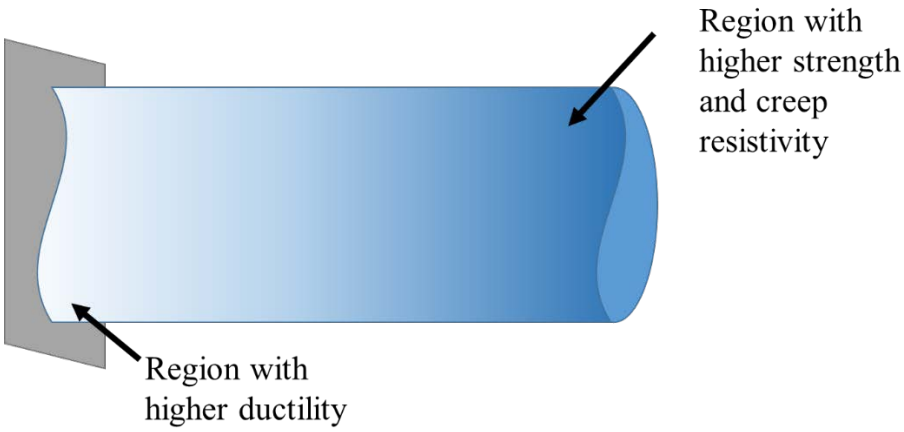

Figure 2.9 A gas turbine blade made of FGM

In gas turbine blades, the ductility in the root block needs to be maximized. The temperatures there is low compared to the blade, a result of the cooling. Creep performance is not important in the root area. In contrast, the airfoils need maximum strength and creep resistivity under high temperatures. At the blade area, ductility is of secondary concern. A gradient from a fully lamellar microstructure at the foil to a duplex microstructure at the root can provide the desired mechanical properties at both places. One method to obtain the desired gradient of properties is to create a gradient in the volume ratio of the $\alpha+\beta$ phases during isothermal annealing. This can be achieved by

utilizing a gradient of a ternary alloy with an addition of Cr thereby shifting the volume ratio [46].

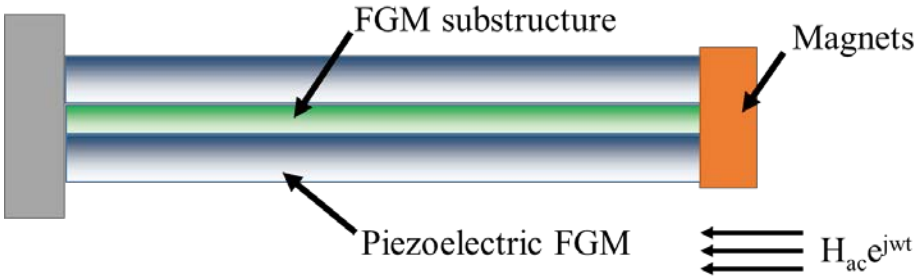

Figure 2.10 Magnetic energy harvesters using functionally graded composite cantilever

For improving harvesting ability, magnetic energy harvesters using FGM cantilevers, as shown in Fig. 2.10, were analyzed theoretically [48]. Output voltage of the harvester made of homogeneous materials was measured experimentally to verify the developed model and good agreement was observed. In the theoretical model, functionally graded properties with a power-law distribution along the thickness were assumed for piezoelectric and substructure layers. The electric current, voltage and power under closed-circuit condition with impedance were derived. The influence of the driven frequency, graded material distribution, substructure's thickness and impedance value on the output power was studied in detail. The numerical results showed that the introduction of functionally graded materials could enhance the magneto-mechano-electric coupling effect of harvesters. Different optimal impedance values could be obtained under different frequencies and material distributions, meaning the best harvesting ability was achieved.

Chapter 3 interpenetrating polymer networks (IPN)

3.1 Introduction

Among the materials suitable for making FGMs, interpenetrating polymer networks (IPNs) are one option that promises grading at the molecular level without the formation of undesirable interfaces. IPNs are a combination of two or more polymer networks that are intertwined, but not covalently bonded. As a result of growing the intertwined networks in the same physical space, IPNs cannot be separated unless the chemical bonds are broken. One can control an IPN's properties by controlling the ratios of the constructing networks. In contrast to growing interpenetrating networks, simple mixing of polymers in blends results in systems with regions occupied by each component and the development of interfaces that have low interfacial strength and are inclination to failure.

The first known published report on IPN was in 1914 by Jonas Aylsworth [49]. He added rubber and sulfur into the monomer mixture of phenol and formaldehyde, which on vulcanization formed a polymer network. Thus, the first recorded IPN was formed, even though the words polymer, network or IPN, had not yet been selected for their description. Many IPNs were fabricated later on [50-52]. The term interpenetrating polymer networks was first invented in 1960 by an early IPN researcher called John Millar [53]. His homo-IPN were processed from styrene suspension polymerization. He wanted to increase the particle sizes in order to make ion exchange resins. Millar was also the first to explain the molecular topology of an IPN clearly. The topic of IPN became popular later as a large number of related work and publications came into existence [54].

3.2 Types of IPN

IPNs can be classified into full-IPNs, semi-IPNs and thermoplastic IPNs based on chemical and physical bonding. Full-IPNs consist of two or more polymer networks that are at least partially intertwined on a molecular scale but not covalently bonded to each other and that cannot be separated unless chemical bonds are broken. In semi-IPNs, which are also called pseudo-IPNs, only one component of the mixture is crosslinked to form a network while the other stays in linear form. Thermoplastic IPNs are hybrids between polymer blends and IPNs that involve physical crosslinks, such an entanglements, rather than chemical crosslinks. These materials can flow at relatively high temperatures, similar to the thermoplastic elastomers, while at room temperature, they behave like IPNs.

IPNs can also be classified into sequential IPNs and simultaneous IPNs based on the preparing process. Sequential IPNs involves the initial formation of polymer network I followed by swelling of this network with monomer II along with a crosslinker and activator, which are then used to polymerized network II. In simultaneous interpenetrating networks (SINs), the monomers along with the crosslinkers and activators of both networks are mixed together. In this case, the reactions to form the networks start and progress simultaneously. For this to work, the reactions must be noninterfering.

3.3 IPN Applications

IPNs can be tuned to provide useful characteristics of their constituent components, or sometimes the mixture as a whole can display new properties that the single individual networks do not exhibit. A high degree of flexibility, controllable phase

domain sizes and a range of other properties in addition to thermoset properties endow IPNs with a multitude of applications in various fields [21]. Most of the applications are in the biomedical fields due to IPN properties.

3.3.1 Drug delivery

Key requirements in designing efficient drug delivery systems are the non-toxicity and the accurate control of kinetics of drug release rate. To accomplish the ideal features of an effective drug delivery system, polymeric drug carriers need some modification to their chemical structure [55, 56]. However, some chemically modified materials may have non-biocompatibility and toxicity issues. Some IPNs by certain processing methods are capable of controlling the delivery of drugs at a certain rate for a specific period, being biocompatible and avoiding the issues of toxicity. A similar choice is copolymerization, which forms a new chemical entity and may not conserve the properties of each polymer. IPN-based systems are more suitable for drug delivery because the interpenetration of crosslinked polymers leads to the materials that not only keep the features of both components but also combine them in a tunable way. Drugs can be delivered in a controlled way with minimum fluctuations by precisely designed IPN-based drug delivery systems. IPN-based systems also have several other physical and biological characteristics which make them suitable for drug delivery applications, such as enhanced solubility of hydrophobic drugs, excellent swelling capacity, stable drug formulations, biodegradability and specific tissue targeting. The release rate of a drug from an IPN hydrogel is controlled by degree of crosslinking, and solvent type, density, pore size of the matrix, nature and molecular weight of the drug. A typical hydrogel comprises of two components. One is a strong polymer network as a frame and the other

is permeation channels filled with water for diffusion of water-soluble solutes [57]. The water content of the matrix governs the release situation of the molecule within the hydrogel. High swelling capability of a hydrogel can facilitate release rate of a solute. Release of various drugs and proteins has been investigated in many IPNs. For example, semi-IPN hydrogels made of silk fibroin (SF) and polyacrylamide (PAAm) have been studied as a matrix for sustained drug release of two different molecules: trypan blue and FITC-inulin [58]. One way to increase the release rate of a drug is to reduce the number of hydrogen bonds between the IPN components. This can decrease the crosslinking density and thereby increase the free space within the polymeric matrix for drug to move more freely. Microgel/nanogel-hydrogel IPN composites using acrylamide and 2-hydroxyethylmethacrylate poly(acrylonitrile)-based core-shell nanoparticles have also been made and fluorescein sodium was chosen as a model drug [59]. The intent is to study the antimicrobial property of the particles against various kinds of bacteria. Modification of the polymer and modulation of the crosslinking modality are two factors to manipulate the physicochemical properties of the IPN matrix. They prove to be effective in designing a material system with tailored swelling, drug release, and degradation kinetics.

3.3.2 Tissue engineering

Tissue engineering is especially meaningful to human beings for its possibility to repair and regenerate diseased tissues. Development of tissue engineering scaffolds is necessary in biomedical research. Hydrogels have been regarded as promising candidates

for engineered tissue scaffolds due to its similarities to native extracellular matrix. In order to create engineered tissues with structure and function similar to native ones, the ability to control porosity in hydrogels is vital, but it's also quite challenging. Hydrogels with different mechanical properties can be obtained by the preparation of IPNs. For instance, Ferrer et al. [60] fabricated a sequential hydrophobic-hydrophilic IPN structure of porous-hybrid hydrogel of poly (ethyl methacrylate) and poly (2-hydroxyethyl acrylate). IPNs can also be employed as cartilage scaffolds and bone substitutes. Encapsulation of 3-D smooth muscle cells (SMCs) and 2-D culture of endothelial cells (ECs) have been prepared utilizing gelatin-bonded dextran-based hydrogel with relatively high modulus [61]. These hydrogels showed elastic properties that were superior to peptide/protein modified polyethylene glycol(PEG)-based hydrogels. With the help of such IPN hydrogels, adhesion of vascular endothelial cells in 2-D culture and proliferation of vascular smooth muscle cells in 3-D culture could sustain for 14 days. Compared to either original component, these IPN hydrogels are mechanically stronger and more stable against enzymatic digestion or UV degradation. IPNs comprising of 1-ethyl-3-(3-dimethylaminopropyl) carbodiimide and N-hydroxysuccinimide crosslinked porcine atelocollagen and poly(ethylene glycol) diacrylate crosslinked 2-methacryloyloxyethyl phosphorylcholine (MPC) have been made for corneal substitutes [62]. In spite of MPC's antiadhesive properties, these hydrogels could retain the full cell-friendly properties of collagen to promote corneal cell and nerve ingrowth. Besides, this hydrogel can interact with host tissues to advance tissue regeneration by mobilizing endogenous host stem and progenitor cells. Long-term properties of small-diameter vascular grafts made of a poly(ether)urethane-polydimethylsiloxane (PEtU-PDMS) semi-

IPN were investigated by Soldani et al. [62]. They compared the efficiency of the grafts with a standard expanded polytetrafluoroethylene (ePTFE) graft. The semi-IPN grafts experienced obvious remodeling and negligible calcification phenomena. Biologically derived IPNs from collagen and hyaluronic acid have been intensively studied for tissue engineering purposes [63]. Modulation of bone formation around the implant region have been reported using IPNs of poly (acrylamide-co-ethylene glycol/acrylic acid) with addition of Arg-Gly-Asp-arginylglycylaspartic acid (RGD) grafted to titanium implants [64]. Natural biomaterials based IPNs can provide a culture environment that can help tissue growth due to such IPNs' dynamic cell-responsive mechanical properties. Shikanov et al. [65] looked into the cell-responsive mechanical properties of fibrin-alginate in the in-vitro growth of ovarian follicles. IPNs derived from synthetic and a natural polymer could create a type of materials, which can gain the mechanical properties of the synthetic component, while keep the biological properties of the natural one unaltered. This offers material scientists a method to enhance some properties of the natural polymer.

3.3.3 Ophthalmic applications

For patients who are blind due to corneal disease, artificial corneas can serve as an effective cure. The requirements for an artificial cornea contain transparency, mechanical strength, oxygen permeability, permeability to glucose and cellular compatibility [66]. Glucose-permeable poly(dimethyl siloxane)-poly(N-isopropyl acrylamide) IPNs have been synthesized, characterized, and proved as ophthalmic biomaterial candidate by Liu et al. [67]. They prepared collagen-phosphorylcholine interpenetrating network hydrogels

as corneal substitutes in order to utilize its enzymatic resistance, hydrophilicity, and enhanced mechanical strength.

3.3.4 Dental applications

The reasons for using IPNs in dentistry are its toughness, mechanical interlocking to resin adhesives and favorable handling properties [68]. The extent of interlocking of resin adhesives to polymers and composites determines the clinical success of dental treatments using composite resin restoration. The debonding of restoration can be caused by inadequate interlocking of materials, resulting in the final failure of the treatment. IPNs are widely used not only as denture base polymers but also as artificial teeth. The properties of porcelain and polymers make them suitable to be artificial teeth material. Compared to tough polymers, porcelain is more prone to chipping. Polymers also have some shortcomings. For instance, crosslinked PMMA can be plasticized by food materials, which threaten its mechanical properties. IPNs of PMMA can avoid this setback as they don't swell as much as crosslinked polymers. Dentsply, a dental solutions company, has put artificial teeth to the market, under the trade names Trubyte and Bioform. These materials, based on PMMA-PMMA homo-IPNs, are swelling resistant and have excellent grinding ability [19]. IPNs also provide good interfacial adhesion due to swelling of the IPN nanostructure, which is a requirement for the success of modern adhesive dentistry.

3.3.5 Sound and vibration damping

IPNs with sound and vibration damping properties can be used in automotive, aircraft, construction, and appliance industries [69]. Controlling some factors such as

chemical structure of the polymer, glass transition temperatures, miscibility of the system, crosslinking density, and feeding sequences in polymerization can control the damping behavior of IPNs [21]. IPNs based on polyurethanes have been widely investigated to obtain insights into their damping property [26]. Such IPNs show high damping phenomenon over a broad range of frequencies and temperatures, controlled by the fraction of its component. In the paper these researchers also studied gradient semi-IPNs, which are characterized by the broad glass transition range because of superposition of a large number of relaxation maxima arising from the gradual variation in composition. This provides the possibility of creating novel noise and vibration dampening materials using gradient IPNs or semi-IPNs.

Chapter 4 Modelling of Functionally Graded Materials (FGMs)

4.1 Introduction

With the emergence of powerful computers and well-verified software, computational modeling has become a very informative and cost effective tool for materials engineers and part designers [70]. Modeling can not only avoid some costly experiments but also can provide information that experiments are not able to provide. The ability to accurately predict the temperature, stress, and strain fields is important since such parameters can strongly affect the performance of an FGM part and can play a key role in FGM component design [71].

The modeling of graded materials such as FGMs and layered composites has had a recent surge in interest due to developing applications such as is seen in emerging aerospace structures and in wind energy. As a result, the subject of modeling composite properties has been extensively studied, and a large number of related articles written on this subject. Several extensive review articles are available that provide both good overviews of the subject and deep insight into the significant complexities [72].

FGM distribution is usually controlled by some material parameters, such as componential fraction, void density or fiber orientations. So this chapter consists of two parts: parameterizing the state of the material and the methods for modelling the grading of FGMs. The former discusses the methods to determine the mechanical behavior of materials used to construct an FGM based on the material parameters used to characterize

them. The latter focuses on the methods to model the grading of the mechanical response of an FGM part.

4.2 Parameterizing the state of the material

There are many ways to parameterize the state of the material which forms an FGM part. They can be categorized into two groups: homogenization methods and phenomenal methods. Typical modeling approaches are then described in detail in the followings.

4.2.1 Homogenization methods

Efforts to determine analytically the effective thermophysical properties of composites, of which FGMs are one special kind due to their gradual property variation, started decades ago [73]. To estimate thermophysical properties of FGMs, a basic assumption is that the microscopic length scale for the FGM is much larger than molecular dimensions, but obviously smaller than the macroscopic sample length. An FGM can then be regarded as a continuum on the microscopic scale, and the effective properties on the macroscopic scale can be derived from the distribution assumed in the microscopic scale. This concept is named homogenization. FGMs constructed by the formation of mixture of two or more phases have been studied extensively. Thermophysical properties of an FGM depend on its individual phase properties, volume fraction, size, shape, orientation, and spatial distribution of the phases. Property estimates are difficult because the fabrication processes and the application conditions for FGMs often involve significant temperature variations. So to obtain the information for accurately modelling the FGM properties, vast number of experiments and measurements are required, which is highly costly and not practical. In most cases only the information

for the individual phases is available. To provide reasonable estimates of material properties based on limited experimental data is a challenging but important task of the modeling process. Three widely-used homogenization approaches for microscopic FGM modeling are presented in the following sections.

4.2.1.1 Rules of mixtures

A common approach for estimating the material properties of FGMs is to apply a rule of mixtures. These relationships can be used to approximate thermal or mechanical properties of a composite material in terms of the individual properties and relative amounts of the constituents, although the rules are actually not physical or mathematical. The simplest one is the classical linear rule of mixtures, or Voight estimate, for two constituent materials [74]:

$$P = V_\alpha P_\alpha + V_\beta P_\beta \tag{4.1}$$

where P is a typical property of interest, V is the volume fraction, and the subscripts α and β are used to distinguish the two constituents. The Voight estimate is simply a volume based arithmetic mean. This method is quite easy to use but the model adopting this method seldom concurs with experimental data due to its over-simplification. To overcome this disadvantage, the rules of mixtures can also be described in a modified form to include interaction effects between constituent materials, either by utilizing in-situ constituent properties [75] or by including empirical data. Complex stress-strain data have been approximated using this empirical approach.

4.2.1.2 Self-consistent method

The self-consistent method is based on the solution to an auxiliary inclusion system where a single ellipsoidal inclusion is embedded in an infinite medium. In this system it is assumed that the inclusion and the infinite medium are perfectly bonded. Therefore, displacement and traction are continuous across the interface of the two phases. One can determine the stresses and strains by applying uniform stresses or strains to the system at infinity. It was first shown by Eshelby [76] that in such types of problems, the stress and strain fields in the inclusion are uniform. Further, the elastic properties can be determined by finding the relation between far-field stresses and strains in the homogeneous medium and stresses and strains in the inclusion, or the stress or strain concentration factors. The problem of determining the effective properties of such a system was further investigated by Hill [77] and Budiansky [78]. In this approach the average stress and strain fields in the fiber are taken to be equal to those in the inclusion problem. Further, the infinite medium is taken to be homogeneous with the same properties of the composite.

4.2.1.3 Mori-Tanaka Method

The original method was proposed by Mori and Tanaka [79] in 1973. Further, Benveniste [80] proposed a simpler version of the same model. The key assumption in this model is, the average strain in the inclusion is related to the average strain in the matrix by a fourth order tensor. Further, this material is subjected to uniform strain at infinity.

A comparison between the Mori-Tanaka and self-consistent models of FGM was studied by Reiter.T et al. [81]. The Mori-Tanaka model was shown to present accurate

prediction of the properties with a well-defined continuous matrix and discontinuous inclusions, while the self-consistent model was better in skeletal microstructures characterized by a wide transition zone between the regions with predominance of one constituent phase. Based on the analysis, the authors concluded that the methods developed for homogeneous particulate materials could provide satisfactory results in FGM subjected to uniform and nonuniform loads.

4.2.2 Phenomenological methods

Phenomenal methods don't consider the mechanism at the microscopic level. Instead, they regard the mixture or composites as a whole. Experiments are carried out to obtain the effective material properties at the macroscopic level with respect to several different material parameters. The relation of the material parameters, which are not included in the experiments, can be acquired from curve fittings of the experimental results.

Homogenization methods usually have some assumptions at the microscopic level, which limit the scope of application of these methods. Phenomenal methods assume that properties of the material are continuous functions of the material parameters, which is often true if the number of experiments are sufficient. Phenomenological methods require more experiments, compared to homogenization methods, which can be costly.

4.3 Methods to model the grading of FGM

Once we have the material properties of the composite system in terms of the material parameters, the next step is to model the mechanical response of an FGM part. For an FGM part with simple geometries and simple variation of simple material

properties, such as elastic behavior, some analytical solutions are available. The basic partial differential balance equations from continuum mechanics are applicable to any continuum including an FGM part. For relatively complex geometries or constitutive behavior, numerical solution techniques, for example the finite element method, can be used to provide satisfactory approximate solutions. To use these numerical methods, one needs find ways to include the grading into the solution. Methods to model the grading of FGM can be categorized into two types: function based models and discrete models, which are discussed in the followings.

FGM distributions can be represented by a functional model, with the design variables chosen as the coefficients of analytical functions, for instance the power index for power-law formulae or polynomial coefficients for Taylor expansions. This model is concise and computationally efficient, as only a few design variables can fully characterize the material distributions. One apparent disadvantage of functional models is that it is nearly impossible to model complex material grading with a simple analytic function throughout the entire geometric domain [82]. Another disadvantage emerges when one plans to design an FGM part for a certain purpose using the optimization methods. The designer needs to preselect a function to describe the FGM distribution, which may exclude the optimal solution. As a result, the material variation pattern becomes a subjective personal choice, where the designer's experience plays a big role.

Functional models of FGMs have been studied intensively. As discussed in Chapter 2, currently most FGMs are used in plate or shell like structures. The variation is only along the thickness direction, which makes functional models applicable and easy to utilize. For example, J. N. Reddy [83] developed a plate element based on third-order

shear deformation plate theory in which variation of properties through the thickness described by power law function was introduced and theoretically integrated for the thickness dimension. In this case, he provided numerical results of the linear third-order theory and non-linear first-order theory to illustrate the deflection and stress changes resulting from material grading. Jinseok Kim et al. [84] modified the third-order shear deformation plate theory to bring out the effects of couple stress, geometric nonlinearity and power-law variation of the material composition through the plate thickness on the bending deflections of plates. The principle of virtual displacements was utilized to develop a nonlinear finite element model. Numerical results were presented for static bending problems of rectangular plates with various boundary conditions. T. Kant et al. [85] employed a higher-order shear and normal deformations plate theory for stress analysis and free vibration of functionally graded elastic, rectangular, and simply supported plates. The effect of variation of material properties in terms of material grading index in exponential and power law functions on the deformations, stresses, and natural frequency of FG plates was studied. N. A. Apetre et al. [86] investigated a sandwich panel with an FGM layer that was impacted by a low-speed rigid cylindrical projectile. The middle layer of the sandwich panel was taken to have a variation of Young's modulus described by a polynomial function in the thickness coordinate. The two-dimensional elasticity equations for this structure were solved by a combination of Fourier series and Galerkin method. The results indicated that the impact damage in sandwich composites could be considerably mitigated by the functionally graded middle layer. The nonlinear dynamic response of functionally graded rectangular plates under combined transverse and in-plane excitations was investigated under different internal

resonance conditions by Y. X. Hao et al. [87]. The plate has a gradual volume fraction variation in power law function. The governing equations of motion of the FGM plates were derived by Reddy's third-order plate theory and Hamilton's principle and, solved numerically by a 4th-order Runge-Kutta algorithm.

Discrete models offer a more flexible, objective representation of material heterogeneity compared to functional models. The shortcoming associated with a discrete model lies in the large number of design variables. This can raise the computational cost to an unaffordable level when it comes to a design problem using optimization methods. The most commonly used discrete models are based on finite element methods.

There are several strategies to introduce the variation of properties into FEM analysis for discrete models, which can be basically classified into four methods. The first method uses uniform elements, but assigns different properties to each element. For example, Anlas et al. [88] introduced grading by assigning the value of the property at the center of the element to the whole element. They noted that the global strain energy calculated by this method is accurate, but not the local stresses and displacements. The second method is to assign the material properties to the global nodes, such as was done by Jeong-Ho Kim et al. [89], and to use the element interpolation to distribute the values to all the elements that are attached to the node. This method results in a continuous distribution of properties in the body. The third method is to assign properties to the local nodes of each element and to use the element interpolation to calculate properties inside each element. This method results in continuous variations of properties in each element, but allows discontinuity in properties across element boundaries. The fourth method uses a function to describe the properties over the element. In this method the property, when

needed, is evaluated by calling on the function. Santare et al. [90] modeled a graded plate by this method. In particular, the values of the property at the integration points (Gauss points) were evaluated using the function. They used different boundary conditions perpendicular and parallel to the gradient direction, showing that the graded finite element results were closer to the analytic solution than for the solution with constant-property elements when the boundary conditions were applied perpendicular to the gradient direction, but worse when parallel. To illustrate the difference between these 4 methods consider the example shown in Figure 4.1 using two elements. As can be seen, for the example selected, only the fourth method (using a function) reproduces the proposed property variation exactly. The first method (assigning different properties to standard constant-property elements) does a poor job of reproducing both the jump and the variations. The second method (assigning values to global nodes) is incapable of capturing the jump in properties between the elements, while the third method (assigning properties to local element nodes) captures the jump between the elements accurately. Methods one to three use lower order approximations so they do not accurately capture the quadratic variation in the second element.

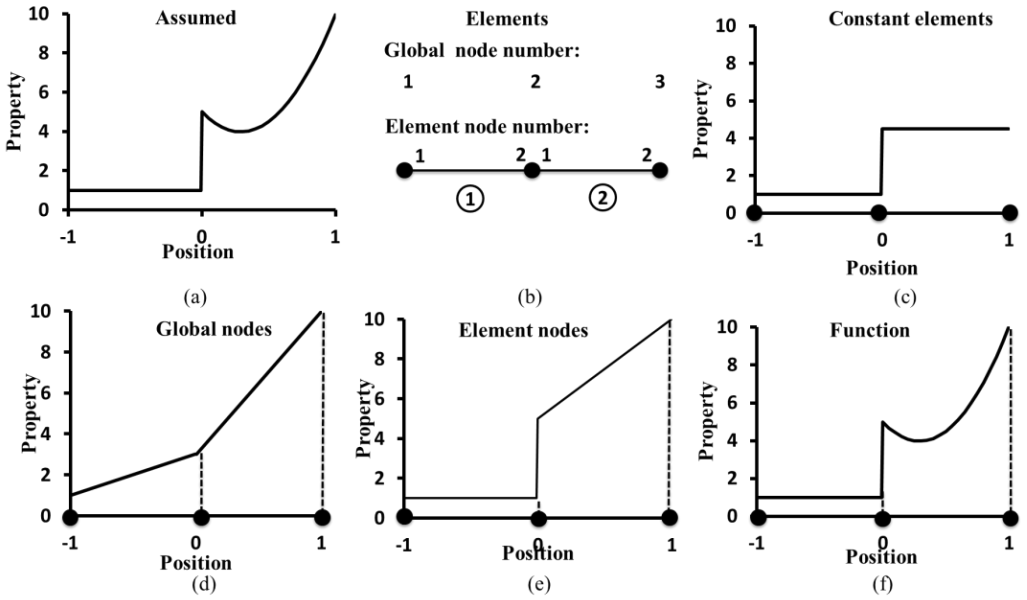

Figure 4.1 Example material distribution and FEM models: (a) assumed for of actual material distribution, (b) finite element model using two two-node elements, (c) material modeled using two elements with constant properties matched to mid-point, (d) material modeled by giving properties to global nodes, (e) material modeled by giving properties to element nodes, (f) material modeled by defining a function for the property variation. [91]

The focus of this dissertation is to study the mechanical response of a part made of FG-IPN. Modelling FGM microscopically from its compositional properties is not appropriate since components of IPN are intertwined at the molecular network level. So we use the phenomenal method for describing the properties in terms of IPN network fraction. The elastic properties and failure criteria are curve-fitted from the experimental results as functions of material parameters. For FG-IPNs, compositional ratios are chosen as material parameters. To model the grading of an FGM part, discrete modelling based on the finite element method is chosen as the tool to avoid the limitations caused by functional models discussed previously.

Chapter 5 Development of conditions for robust higher order materially graded elements

5.1 Introduction

There is an interest to model and simulate the response of systems that have varying material properties in space [71]. A number of strategies have been proposed to capture this variation of properties. One such strategy is to use standard finite element method FEM interpolation for modeling the continuous variation of properties in a part [92]. While this strategy allows exact introduction of continuous variations of properties into the FEM analysis, it comes with the possibility of introducing a potentially detrimental problem. The possible problem arises from interpolations that result in regions in an element with a change of sign of the moduli even when the nodal values of the moduli are all of the same sign. This can happen when using higher order (p-type) interpolations for better characterizing grading of properties in an element. This chapter will focus on identifying the conditions under which this problem can occur and proposes a way to protect against this event in quadratic elements.

Within the modeling methods that give properties to global or local nodes, there are at least two subdivisions. One may be termed fully-isoparametric and the other might be termed semi-isoparimetric. The fully-isoparamteric method was first proposed by Jeong-Ho Kim et al. [89]. In this method the same interpolations are used to approximate

all variables including the distribution of material properties. They tested idea using Q4 and Q8 elements and evaluated their results by comparison to analytical solutions. They conclude that the results are very reliable except when load is applied parallel to the direction of material variation. The semi-isoparametric method simply chooses a different interpolation scheme for material variation, as opposed to the interpolation used for all other variables.

Fully-isoparametric graded finite elements were used by D.V. Kubair et al. [93] to study the stress concentration factor due to a circular hole in an FGM panel under uniaxial tension. They termed this method as the multiple isoparametric finite element method. They tried to optimize the property distribution to reduce the stress concentration at the hole. For this they employed exponential and power-law variation of material properties along different directions and used various material inhomogeneity parameters. They showed that they could reduce the expected stress concentration of 3 around the hole for a homogenous body down to 2.31 by using inhomogeneous material property distribution. Fully-isoparametric graded finite elements were also employed by K. Asemi et al. [94] in three-dimensional static and dynamic analysis of functionally graded elliptical plates. The three-dimensional graded finite element formulation was derived based on the principle of minimum potential energy and Rayleigh Ritz method.

Even though higher order interpolation has been used to successfully model grading in an element and simulate the response of inhomogeneous bodies, care needs to be taken to avoid interpolated regions with unrealistic values for the properties. In particular, the possibility of a material parameter, such as the elastic modulus, changing its sign inside the element produces regions of non-physical behavior, and can have potentially

detrimental effects on the solution. This can happen even when one has only positive nodal values for the parameters. The problem of finding these non-physical regions for polynomial interpolations is analytically possible for polynomial interpolations of order up to four. To identify the range of nodal parameters that can introduce regions of sign reversal in the material parameters, we study the problem of interpolating the elastic moduli using a 3-node Lagrange interpolation. We combine this material interpolation with otherwise standard p-type isoparamtric elements to show the potential effect and the estimated rules to avoid it.

5.2 Interpolation in FEM

In the following we consider one- and two-dimensional linearly elastic problems modeled, respectively, by line and quadrilateral elements using standard Lagrange interpolations. For these we assume position $\mathbf{X}$ and displacement $\mathbf{u}$ are given, respectively, by the isoparametric interpolations of space and displacement by

$$\begin{aligned} \mathbf{X} &= \sum_{p=1}^{nnpe} \mathbf{X}^p N_p(\xi), \\ \mathbf{u} &= \sum_{p=1}^{nnpe} \mathbf{u}^p N_p(\xi), \end{aligned} \tag{5.1}$$

where $\mathbf{X}^p$ and $\mathbf{u}^p$ are, respectively, the location and displacement of node p for an element with shape functions $N_p(\xi)$ given in terms of the parametric coordinates ξ for $nnpe$ nodes per element. The material grading in the element is assumed to follow similar Lagrange interpolations, but of possibly different order. For example, the shear modulus G in the element is assumed to be given by the interpolation

$$G = \sum_{p=1}^{mnpe} G^p N_p^*(\boldsymbol{\xi}), \qquad (5.2)$$

where G^p is the shear modulus at node p for an element with $mnpe$ (material nodes per element) with the associated shape functions $N_p^*(\boldsymbol{\xi})$. We term the element fully-isoparametric if the same shape functions are used for the material as that for space and displacement (i.e., $mnpe = nnpe$) and semi-isoparametric if they differ.

5.3 The FEM problem

For the demonstrations we consider the simplified equilibrium equation $div(\boldsymbol{\sigma}) = 0$ in a body with stress $\boldsymbol{\sigma}$ and without body forces. It is assumed that the body is subject to displacement and traction boundary conditions as displayed in Fig 5.1. The notation $\alpha(\mathbf{X})$ means the material distribution is a function of location. The traction on the surface with normal $\hat{\mathbf{n}}$ is calculated from the Cauchy relation $\mathbf{t}^{(n)} = \hat{\mathbf{n}}\boldsymbol{\sigma}$. The stress in the body is assumed to follow the linear elastic Hook's law $\boldsymbol{\sigma} = \mathbf{E} : \boldsymbol{\varepsilon}$, where $\boldsymbol{\varepsilon}$ is the infinitesimal strain and $\mathbf{E}$ is the fourth order elasticity tensor that for the demonstrations is taken as that of isotropic elasticity. This problem is formulated in a standard Galerkin FE formulation. For the one dimensional case, we simplify this to that for a bar under extension.

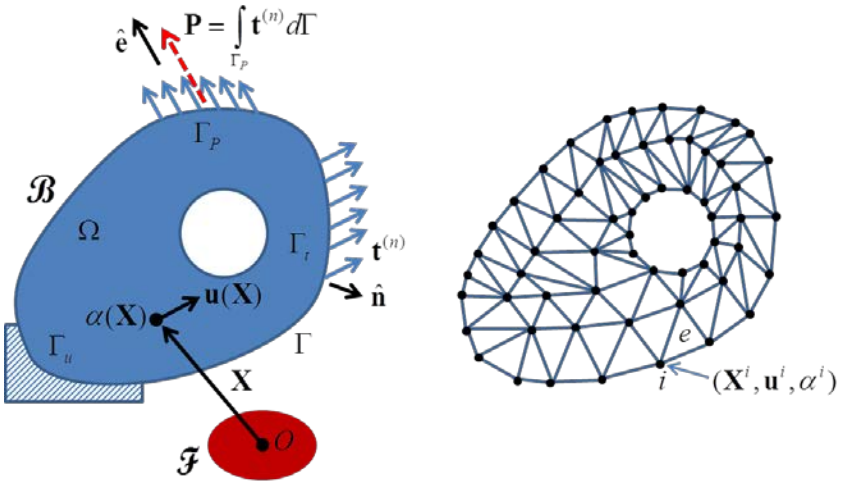

Figure 5.1 Mechanically loaded system under displacement or traction boundary conditions (left), and a schematic FEM mesh (right).

5.4 Grading properties using three-node quadratic elements

When using shape functions to interpolate the properties in a graded material, we select the value of the properties at the nodes and use an interpolation as given in Eq. 5.2 to evaluate the distribution of properties at all point of the element. This is then used to obtain the needed material properties at the integration points and at other point where the stress or traction is to be calculated.

In most cases material properties are physically restricted to being positive numbers and so the selected nodal values of the property are assumed as positive numbers. Even though the nodal values of the properties are selected positive, the interpolation might result in regions of negative properties, which, as will be shown, result in singular solutions that can overshadow the expected results. This sign change of the property in an element can occur in higher-order one-dimensional line elements. It is clear that one-node (constant) and two-node (linear) interpolations produce only positive interpolations when positive nodal values are selected. Yet, from three-node (quadratic)

interpolations one has the possibility of getting regions with negative properties, even when all the nodal values are positive. Fig. 5.2(b) demonstrates this possibility for a three-node line element with nodal moduli given as $(G_1, G_2, G_3) = (20, 1, 1)$ when using the standard Lagrange shape functions shown in Fig. 5.2 (c-e).

The possibility of getting a sign reversal in a continuous function, as is the case for the Lagrange interpolations, introduces points of zero value for the properties. These zero property points typically result in singularities in the response. If these regions of negative properties are unintended, for example resulting from assignments of nodal elastic moduli by an optimization program in designing a functionally graded part, the solution will be dominated by the unintended singularities. One, thus, needs to find a way to avoid assignment of moduli at the nodes that will produce such sign reversals. This can easily be done for three-node quadratic elements as follows.

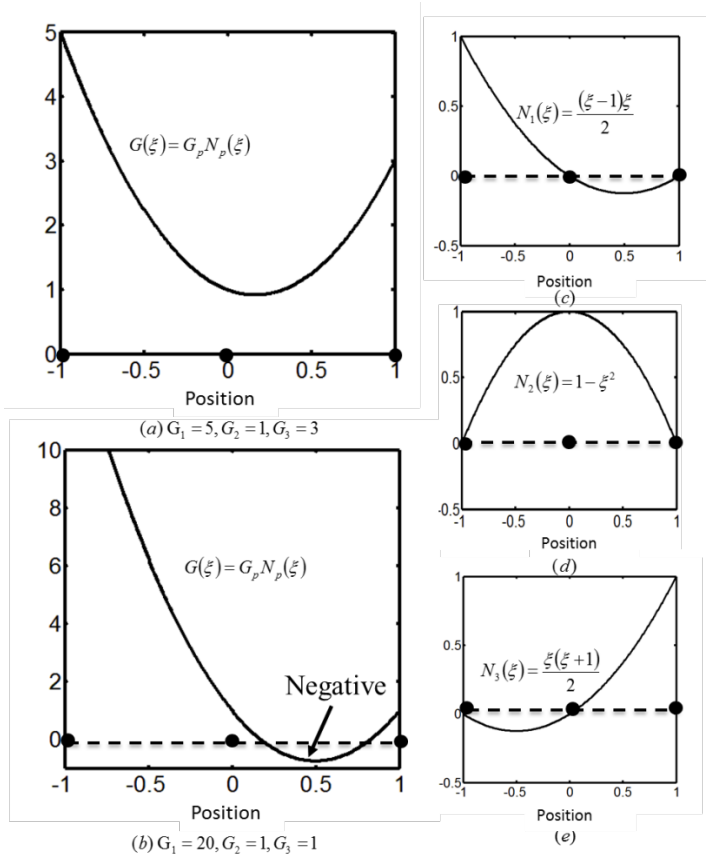

Figure 5.2 Examples of modulus distribution and shape functions for a three node parametric element over the interval (-1, 1): (a) Interpolation of the modulus for the nodal shear moduli (G_1,G_2,G_3) = (5,1,3), (b) Interpolation of modulus for nodal shear moduli (G_1,G_2,G_3) = (20,1,1), (c) first shape function, (d) second shape function, (e) third shape function. [91]

For a 3-node element, the problem of identifying positive nodal moduli that result in regions of negative modulus is tractable. Let us set up this problem. For the 3-node parametric element with the Lagrange shape functions given in Figure 5.2(c-e), defined on the isoparametric domain (-1,1), one can write Eq. 5.2 for the interpolation of the shear modulus as

$$G(\xi) = \frac{1}{2}\xi(\xi-1)G_1 - (\xi-1)(\xi+1)G_2 + \frac{1}{2}\xi(\xi+1)G_3$$
$$= \left(\frac{G_1}{2} - G_2 + \frac{G_3}{2}\right)\xi^2 + \frac{G_3 - G_1}{2}\xi + G_2. \tag{5.3}$$

This interpolation has the generic quadratic form of $G(\xi) = a\xi^2 + b\xi + c$ for the coefficients

$$\begin{aligned} a &= \frac{G_1}{2} - G_2 + \frac{G_3}{2}, \\ b &= \frac{G_3 - G_1}{2}, \\ c &= G_2. \end{aligned} \tag{5.4}$$

Since the interpolation is continuous, the boundaries of the negative modulus regions are defined by the points of zero modulus $G(\xi) = 0$ in the domain (-1, 1), and can be evaluated from the solution of the quadratic equation given by

$$\xi = \frac{-b \pm \sqrt{b^2 - 4ac}}{2a}. \tag{5.5}$$

Taking into consideration that G_1, G_2 and G_3 are all positive, one can show that a negative modulus region inside the element will exist only if the following three restrictions are simultaneously satisfied:

$$\begin{aligned} &G_1 - 4G_2 + 3G_3 > 0, \\ &3G_1 - 4G_2 + G_3 > 0, \\ &\frac{(G_3 - G_1)^2}{4} - 2(G_1 + G_3 - 2G_2)G_2 > 0. \end{aligned} \tag{5.6}$$

Since the interpolation given in Eq. 5.3 is linear in the nodal moduli, multiplying the nodal moduli by the same positive constant will not change the sign and thus will not change the region with the same sign. This allows us to normalize the three moduli by the value of any one, thus reducing the parameter space to two. Fig. 5.3 shows the nodal moduli space using the modulus at the second (center) node as the normalizing modulus. The figure separates out the space of positive nodal moduli into those that produce regions of negative modulus in the element (shown in white) and those positive nodal moduli that produce no negative regions (shown in color).

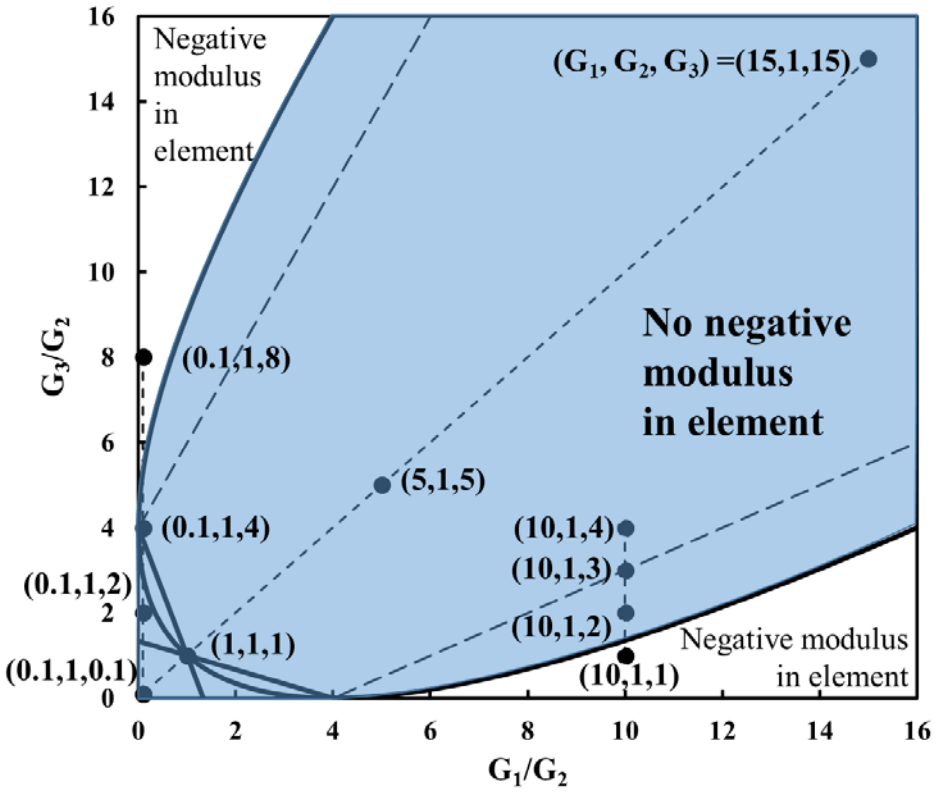

Figure 5.3 Mapping of the space of positive nodal moduli that can produce regions of negative modulus for a 3-node element. The part shown in white designates the existence of a negative modulus region in the element. For the balance, the modulus is always positive. [91]

An analysis of Fig. 5.3 indicates that the region close to the origin and described by $0 < G_1 < 4G_2$ and $0 < G_3 < 4G_2$ defines one range of nodal moduli that produces no negative regions in the element. That is, as long as the modulus values for the side nodes are less than 4 times the modulus at the center node, there will be no negative modulus region in the element. This can be taken as a simple rule of thumb to avoid regions of negative modulus in the element even though, as can be seen, a much large range of moduli are, in general, available to consider. The full region of acceptable values for the nodal moduli are defined by the quadratic curve given in the third condition in Eq. 5.6. The full region of admissible nodal moduli is defined by

$$\begin{aligned}
&\text{if } 0 < \frac{G_1}{G_2} < 4 \quad \Rightarrow \\
&\quad 0 < \frac{G_3}{G_2} < \frac{G_1}{G_2} + 4 + \sqrt{\left(\frac{G_1}{G_2} + 4\right)^2 - \left(\frac{G_1}{G_2} - 4\right)^2} \\
&\text{if } 4 < \frac{G_1}{G_2} \quad \Rightarrow \\
&\quad \frac{G_1}{G_2} + 4 - \sqrt{\left(\frac{G_1}{G_2} + 4\right)^2 - \left(\frac{G_1}{G_2} - 4\right)^2} < \frac{G_3}{G_2} < \frac{G_1}{G_2} + 4 + \sqrt{\left(\frac{G_1}{G_2} + 4\right)^2 - \left(\frac{G_1}{G_2} - 4\right)^2}
\end{aligned} \tag{5.7}$$

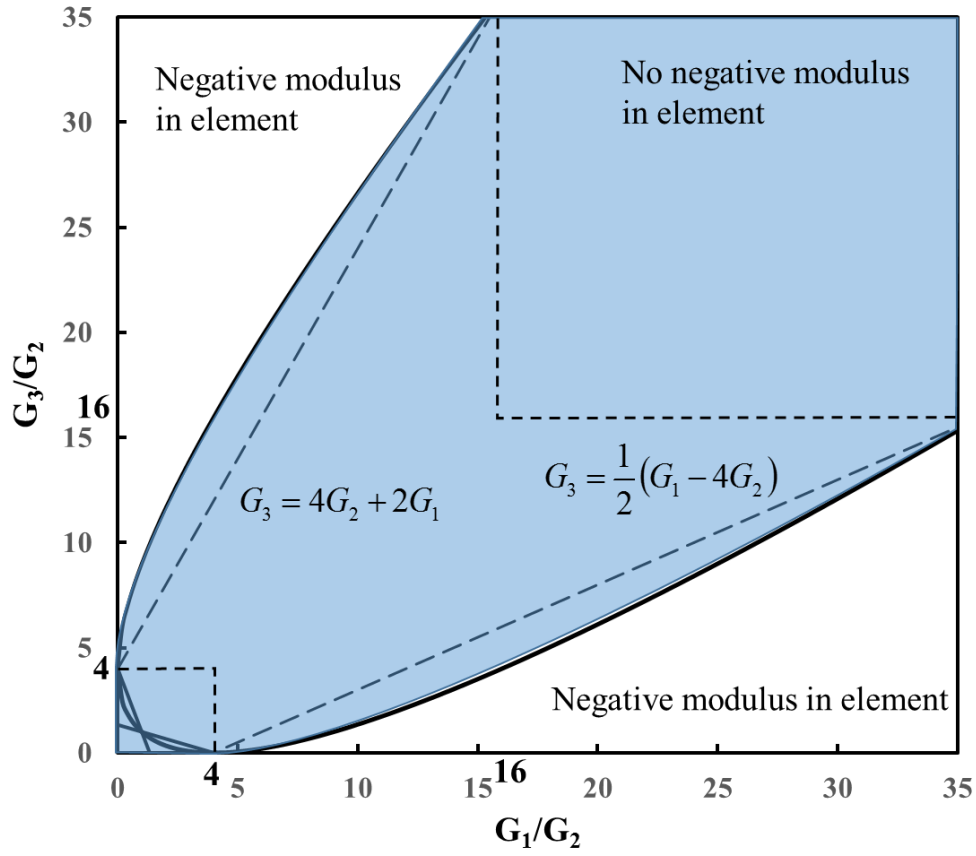

Figure 5.4 Estimation of the admissible region of nodal moduli that give only positive values in the element. [91]

Once the ratio of either of the side moduli are larger than four times the center modulus, the bounds on the other end's modulus is quadratic. One may approximate the quadratic bounds in a limited domain by linear conditions. For example, Fig. 5.4 shows the linear bounds for the case when one of the two end moduli are less than 16 times the center modulus. The constraint is symmetric and can be written, for example, based on the left end modulus as

$$
\begin{aligned}
&\text{if } 0 < \frac{G_1}{G_2} < 4 \quad \Rightarrow \\
&\quad 0 < \frac{G_3}{G_2} < 4 + 2\frac{G_1}{G_2} \\
&\text{if } 4 < \frac{G_1}{G_2} < 16 \quad \Rightarrow \\
&\quad \frac{1}{2}\left(\frac{G_1}{G_2} - 4\right) < \frac{G_3}{G_2} < 2\frac{G_1}{G_2} + 4
\end{aligned}
\tag{5.8}
$$

As an example to show the potential problem that can result from regions of negative modulus in the element, let us select the point with nodal elastic Young's moduli $(E_1, E_2, E_3) = (10,1,1)$ that is located in the white region of Fig. 5.3 indicating the existence of a negative modulus range. To capture the contrast in results, we also select three adjacent points $(10,1,2)$, $(10,1,3)$ and $(10,1,4)$ that are in the adjacent blue region of Fig. 5.3 indicating that we should get no negative modulus regions in the element. This example could correspond to a problem that has a varying hard region adjacent to a soft region as depicted in Fig. 5.5 for the uniaxial extension of an inhomogeneous bar. If we model this bar with one 3-node fully isoparametric element and solve for the axial stress using FEM analysis, one would get the stress distributions given in Fig. 5.6. The error estimate noted in this figure for each case is calculated using

$$
Err_\sigma = \frac{1}{L}\int_o^L \left(\frac{\sigma - \sigma_o}{\sigma_o}\right)^2 dx, \tag{5.9}
$$

where σ is the calculated stress, $\sigma_o = 1$ is the exact solution for the selected bar of length $L = 2$.

As noted in the Fig. 5.6, the exact analytical solution for this problem is a constant stress equal to the applied stress of 1, while the FEM solution for $(E_1, E_2, E_3) = (10,1,1)$ resulted in oscillations in the solution between -3 and 3, showing a -400% to +200% error in solution value. This unrealistic result indicates the potential problem with using interpolations that result in elements with negative modulus regions. In contrast, the other three solutions in Fig. 5.6 that are for nodal moduli that do not create negative modulus regions show much smaller error. As can be seen in Fig. 5.6, the error estimate drops from 1.68 for the element slightly outside the admissible nodal modulus region shown in Fig. 5.3, to 0.3-0.37 for adjacent points with nodal moduli in the admissible region. Similarly, Fig. 5.7 shows nodal elastic moduli that graze the vertical axis (shown in Fig 5.3). As can be seen, the error ranges from 0.12-0.16 when inside the range of admissible nodal moduli, but jumps to 29.8 outside this range. In contrast, Fig. 5.8 shows that moving along the diagonal in Fig. 5.3 from $(E_1, E_2, E_3) = (0.1,1,0.1)$ to $(15,1,15)$ produces an error only up to a value of 0.54.

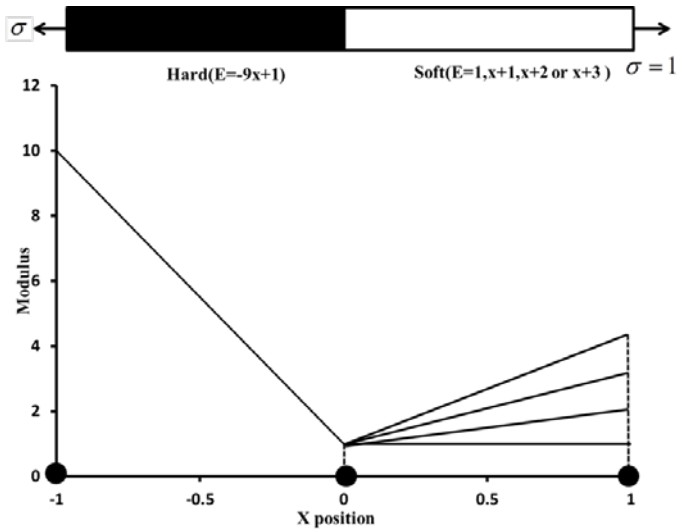

Figure 5.5 Demonstration of modulus distributions that will correspond to the point (E1,E2,E3) = (10,1,1), (10,1,2), (10,1,3) and (10,1,4) shown in Fig. 5.3 when modeling with a single quadratic (3-node) element. The case of (E1, E2, E3) = (10, 1, 1) will create a region of negative modulus. [91]

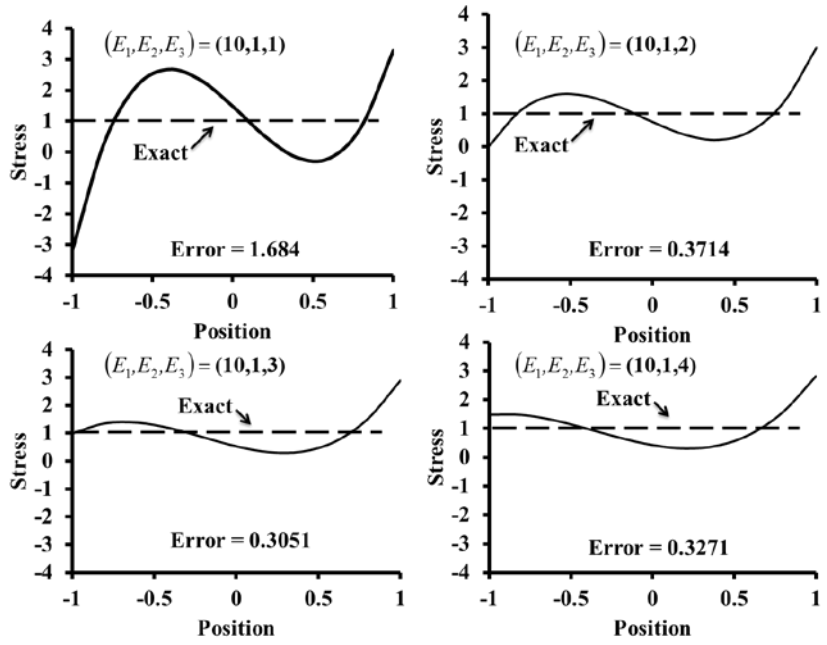

Figure 5.6 Stress distribution obtained by FEM using a single 3-node fully-isoparametric graded modulus element for (E1,E2,E3) = (10,1,1), (10,1,2), (10,1,3) and (10,1,4) for modeling the problem described by Fig. 5.5 with exact solution of 1. [91]

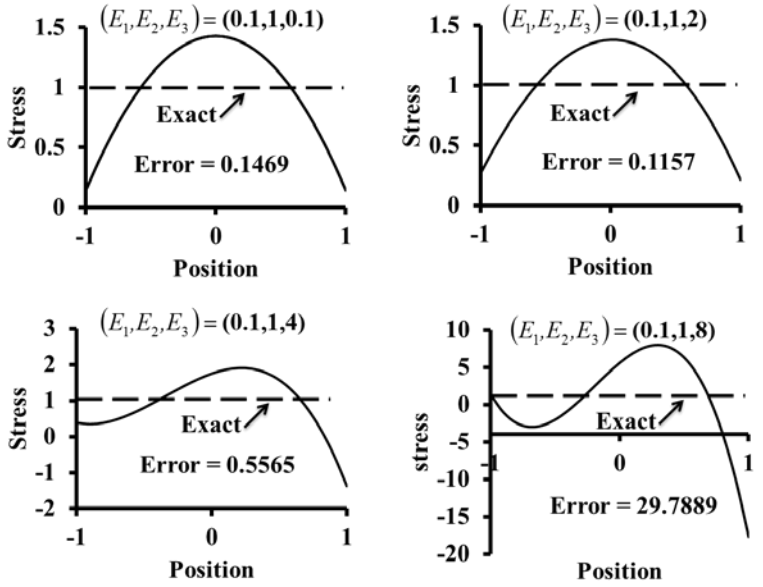

Figure 5.7 Stress distribution obtained by FEM using a single 3-node fully-isoparametric graded modulus element for (E1,E2,E3) = (0.1,1,0.1), (0.1,1,2), (0.1,1,4) and (0.1,1,8) for modeling uniaxial extension with an exact solution of 1. [91]

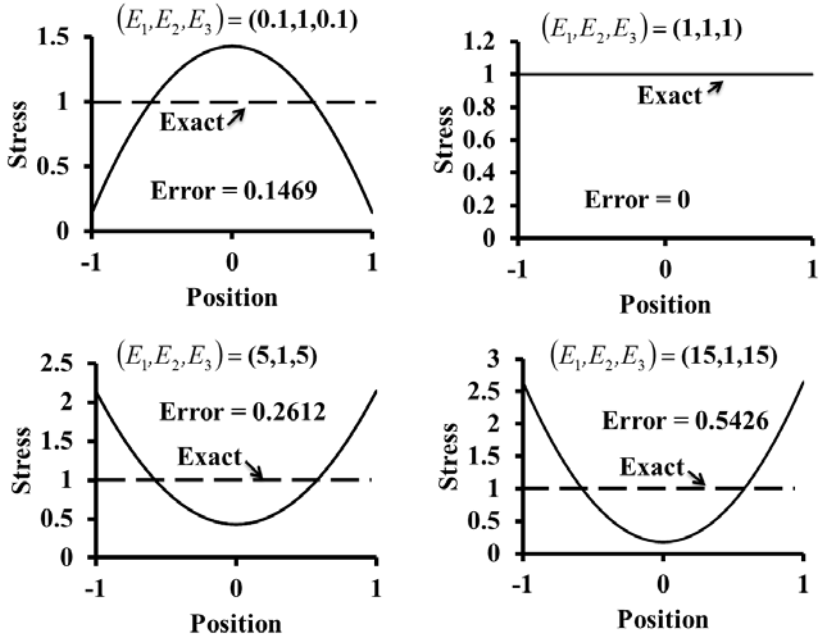

Figure 5.8 Stress distribution obtained by FEM using a single 3-node fully-isoparametric graded modulus element for (E1,E2,E3) = (0.1,1,0.1), (1,1,1), (5,1,5) and (15,1,15) for modeling uniaxial extension with an exact solution of 1. [91]

The error in strain can be substantial for elements with regions of both positive and negative moduli. Consider again a problem similar to that described in Fig. 5.4, but with a constant hard region of modulus 10 on the right, which drops to 1 just to the left of the middle node and is then constant. This resembles a hard and a soft material joint just to the left of the middle node. The exact analytic value for strain is 0.1 in the hard region (left half) and 1 in the soft region (right half). On the other hand, if we look at the strain corresponding to the interpolated distribution of modulus given by putting (E_1, *E2, E3*) = (10, 1, 1) into Eq. (5.2), the exact analytical solution for the strain in this element is

$$\varepsilon(x) = \frac{1}{E(x)} = \frac{2}{9x^2 - 9x + 2}. \tag{5.10}$$

This solution is singular when the modulus goes to zero, shown in Fig. 5.9 for this element (noted as the "exact" solution). One can separate the interpolation for the material from that associated with the FEM solution (space and displacement). If we keep the quadratic interpolation (*mnpe* =3) for the modulus but now increase the order of the interpolation of position and displacement in an isoprametric sense (*nnpe* =3, 4, 10, 14), we observe that as the order of the element in the FEM solution goes up, the solution for the strain approaches the exact singular solution described in Eq. (5.10). This is expected since the FEM solution for the p-node element approaches the exact response for the material distribution given in Eq. (5.3) for *mnpe* =3. The extent of the problem generated from having the negative modulus region is clearly appreciated when one recalls that the actual strain field for the real problem never exceeds 1, while the strain field from our 3-node element interpolation of the material property in the actual problem approaches infinity as the sign of the modulus changes.

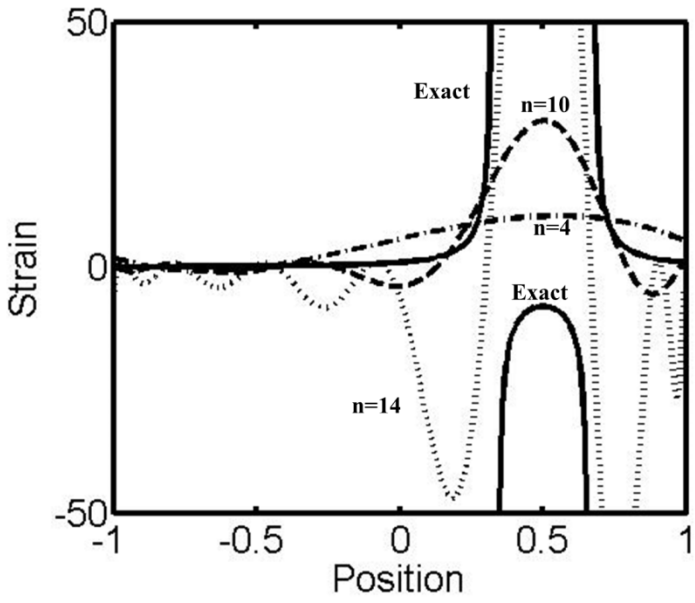

Figure 5.9 The strain distribution associated with the uniaxial extension problem when using a 3-node quadratic elements with (E_1, E_2, E_3) = (10, 1, 1), for the interpolation of the modulus, while using one, up to 14-node, p-type semi-isoparametric element for modeling position and displacement in the FEM solution. [91]

5.5 Semi-isoparametric element

The error in polynomial Lagrange-type graded elements can be reduced by separating the interpolation for the material property from that associated with space and displacement. Fig. 5.10 shows the solution using 3-node Lagrange interpolation for modeling material variation, while using 3- to 7-node Lagrange interpolation for capturing space and displacement. As can be seen, the solution for this semi-isoparametric element improves and approaches the exact solution as the number of nodes for the isoparametric space and displacement interpolation is increased.

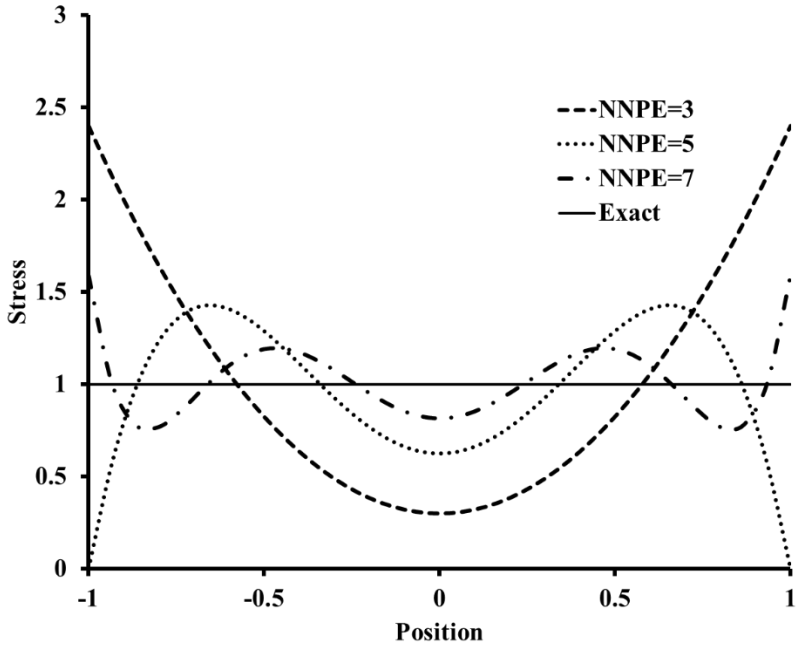

Figure 5.10 Stress distribution for the uniaxial extension problem described in Figure 5.3 using one semi-isoparametric element with material grading described using *mnpe* = 3 for (E_1, E_2, E_3) = (8, 1, 8), and different values of *nnpe* used to interpolate space and displacement. [91]

Tables 5.1-6 provide a picture of the error estimate, given in Eq. (5.8), for the uniaxial extension problem using a single fully-isoparametric element or using a single semi-isoparametric element. Tabels 1 and 2 show that for a 3-node fully-isotparametric element (*mnpe* = *nnpe* = 3), one my use the following rules of thumb for the given errors

$$\begin{aligned} 0.5 < \frac{G_1 G_3}{G_2^2} < 2 &\Rightarrow Err_\sigma < 1.2\times 10^{-2}, \\ 0.5 < \frac{G_1 G_3}{G_2^2} < 4 &\Rightarrow Err_\sigma < 5\times 10^{-2}. \end{aligned} \tag{5.11}$$

For a semi-isoparametric element using 3-node interpolation for material and a 5-node interpolation for space and displacement (*mnpe* = 3, *nnpe* = 5), Tables 5.3 and 5.5 show that one my use the following rules of thumb for the given errors as

$$0.5 < \frac{G_1 G_3}{G_2^2} < 2 \Rightarrow Err_\sigma < 2\times 10^{-4},$$
$$0.5 < \frac{G_1 G_3}{G_2^2} < 4 \Rightarrow Err_\sigma < 6.7\times 10^{-3}. \tag{5.12}$$

Tables 5.5 and 5.6 give the rule of thumb for *mnpe* = 3 and *nnpe* = 7 as

$$0.5 < \frac{G_1 G_3}{G_2^2} < 2 \Rightarrow Err_\sigma < 2\times 10^{-6},$$
$$0.5 < \frac{G_1 G_3}{G_2^2} < 4 \Rightarrow Err_\sigma < 8.6\times 10^{-4}, \tag{5.13}$$
$$0.05 < \frac{G_1}{G_2} < 8 \quad \& \quad 0.05 < \frac{G_3}{G_2} < 8 \quad \& \text{ Admissible} \Rightarrow Err_\sigma < 4\times 10^{-2}.$$

Also, for this higher order semi-isoparametric elements, the accuracy is such that one can get fairly accurate results as long as one stays inside the boundaries shown in Fig. 5.4 and stated in Eq. (5.6).

Table 5.1 The error relative to the exact solution of unit for the problem shown in Fig. 5.5 using a single 3-node fully-isoparametric elastic modulus graded element (*mnpe* = *nnpe* = 3). [91]

	E_3/E_2				
E_1/E_2	1	2	4	8	16
1	0	7.60E-3	3.35E-2	5.20E-1	3.69E+2
2	7.60E-3	5.00E-2	1.01E-1	2.13E-1	2.97E+0
4	3.35E-2	1.01E-1	2.00E-1	2.88E-1	5.85 E-1
8	5.20E-1	2.13E-1	2.88E-1	3.92E-1	4.96E-1
16	3.69E+2	2.97E+0	5.85 E-1	4.96E-1	5.56E-1

Table 5.2 The error relative to the exact solution of unit for the problem shown in Fig. 5.5 using a single 3-node fully-isoparametric elastic modulus graded element (*mnpe* = *nnpe* = 3). [91]

	E_3/E_2				
E_1/E_2	1	0.5	0.1	0.05	0.01
1	0	1.18E-2	8.50E-2	1.07E-1	1.28E-1
0.5	1.18E-2	1.28E-1	9.74E-2	1.15E-1	1.31E-1
0.1	8.50E-2	9.74E-2	1.47E-1	1.56E-1	1.72E-1
0.05	1.07E-1	1.15E-1	1.56E-1	1.72E-1	1.83E-1
0.01	1.28E-1	1.31E-1	1.72E-1	1.83E-1	1.94E-1

Table 5.3 The error relative to the exact solution of unit for the problem shown in Fig. 5.5 using a single 3-node quadratic interpolation for describing elastic modulus grading (*mnpe* = 3) and a 5-node semi-isoparametric element for interpolating space and displacement (*nnpe* = 5). [91]

	E_3/E_2				
E_1/E_2	1	2	4	8	16
1	0	2.06E-5	6.70E-3	5.21E-1	1.13E+1
2	2.06E-5	1.50E-3	4.90E-3	9.41E-2	1.18E+2
4	6.70E-3	4.90E-3	2.49E-2	4.99E-2	9.29E-1
8	5.21E-1	9.41E-2	4.99E-2	1.11E-1	2.02E-1
16	1.13E+1	1.18E+2	9.29E-1	2.02E-1	2.68E-1

Table 5.4 The error relative to the exact solution of unit for the problem shown in Fig. 5.5 using a single 3-node quadratic interpolation for describing elastic modulus grading (*mnpe* = 3) and a 5-node semi-isoparametric element for interpolating space and displacement (*nnpe* = 5). [91]

	E_3/E_2				
E_1/E_2	1	0.5	0.1	0.05	0.01
1	0	1.77E-4	1.88E-2	3.56E-2	6.17E-2
0.5	1.77E-4	6.17E-2	2.07E-2	3.52E-2	5.61E-2
0.1	1.88E-2	2.07E-2	4.29E-2	5.59E-2	7.36E-2
0.05	3.56E-2	3.52E-2	5.59E-2	6.83E-2	8.50E-2
0.01	6.17E-2	5.61E-2	7.36E-2	8.50E-2	1.01E-1

Table 5.5 The error relative to the exact solution of unit for the problem shown in Fig. 5.5 using a single 3-node quadratic interpolation for describing elastic modulus grading (*mnpe* = 3) and a 7-node semi-isoparametric element for interpolating space and displacement (*nnpe* = 7). [91]

	E_3/E_2				
E_1/E_2	1	2	4	8	16
1	0	1.25E-6	8.63E-4	1.338E-1	1.83E+0
2	1.25E-6	6.57E-5	4.66E-4	4.10E-2	5.98E+0
4	8.63E-4	4.66E-4	2.80E-3	8.40E-3	1.12E+0
8	1.338E-1	4.10E-2	8.40E-3	2.69E-2	7.63E-2
16	1.83E+0	5.98E+0	1.12E+0	7.63E-2	1.087E-1

Table 5.6 The error relative to the exact solution of unit for the problem shown in Fig. 5.5 using a single 3-node quadratic interpolation for describing elastic modulus grading (*mnpe* = 3) and a 7-node semi-isoparametric element for interpolating space and displacement (*nnpe* = 7). [91]

	E_3/E_2				
E_1/E_2	1	0.5	0.1	0.05	0.01
1	0	3.83E-6	4.40E-3	1.33E-2	3.72E-2
0.5	3.83E-6	4.03E-5	5.00E-3	1.33E-2	3.30E-2
0.1	4.40E-3	5.00E-3	1.25E-2	2.10E-2	3.86E-2
0.05	1.33E-2	1.33E-2	2.10E-2	2.93E-2	4.65E-2
0.01	3.72E-2	3.30E-2	3.86E-2	4.65E-2	6.26E-2

5.6 Two-dimensional quadrilateral elements

It is natural to wonder whether similar problems, like getting negative moduli, and their consequently unrealistic stress and strain fields can be observed for 2- and 3-D

problems. This can easily be demonstrated for a 2-D linear-elastic element using the standard 9-node (3x3) bi-quadratic element for interpolating the elastic modulus values in the element based on the nodal values. In this case, consider the problem of uniaxial extension of a 2x2 square part, as shown in Fig. 5.11, containing a hard circular region of Young's modulus 20 and diameter 0.9, with the balance having a modulus of 1. Assume the Poisson ratio does not change and is given as 0.3. Due to symmetry of the problem, we model the top right quarter of the part, imposing an applied horizontal traction of one on the right side, zero traction on the top, zero vertical displacement on the bottom, and zero horizontal displacement on the left. We cover this section with a single 9-node element. Due to the distribution of properties, we assign a Young's modulus of 20 to the bottom left node and a Young's modulus of 1 to the other 8 nodes. Fig.5.11 shows the horizontal stress distribution obtained from the FEM analysis. This stress ranges from negative 52.8 to positive 14.5. The figure also shows the regions of negative modulus resulting from the 9-node interpolation of the nodal elastic moduli and the regions of negative stress in the FEM solution. As can be seen, large areas of negative stress shows up when the plate is under tension, which indicates that the fully-isoparametric (material, position and displacement) p-type graded finite elements may have difficulty modelling some inhomogeneous bodies accurately. One can somewhat avoid this problem by checking that the rows and columns of nodal moduli each are admissible for the associated one dimensional three-node elements. Even though this does not fully eliminated the possibility of regions of negative modulus, it can minimize this possibility. Thus, for a fully-isoparametric 9-node quadrilateral element one would restrict the moduli at the corner nodes to be between 0.5 to 2 times the associated mid-side node

moduli, and the mid-side node moduli to be between 0.5 to 2 times the modulus at the central node. Similar rules may be used for three-dimensional fully-isoparametric 27-node brick elements.

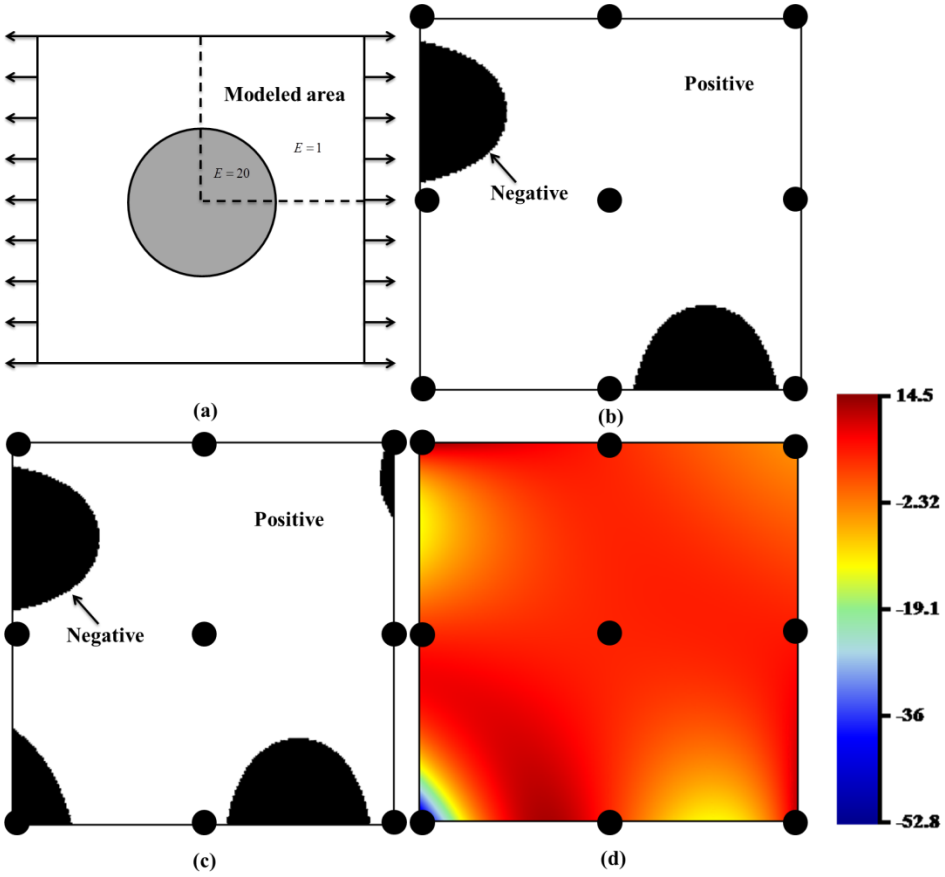

Figure 5.21 A part with a hard central core under uniform horizontal extension, (a) whole part under extension, (b) the sign of the modulus of a quarter of the part (black is a negative modulus), (c) the sign of the stress distribution of a quarter of the part (black is negative stress), (d) stress distribution of a quarter of the part. [91]

5.7 Discussion

Most previous work on simulating the response of FGMs using graded finite elements focus on very gradually varying properties for which the occurrence of regions of negative modulus is unlikely even for higher order fully-isoparametric elements [10-14]. As a result, these works focus on the positive characteristics of the higher order

elements without observing the potentially large errors that can sometimes occur in problems that show large variation in properties, such as is seen between a fiber and the matrix in a fiber-reinforced composite, a problem similar to that shown in Figure 5.11.

The issue of getting regions of negative modulus while starting from positive nodal moduli is one that should be carefully considered when using automatic mesh generation for a graded FEM, or when optimizing the distribution of properties in a part. The former can result in meshes with elements that inherently have very poor performance. The latter can result in searches that produce positive nodal properties that give poor FEM performance, distorting the optimization strategy.

The error given in Tables 5.1-6 show that material grading in the element, even when the nodal moduli are admissible, can produce large errors in the solution. In general, increasing the order of interpolation for obtaining the solution (i.e., increasing *nnpe*) without increasing the order of interpolation for the material properties (*mnpe*) is very desirable. As shown in the tables, as long as the interpolation for the modulus remains admissible, the performance of the element improves with higher *nnpe*.

This chapter demonstrates a possible problem with p-type higher order fully-isoparametric graded finite element methods resulting from development of regions of property sign reversal even when having only positive nodal properties. For many properties, such as the elastic Young's modulus, regions of negative modulus are not physically admissible, and the solution to the FEM clearly indicates large errors when such regions appear in the element. For constant and linearly varying properties in the element, positive nodal properties will produce only positive interpolations in the element.

This is not true for quadratically varying properties. For 3-node quadratic line elements, it is shown that one can clearly separate the space of positive nodal properties into admissible and inadmissible regions. The inadmissible regions produce islands of negative valued properties in the element and thus need to be avoided. Simple rules of thumb can be used for materially graded elements to avoid nodal properties that produce large errors. Mixed semi-isoparametric elements that use admissible nodal properties are shown to give good accuracy. These semi-isoparametric elements use the 3-node quadratic interpolation to model the property variation, while using higher order interpolations for space and displacement. Rules of thumb are developed to estimate the range of nodal properties that produce high accuracy results.

Chapter 6 Optimal material grading for maximizing load capacity

6.1 Introduction

Most FGM parts described in the literatures adopt simple grading that is typically only in one direction [83-85]. For a bulk FGM part, there are infinite patterns of material variation so there can be an optimal choice of FGM distribution, which achieves better performance than material variation in any single direction. Optimization of FGM parts has been studied for different applications [95-101]. For example, the peak thermal stress of a Ni-Al_2O_3 FGM transition plate was minimized by Cho and Ha [95] using volume fraction optimization by a grading that divided the part into parallel uniform homogenized sub-layers. This was done using bilinear isoparametric elements, interior penalty-function method and the golden section method to analyze and optimize the problem and show that the peak stress could be reduced by 47%. The element-free Galerkin method (EFG) was employed by Goupee and Vel [96] to analyze a 2D functionally graded material plate showing that in comparison to FEM, the EFG method has higher rates of convergence, smoother stress distribution and no need for nodal connectivity data. They used the Range-restricted bicubic interpolation technique devised by Brodlie et al. [102] since the optimization variables were always within two bounds, and could optimize the distribution using genetic algorithms. In this case, the maximum thermal stress of the same Ni-Al_2O_3 plate described above was shown to reduce by 69%. Taheri et al. [97] have proposed a NURBS-based FEM isogeometrical approach. Surfaces created by NURBS have a strong convex hull property and good continuity. In this case the same parameterization of the computational domain for both the geometric

(computational) and the material model was used. This allowed calculation of variable material properties at the Gauss points by taking their parametric coordinates from the computational model. For this case, the same optimization problem of a Ni-Al_2O_3 plate was solved and the result was close to those reported by Goupee and Vel. Kou et al. [98] proposed a feature tree based procedural model to capture generic material heterogeneities instead of using the explicit functional models used up to this point. This allowed more than one explicit function to describe versatile material gradations, and the material composition at a given location was then obtained by execution of customizable procedures. They used a Particle Swarm Optimization (PSO) method to show that functional grading can be efficiently optimized.

In this chapter we study the problem of designing functionally graded parts for a class of IPNs that show linear elastic response, and allow two to three orders in variation of the elastic modulus and one decade of change in the fracture stretch. Since the material shows linear elastic response, we construct an optimization procedure that takes advantage of this fact to fairly rapidly converge on to an optimal solution. For the examples shown, the improvement in load carrying capacity is two to three times, which may be interpreted also as a potential for substantial reduction in weight. This benefit comes from the competition between changes in modulus and ultimate stress capacity for this IPN system, and represents a realistic potential that may be achieved if one produces a printer to construct the proposed grading.

We start by giving the material and associated properties for the IPN system. These are presented in terms of the ratio of the components, which in the following

sections is used as the parameter for variation of functional grading. This is followed by describing the optimization process we considered, which is based on a finite element method (FEM) solver that uses materially graded elements defined by giving the nodal properties. Since the problem is linear before failure, we use a scaling method to efficiently solve the ultimate load problem. A general purpose optimization code is then attached to the mechanical analysis to obtain the optimal grading of the part. This method is used to optimize the grading of the IPN system in two examples. One is for a plate under tensile loading that contains a hole, and the other is for the loading of a bent bracket. In each case the optimized grading performs over one hundred percent better than any uniform part made from this IPN system. The level of improvement is closely related to the IPN system used and may be more or less significant depending on the relative change of stiffness and fracture properties for the IPN system.

6.2 Materials and Modeling: acrylate/epoxy IPNs

The material used for this study is an IPN system made from acrylate and epoxy components that were simultaneously cured in mixture. Acrylate/epoxy IPNs have been the subject of development and study for a long time [20, 103, 104]. In this case, the acrylate component was Bisphenol A propoxylate diacrylate (BPA-PDA) with 15 repeating units (m=n=15) that was photo cured with the help of the photo initiator 2-hydroxy-2-methylpropiophenone. The epoxy component was 3,4-epoxycyclohexylmethyl 3,4-epoxycyclohexanecarboxylate (ECH) that was photo cured with the help of the photo initiator Triarylsulfonium hexafluoroantimonate mixed at 50% weight with propylene carbonate. All components were purchased from Sigma-Aldrich®.

Different fractions of acrylate and epoxy were used to obtain IPN systems that ranged from pure acrylate to pure epoxy. The components were photo cured under a metal halide Dymax® 5000 polychromatic lamp. The details of this preparation are reported in Butterfield et al. [105, 106]. The samples made in this way were evaluated by uniaxial mechanical testing in tension using stereo-optical DIC (Aramis) for full surface strain measurements. The response of the samples as a function of epoxy content is given in Fig. 6.1 for uniaxial extension.

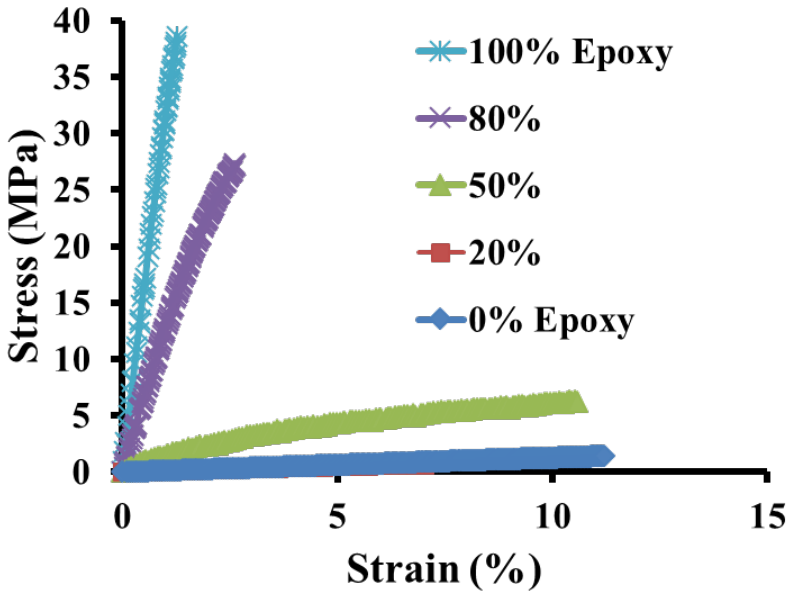

Figure 6.1 Stress-strain response of uniaxial extension of a non-post cured acrylate/epoxy IPN systems at different fractions of epoxy

The response in uniaxial extension was used to extract the elastic modulus, Poisson's ratio, and stress at fracture for these IPN systems, shown in Fig. 6.2-4. The properties of the IPNs, which are made from long acrylic and short epoxy units, showed

two orders of magnitude variation of the Young's modulus E, and one order of magnitude variation in the ultimate failure stress σ_u. The variation of the Poisson's ratio ν was smaller and transitioned from close to incompressible rubbery acrylate to the rigid, but compressible, epoxy.

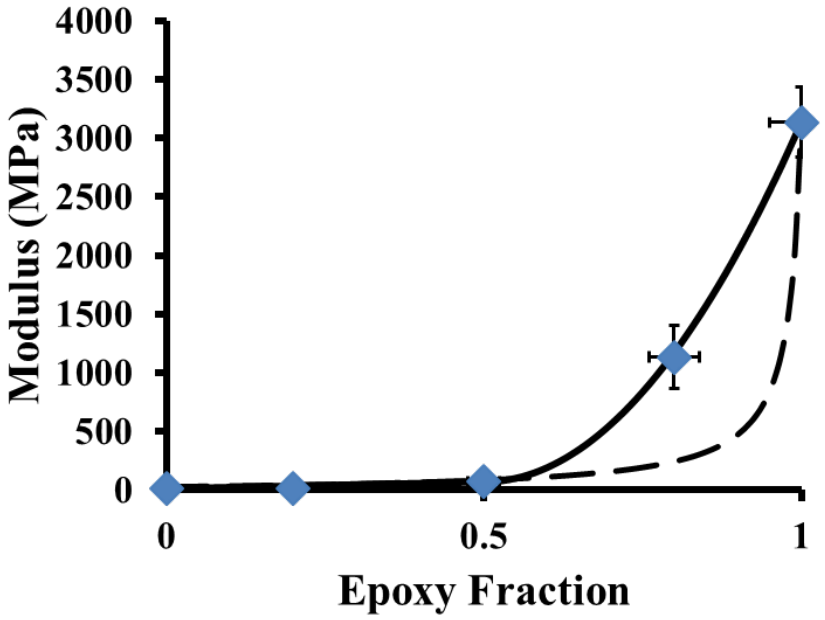

Figure 6.2 Modulus of a non-post cured acrylate/epoxy IPN systems at different fractions of epoxy (dash line is the Mori-Tanaka approximation)

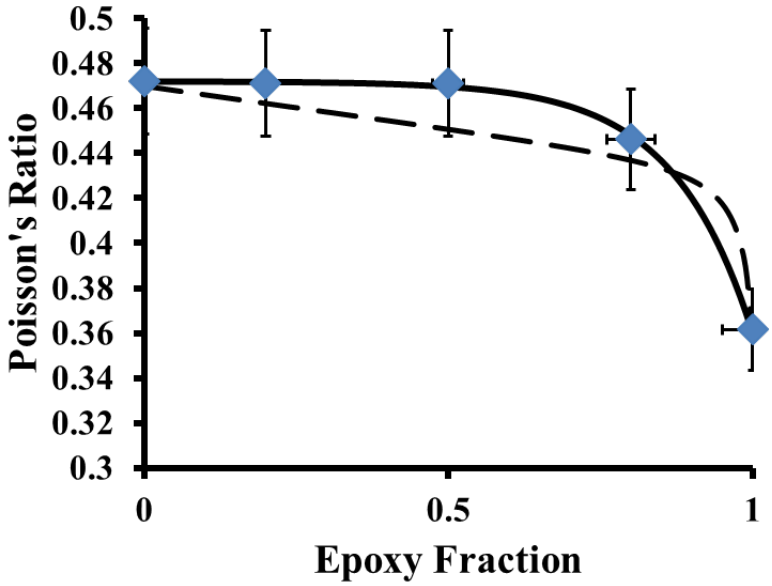

Figure 6.3 Poisson's ratio of a non-post cured acrylate/epoxy IPN systems at different fractions of epoxy (dash line is the Mori-Tanaka approximation)

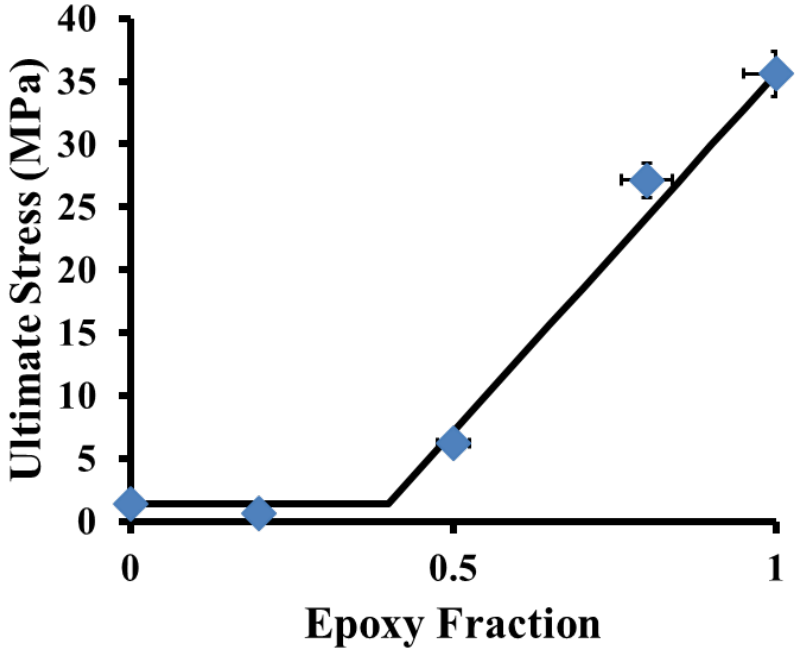

Figure 6.4 Ultimate fracture stress of a non-post cured acrylate/epoxy IPN systems at different fractions of epoxy

For modeling the response, we assume the material is linear, elastic, and isotropic so that the stress $\boldsymbol{\sigma}$ in terms of the infinitesimal strain $\boldsymbol{\varepsilon}$, given by the generalized Hooke's law $\boldsymbol{\sigma} = \mathbf{E} : \boldsymbol{\varepsilon}$, can be written as

$$\boldsymbol{\sigma} = \kappa\, tr(\boldsymbol{\varepsilon})\mathbf{I} + G\boldsymbol{\varepsilon}, \tag{6.1}$$

where $\mathbf{I}$ denotes the identity, $tr(\boldsymbol{\varepsilon})$ denotes the trace of the strain, and the bulk modulus κ and the shear modulus G are, respectively, given in terms of the measured Young's modulus and Poisson's ratio by

$$\kappa = \frac{E}{3(1-2\nu)}, \quad G = \frac{E}{2(1+\nu)}. \tag{6.2}$$

Failure in general loading was assumed to occur when the maximum principal stress at a point reached the ultimate stress at failure in tension. For these acrylate/epoxy IPN systems, the material response was modeled, as shown in Fig. 6.2-4, by

$$\begin{aligned} E &= \begin{cases} 12.8 + 115\alpha \text{ MPa}, & \alpha < 0.5, \\ 70.3 + 12260(\alpha - 0.5)^2 \text{ MPa}, & \alpha \geq 0.5, \end{cases} \\ \nu &= 0.472 - 0.112 e^{\frac{\alpha - 1}{0.13}}, \\ \sigma_u &= \begin{cases} 1.41 \text{ MPa}, & \alpha < 0.4, \\ 1.41 + 57.0(\alpha - 0.4) \text{ MPa}, & \alpha \geq 0.4, \end{cases} \end{aligned} \tag{6.3}$$

where α represents the fraction of epoxy in the IPN system so that it varies from 0 to 1, respectively going from pure acrylate to pure epoxy. As reference, the Mori-Tanaka [79] approximation for spherical inclusion given by Berryman [107] is noted on the figure,

which is frequently used to model the variation of properties in mixtures and discussed in Chapter 4 [108]. As can be seen, the IPN system does not follow this rule.

6.3 Optimization Strategy for Material Grading

Optimal grading for this IPN system was evaluated by attaching a general purpose optimization program to an in-house FEM solver that used graded elements to solve for the mechanical response. The grading of the part was defined and transferred to the FEM solver by prescribing the epoxy fraction at the FEM model nodes. In each optimization step, the optimizer selected these nodal fractions and transferred them to the FEM solver. The FEM solver solved the problem for the given boundary conditions and then, using the linearity described below, scaled the solution to find the maximum load capacity of the part for the prescribed grading. This load was then returned to the optimizer as the value of the objective function. The optimizer, based on this value, altered the grading and the process was repeated until an optimum grading was obtained.

We considered the problem of material property variation in the context of optimizing the grading by varying the ratio of the components in a two component IPN system as described in the previous section. For modeling the grading of the material, we assume that the concentration of the second component is denoted by α, a number between zero and one, that varies with position $\mathbf{X}$ in the body $\mathcal{B}$, shown in Fig. 5.1, where Ω denotes the domain of the body and Γ its boundary. This concentration distribution is assumed to uniquely define the properties of the material at each point, which in our problem will be the elastic modulus E, the Poisson's ratio ν, and the ultimate stress at failure σ_u.

We focus on optimization problems that can be written in terms of an objective function Φ of the distribution $\alpha(\mathbf{X})$. The optimization of the material grading was defined as the minimization of Φ for all admissible variations of $\alpha(\mathbf{X})$ on the body. The optimal distribution $\alpha(\mathbf{X})$ is thus given by the solution to

$$\min_{\alpha(\mathbf{X}),\, \mathrm{X}\in\Omega} \Phi[\alpha(\mathbf{X})], \tag{6.4}$$

where $\alpha(\mathbf{X})$ is any function with values from 0 to 1 defined over the body, $\mathbf{X} \in \Omega$, and subject to the condition that a given norm of the stress $\|\boldsymbol{\sigma}\|$, in our case the maximum principal stress, at each point of the body is less than or equal to its maximum allowable value $\sigma_u[\alpha(\mathbf{X})]$.

The general problem we considered is for the response of a linear elastic material with constitutive equation described by a generalized Hooke's law $\boldsymbol{\sigma} = \mathbf{E} : \boldsymbol{\varepsilon}$, where the fourth order tensor of moduli is given in terms of the concentration α, which varies with the location in space, so that $\mathbf{E}[\alpha(\mathbf{X})]$. Fig. 6.5 shows a schematic of a general problem, which is of a body of density ρ subjected to a body force $\mathbf{b}$, and under displacement $\mathbf{u}$ and traction $\mathbf{t}^{(n)}$ boundary conditions. The equilibrium problem is written as

$$div(\boldsymbol{\sigma}) + \rho\mathbf{b} = \mathbf{0}, \quad \forall \mathbf{X} \in \Omega \tag{6.5}$$

subject to the boundary conditions

$$\begin{aligned} &\mathbf{u} = \mathbf{u}_b \text{ on } \Gamma_u, \\ &\mathbf{t}^{(\mathrm{n})} = \mathbf{t}_b \text{ on } \Gamma_t, \end{aligned} \tag{6.6}$$

where $\mathbf{u}_b$ and $\mathbf{t}_b$ are, respectively, the imposed displacement and traction conditions [109]. This is the problem that the FEM solver solves by satisfying the symmetric weak formulation given by

$$\int_{\Gamma} \overline{\mathbf{u}} \circ \mathbf{t}^{(\mathrm{n})} d\Gamma - \int_{\Omega} \nabla \overline{\mathbf{u}} : \mathbf{E} : \nabla \mathbf{u} d\Omega + \int_{\Omega} \rho \overline{\mathbf{u}} \circ \mathbf{b} d\Omega = 0 \quad \forall \overline{\mathbf{u}}(\mathbf{X}) \text{ on } \Omega, \tag{6.7}$$

which is obtained from Eq. (6.5) by introducing Hooke's law, Cauchy's relation $\mathbf{t}^{(\mathrm{n})} = \hat{\mathbf{n}}\boldsymbol{\sigma}$, the expression for infinitesimal strain

$$\boldsymbol{\varepsilon} = \frac{1}{2}\left(\nabla \mathbf{u} + \nabla \mathbf{u}^{\mathbf{T}}\right), \tag{6.8}$$

an arbitrary weighting function $\overline{\mathbf{u}}(\mathbf{X})$ and standard associated arguments [110]. The formulation in Eq. (6.8) must be forced to satisfy the intrinsic displacement boundary conditions.

A problem of interest, for example, may be to maximize the load P along the direction $\hat{\mathbf{e}}$ that can be applied on a section of the surface of the body denoted by Γ_P, as shown in Fig. 6.5. To cast this as an optimization problem for the distribution $\alpha(\mathbf{X})$, one would define the objective function as

$$\Phi = -P = -\hat{\mathbf{e}} \circ \int_{\Gamma_P} \mathbf{t}^{(n)} d\Gamma. \tag{6.9}$$

To conceptually solve this problem by the finite element method, one may select a distribution $\alpha_o(\mathbf{X})$ and increase the load P until one point in the body reaches the

associated ultimate stress $\sigma_u[\alpha_o(\mathbf{X})]$. Taking this as the maximum load, say $P_{\max}$, one would then change the distribution, say to $\alpha_1(\mathbf{X})$, and again gradually increase the load P until the first point fails. If this load is larger than $P_{\max}$, it would be used as the new value of $P_{\max}$, and if not, it would be discarded. The process could be continued using some method of selecting new distributions $\alpha(\mathbf{X})$ until one converged onto the distribution that provides the maximum possible applied load. In this process, multiple FEM solutions are needed to find the maximum allowable load for each selected distribution $\alpha(\mathbf{X})$. Since FEM solutions are time and resource intensive, these multiple FEM solutions per material grading account for a large part of the cost in implementing this procedure.

General purpose optimizers differ in how they select or change the distribution $\alpha(\mathbf{X})$ and, thus, show different levels of success depending on the problem, but all would require multiple FEM solutions for each selected material distribution to find the load at which the body start to fail. The linearity in the resulting equations can be used in certain problems to avoid the need for these multiple FEM solutions for each distribution $\alpha(\mathbf{X})$. For example, if the solution somehow scales, one may be able to use a single FEM solution per material distribution to get the value of the maximum allowable load. In general, the linear elasticity problem scales as follows. Given a solution $\mathbf{u}(\mathbf{X})$ to the equilibrium Eq. (6.5) and its associated boundary conditions in Eq. (6.6), one can always construct a scaled solution $\mathbf{u}^*(\mathbf{X}) = \beta\mathbf{u}(\mathbf{X})$, for a given constant β, that satisfies the equilibrium equation

$$div(\boldsymbol{\sigma}^*) + \rho \mathbf{b}^* = \mathbf{0}, \quad \forall \mathbf{X} \in \Omega \tag{6.10}$$

subject to the boundary conditions

$$\begin{aligned} \mathbf{u}^* &= \beta \mathbf{u}_b \text{ on } \Gamma_u, \\ \mathbf{t}^{(\mathrm{n})^*} &= \beta \mathbf{t}_b \text{ on } \Gamma_t, \end{aligned} \tag{6.11}$$

if the associated stress $\boldsymbol{\sigma}^*(\mathbf{X})$ and the body force $\mathbf{b}^*(\mathbf{X})$, respectively, have the characteristic that $\boldsymbol{\sigma}^*(\mathbf{X}) = \beta\boldsymbol{\sigma}(\mathbf{X})$ and $\mathbf{b}^*(\mathbf{X}) = \beta\mathbf{b}(\mathbf{X})$. From the Eq. (6.7) we have $\boldsymbol{\varepsilon}^*(\mathbf{X}) = \beta\boldsymbol{\varepsilon}(\mathbf{X})$, and thus from Hooke's law we can show that $\boldsymbol{\sigma}^*(\mathbf{X}) = \beta\boldsymbol{\sigma}(\mathbf{X})$ under all conditions. Thus, the linear elastic equilibrium problem with no body forces scales linearly for problems that have linearly scaled boundary conditions. In addition, from Cauchy's relation one can show that the scaled problem's loading is given by

$$P^* = \beta P. \tag{6.12}$$

Thus, finding the load capacity of a problem that scales can be done by scaling a single solution until the first point in the body reaches its failure condition. This allows using a single FEM solution per material distribution to calculate the largest load the body can carry. In the following examples we consider problems for which we neglect the body force, and only select problems with boundary conditions that scale as described in Eq. (6.12). This substantially reduces the number of FEM solutions.

To calculate the scaling of the FEM solution $\boldsymbol{\sigma}(\mathbf{X})$ for each optimization step, we need to evaluate the maximum possible scaling factor such that the part will not fail. For a given material grading $\alpha(\mathbf{X})$, this can be written as

$$\beta = \min_{\mathbf{X}\in\Omega} \frac{\sigma_u[\alpha(\mathbf{X})]}{\|\boldsymbol{\sigma}(\mathbf{X})\|}. \tag{6.13}$$

The failure condition is based on the largest tensile principal stress. Since the ultimate stress varies with the concentration $\alpha(\mathbf{X})$ in the element, we evaluated the minimum scaling for each element by calculating the scaling on regular grid points in the element. The grids were sequentially refined until the minimum scaling converged. In each case the grid sequence on the parametric element was 4x4, 8x8, 16x16, 32x32, and 64x64. Once the minimum for an element was calculated, it was compare with the minimum for the other elements, proceeding until the minimum in the body was evaluated. Thus, at each optimization step we had one FEM solution, and one search through the elements for the scaling factor. This process is depicted in the flow chart given in Fig. 6.5.

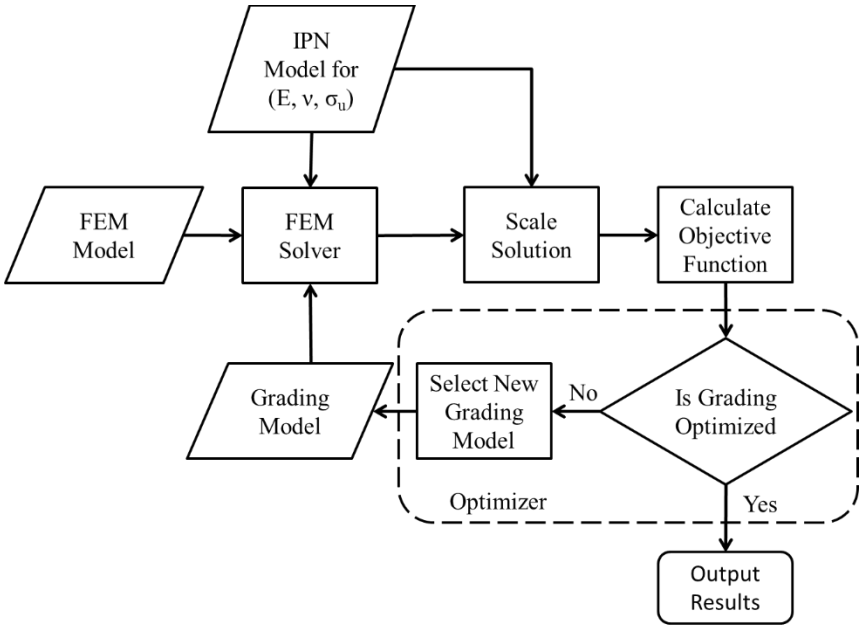

Figure 6.5 Flow chart of the grading optimization procedure.

One may use many ways to define and solve FEM problems for bodies with inhomogeneous material property distributions [88, 90, 92, 93]. We selected to use a graded element, where the properties are defined by an interpolation of nodal values. As described by Matsui and Terada [111] and Chen and Negahban [91], higher order interpolation for material properties can produce regions of negative modulus values in an element, even when all the nodal moduli are positive. This has been shown to drastically affect the quality of the graded FEM simulation. To avoid this in the higher order elements, one needs to control the range of nodal moduli [91]. Since we would like to use general purpose optimization codes, it is undesirable to do this. A simple solution is to use a close to liner interpolation for the material, which avoids the problem. To achieve this, we used bi-quadratic four node elements for grading the material, while at the same time using higher order (p-type) elements for the displacement. In practice, this is equivalent to constructing elements with two sets of shape functions so that one can set and interpolate properties based on values at the corner nodes of the element, while the displacement is interpolated on a larger number of nodes.

6.4 Demonstrations

We demonstrate the grading optimization for two problems. First is a rectangular plate with a hole. This problem shows that the graded plate has a load capacity over 140% higher than the best uniform plate made from the same IPN system. The second problem is an L-shaped bracket. This problem shows that the graded bracket has a load capacity over 110% higher than the best uniform IPN bracket. In each case, in addition to the optimal grading, information on the sensitivity of the load capacity to variations of the

grading is also provided. This would be important, for example in manufacturing graded IPN parts, to identify what characteristics of the grading are most important to capture.

The FEM models for these examples used quadrilateral elements with parametric structure as shown in Fig. 6.7. As can be seen, the material variation was approximated using a four node parametric element, while the position and displacement used p-type isoparametric interpolations having 16 to 36 nodes, selected to get convergence for the problem.

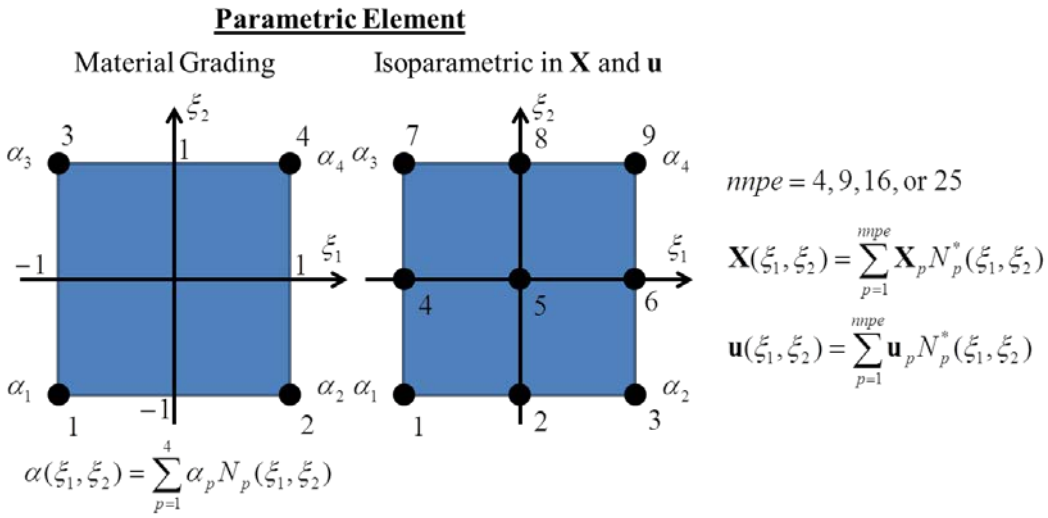

Figure 6.6 Parametric element with four node approximation for material distribution, and varied isoparametric approximations for position and displacement.

The optimization of the grading was done using an open source C++ optimization library called Dlib [112]. Dlib is based on Michael Powell's nonlinear derivative-free bound constrained optimization method BOBYQA [113]. The algorithm applies a trust region method that forms quadratic models by interpolation. There is freedom in the interpolation conditions, which is taken up by minimizing the Frobenius norm of the change to the second derivative of the model, beginning with the zero matrix, so that no

explicit first gradient of the objective function Φ is required. The optimization variables to vary were selected as the nodal values of α at the corner nodes of the elements. These corner node concentrations were each denoted as α_i and the array of all such corner node concentrations is denoted by $\boldsymbol{\alpha}$. The optimizing program allows values of the variables to be constrained by upper and lower bounds, which fits the requirement that each α_i stay between 0 and 1. This also allows restriction of the α_i to smaller variations.

In each case the sensitivity of the objective function Φ to variation of each nodal α_i was evaluated by looking at the variation in the function normalized to its value at the optimal grading $\boldsymbol{\alpha}_o$. For each case the first derivative, curvature, and variation for a fixed offset error of 5% in was calculated for each α_i. The slope and curvature were evaluated by fitting the variation of the normalized objective function around its optimal value using a quadratic regression to the values of the objective function measured for 5% increments over a ±15% interval (7 points for each α_i). For each α_i, the normalized objective function for n nodal values at the optimal grading given by $\boldsymbol{\alpha}_o$, the slope, the curvature, and the 5% offset were calculated using

$$
\begin{aligned}
y(\alpha_i) &= \frac{\Phi(\alpha_{1o},\ldots,\alpha_i,,\ldots,\alpha_{no})}{\left|\Phi(\alpha_{1o},\ldots,\alpha_{io},,\ldots,\alpha_{no})\right|}, \\
y'(\alpha_i) &= \frac{dy(\alpha_i)}{d\alpha_i}, \\
\kappa(\alpha_i) &= \frac{\left|\dfrac{d^2 y(\alpha_i)}{d\alpha_i^2}\right|}{\left[1+y'^2(\alpha_i)\right]^{\frac{3}{2}}}, \\
\Delta y_{5\%} &= \max\left[\left|y(\alpha_{io}+0.05)\right|,\left|y(\alpha_{io}-0.05)\right|\right].
\end{aligned}
\tag{6.14}
$$

The first derivative of the objective function at the optimal point is supposed to be close to zero, while the curvature κ_i should represent how sensitive the objective function is to "finite" changes in the given nodal concentration. The current uncertainty in printing properties can be large so the 5% offset might provide a more realistic measure of the sensitivity of the solution to changes in the grading [9]. Also, the slope need not be zero due to constraints imposed in the FEM solution boundary conditions and limitations resulting from the mesh size so it is useful to visualize the slope in addition to the curvature and 5% offset. These are demonstrated in the demonstrations.

6.4.1 Optimal grading for a plate with a hole

The first demonstration is for calculating the optimal grading of a rectangular plate under tension with a centrally located hole as shown in Fig. 5a. There is an analytical solution for a homogenous isotropic plate with a hole [114], which gives the stress distribution and its concentration at the hole. This problem has also been studied as an example for using FGM systems under mechanical and thermal loading [93, 97] since the stress concentration at the hole limits the maximum applied load to about one third the load that can be applied to a uniform plate without a hole.

Due to the symmetry of the problem, as shown in the Fig. 6.8(b), one quarter of the plate is modeled for the FEM analysis. The vertical displacement on the bottom boundary, and the horizontal displacement on the left boundary are restricted due to this symmetry. The top boundary and the hole surface are stress free. The right boundary is uniformly displaced along the horizontal direction, while leaving the vertical displacement to freely adjust as needed. To guarantee the convergence of the solution,

the FEM solution was calculated with 8x10=80 to 12x14=168 elements, while the elements were varied from 4x4=16 to 6x6=36 nodes per element. The optimized load capacity did not vary more than 2.5% with these variations and the number of optimization steps did not change substantially, even though the time for each optimization step changed substantially. The optimization was started using the properties of uniform epoxy (i.e., $\alpha = 1$ at all corner nodes).

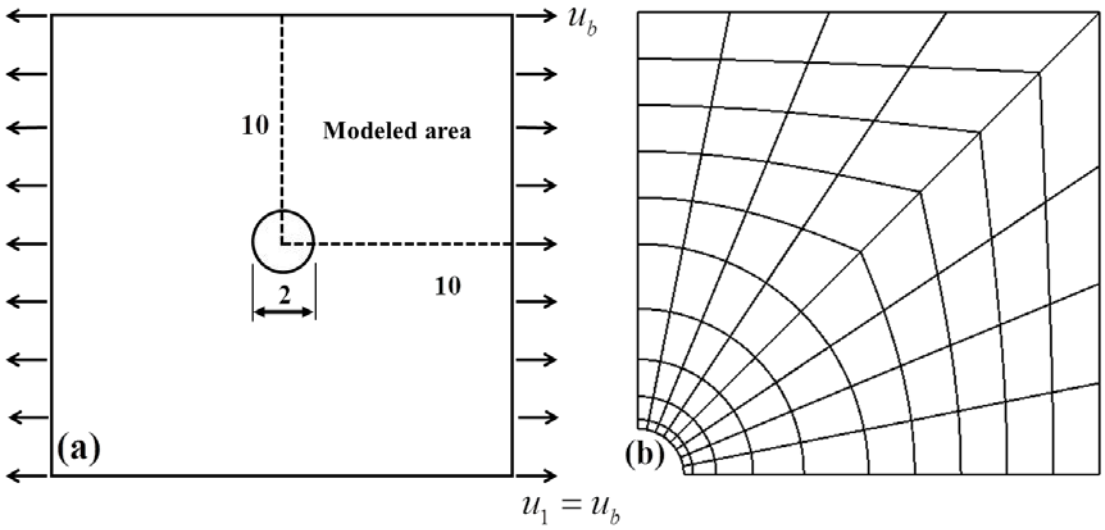

Figure 6.7 Optimization problem: (a) square plate with a circular hole in the middle, (b) FEM model of a quarter of the plate.

The objective function for optimization was taken as negative the applied load on the displaced surface at failure. This was calculated by integrating the horizontal component of stress over the right vertical surface. For comparison, the same load capacity was calculated for uniform samples constructed with different concentrations α of the IPN system. For the uniform samples, the highest load capacity is given by the material made of pure epoxy ($\alpha = 1$). The horizontal stress distribution for uniform epoxy is shown in Fig. 6.9(a). The same stress distribution for an optimally graded material is

shown in Fig. 6.9(b), where the grading is such that most of the material is carrying relatively high stresses. For a uniform body, the solution gives a stress concentration at the hole, which controls the failure of the part, and which leaves most of the part at stresses approximately one third the intrinsic ultimate stress of the material. In the case of the graded part, the grading removes the stress concentration so that most of the material can reach the high stresses. Fig. 6.10 shows the load capacity for uniform IPN plates and that of the optimized IPN grading. When calculating the load capacity of the graded plate and comparing it to the highest load capacity for a uniform IPN of the same system, it is seen that the load capacity is increased by a factor of 2.46, which can also be interpreted as the possibility to reduce the mass (thickness) by 59%. The optimized grading is shown in the insert of Fig. 6.10. Even though the variation of ultimate stress plays a role in the observed improvement, the figure indicates that slightly softer material put strategically adjacent to the hole reduces the stress concentration, essentially protecting the hole and thus allowing the material in the balance of the body to carry load near its intrinsic load capacity. To the best knowledge of the authors, an improvement of this magnitude in the load capacity by using functional grading has not yet been reported for this problem.

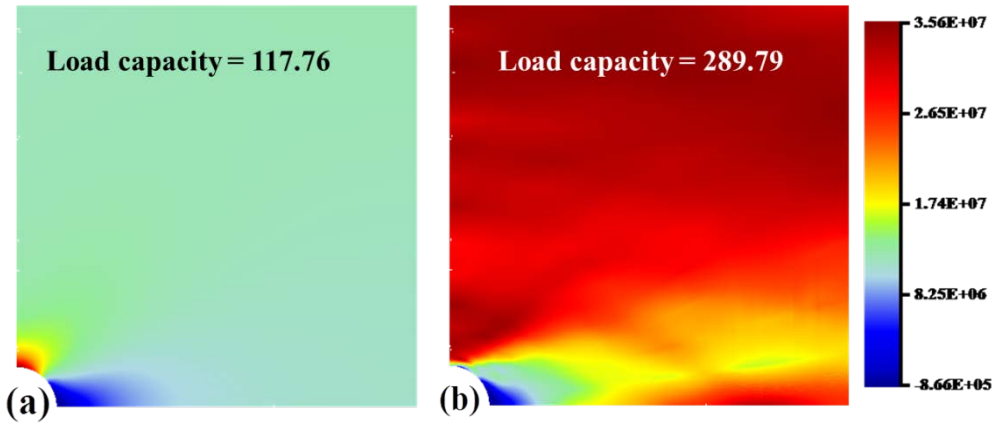

Figure 6.8 Horizontal tensile stress for (a) uniform epoxy, and (b) optimized acrylate/epoxy IPN.

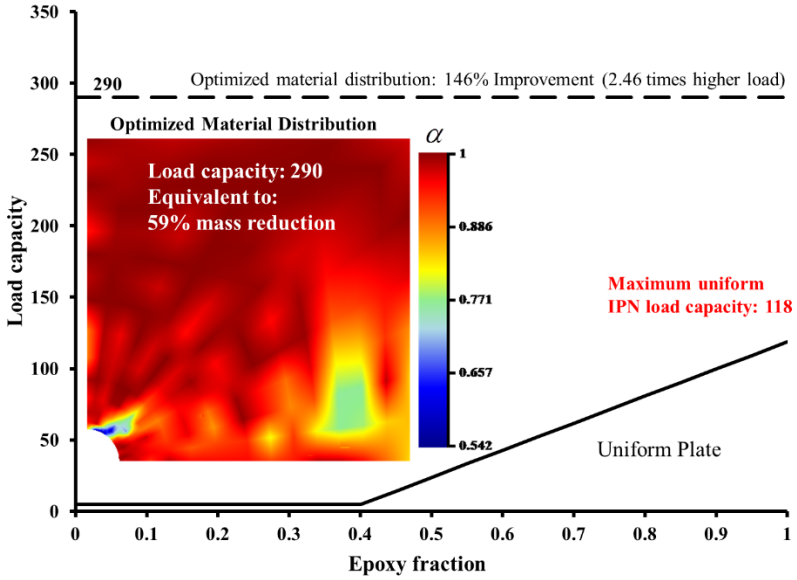

Figure 6.9 Load capacity for uniform IPNs as a function of epoxy content and for an optimally graded IPN (insert shows the optimal grading).

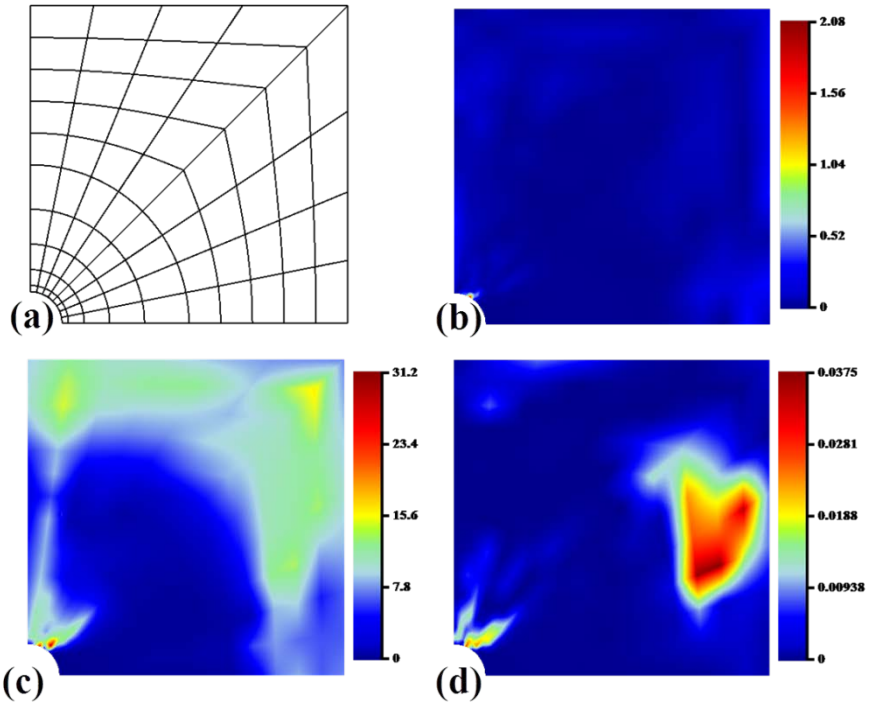

Figure 6.10 The sensitivity of the solution for the plate with a hole in tension characterized by: (a) the mesh used, (b) the first derivative, (c) the curvature, and (d) 5% offset sensitivity.

The sensitivity of the maximum load capacity to variations in the optimal grading is given in Fig. 6.11(b-d). The grading is controlled by the values of the concentration at the corner nodes of the elements shown in Fig. 6.11(a). The derivative and curvature of the normalized load capacity given in Eq. (6.14) is given in, respectively, Fig. 6.11 (b) and (c), and the sensitivity of the normalized load capacity to a 5% offset from the optimal grading is shown in Fig. 6.11(d). The slope at the optimal distribution should be zero and the variation from zero observed Fig. 6.11(b) was due to the regression using a quadratic function, not a result of less than optimal solution. The curvature given in Fig. 6.11(c) shows high sensitivity of the optimal solution to variations near the hole, which is also confirmed by the 5% offset shown in Fig. 6.11(d). Other than adjacent to the hole,

the material grading is smaller and the regions of sensitivity of the solution are exclusive of the regions with larger grading.

The printing of a complex material grading, such as shown in Fig. 6.9, can be difficult. The importance of generating the fine details of the proposed grading is evaluated Fig 6.12. Fig. 6.12(b) and Fig. 6.12(c) show, respectively, the grading and the load capacity if one rounds up to a 1, any concentrations higher than 0.9 and 0.85 (only done in the places where the sensitivity is low). As can be seen, these changes reduce the optimal load capacity from 146% improvement, to, respectively, 117% and 108% improvement, while substantially reducing the regions that need to be graded. Fig. 6.12 (d) removes all the grading, other than in the high sensitivity area next to the hole. This final change reduces the improved load capacity from 146% to 89%, still substantially better than a uniform body.

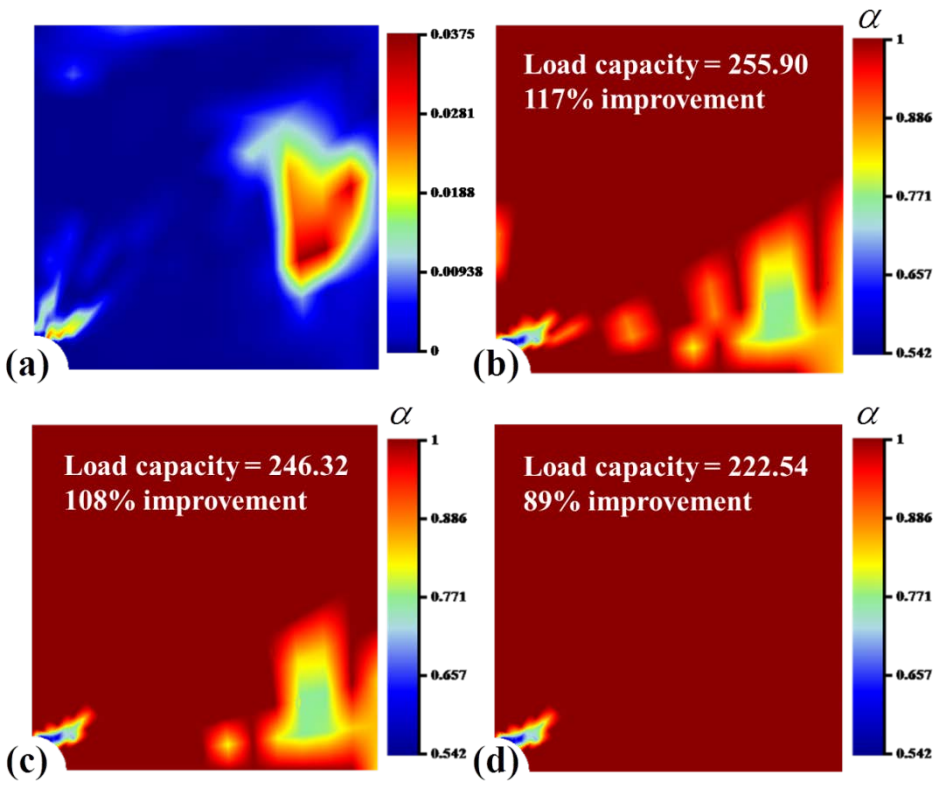

Figure 6.11 The influence of the variation in grading: (a) the 5% offset sensitivity, (b and c) the smoothing of the grading by rounding up to 1 from, respectively, 0.9 and 0.85 in regions that show low sensitivity, and (d) rounding all values to 1 in regions other than with high sensitivity next to the hole.

6.4.2 Optimal grading for an L-shaped bracket

The second example is for the optimization of the grading for an L-shaped bracket subject to a loading as described in Fig. 6.13. The bracket is studied as a plain-strain problem that is fixed on one side and subject to an applied load, as shown, on the other. As for the previous example, four-node isoparametric quadrilateral elements were used to model the material grading. The convergence of the optimizer was studied using 8x10=80 to 12x14=168 elements, each having 4x4=16 nodes per element, with little observed change in the optimized solution. The results presented are for 112 sixteen node elements.

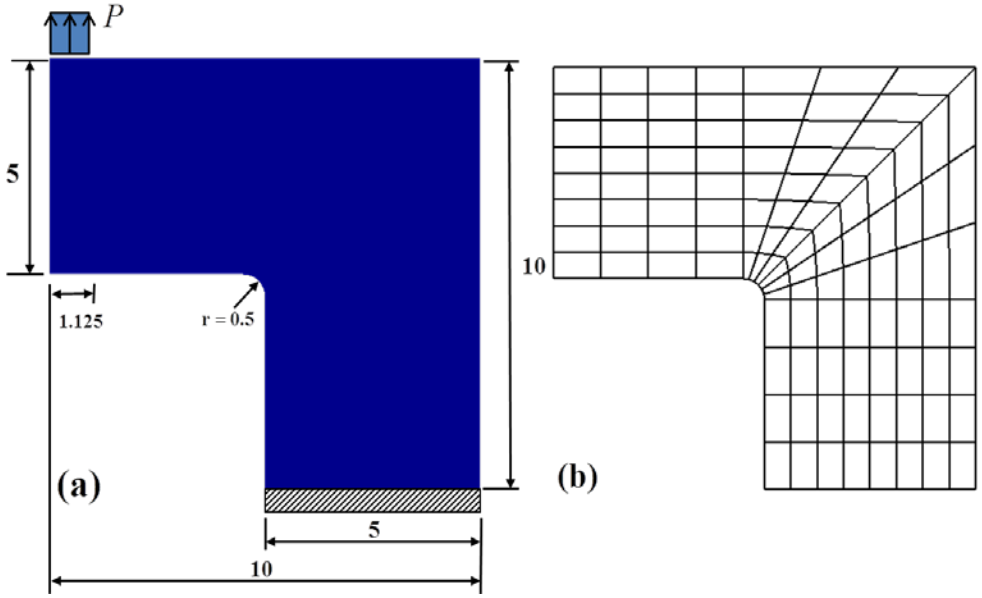

Figure 6.12 Optimization problem: (a) L-shaped bracket geometry and loading condition, (b) the mesh used.

Fig. 6.14, shows the maximum tensile stress in the uniform bracket and for the IPN. The uniform bracket solution shows the stress for the optimal uniform IPN from this system, which as shown in Fig. 6.15 is a pure epoxy bracket. As shown in Fig. 6.15, the optimal grading improves the load capacity by a factor of 2.12 over the best possible uniform system. This represents at 112% improvement, or can be considered a potential of 53% weight (thickness) reduction.

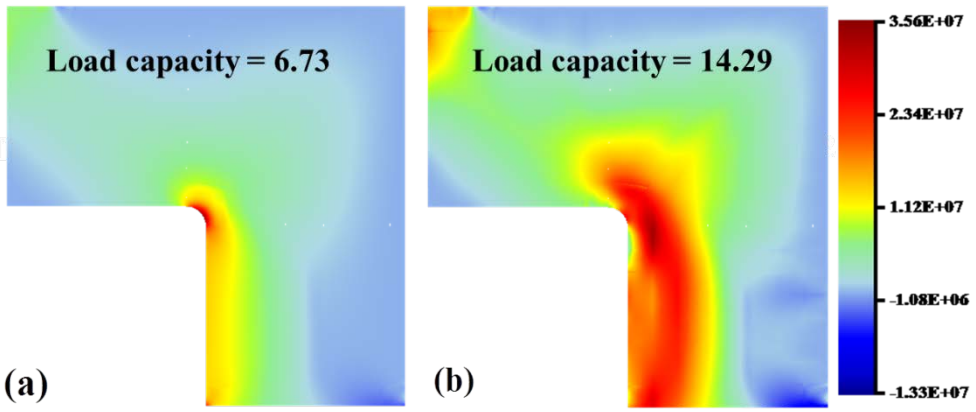

Figure 6.13 Maximum tensile stress distribution for: (a) Uniform epoxy bracket, (b) Grading Optimized bracket.

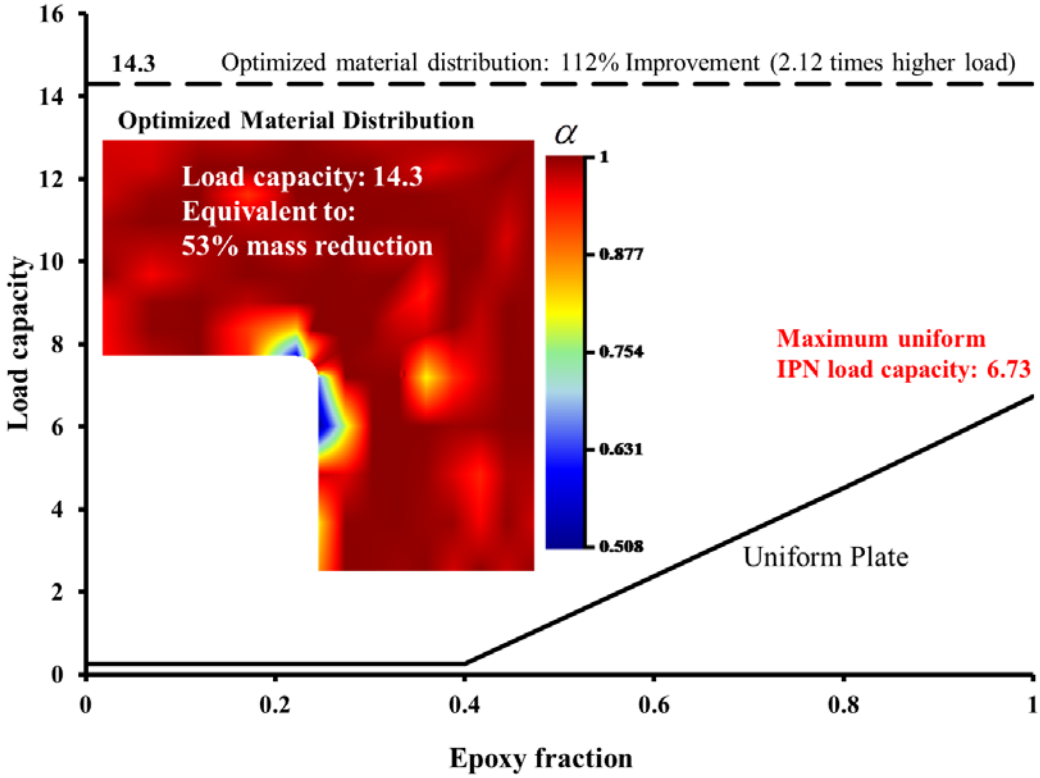

Figure 6.14 Load capacity for uniform IPNs as a function of epoxy content and for an optimized grading of IPN (insert).

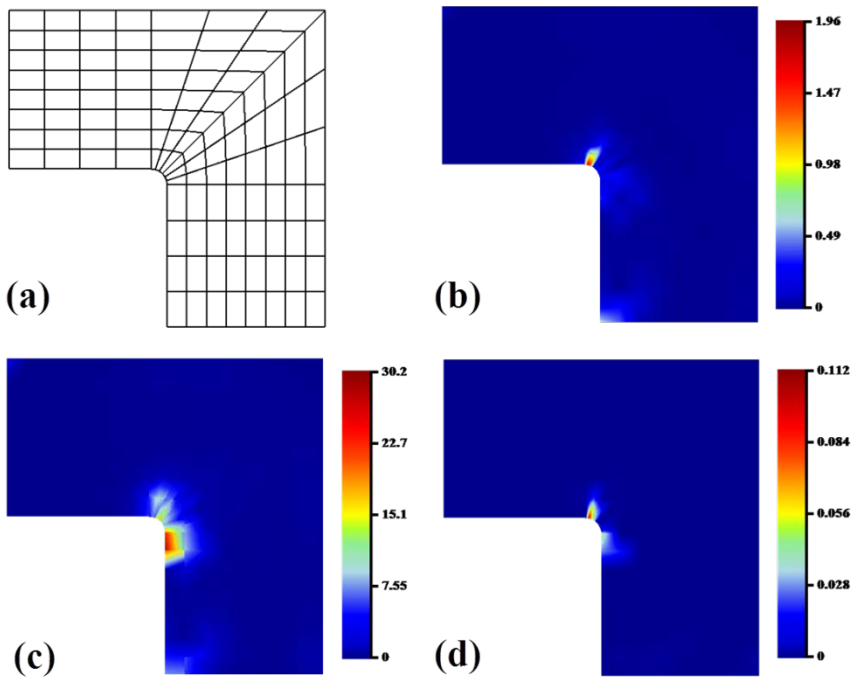

Figure 6.15 The sensitivity of the solution for the L-shaped bracket characterized by: (a) the mesh used, (b) the first derivative, (c) the curvature, and (d) 5% offset sensitivity.

Fig. 6.16 shows the sensitivity of the maximum load capacity to changes in the optimal grading as defined by the concentrations at the corner nodes shown in the mesh. As for the plate with a hole, the first derivative of the optimal solution should be zero and the deviation shown in Fig. 6.16(b) is a result of the regression process. Both the curvature and the 5% offset around the optimal solution indicate sensitivity of the solution only over a small region. This was used in Fig. 6.17 to systematically remove/reduce the regions of grading. Fig. 6.17(c) and (d) show the change in load capacity if one rounds up to 1 the concentration in regions with low sensitivity from, respectively, 0.9 and 0.85. As can be seen, a substantial reduction in the region of grading can be obtained with only 13% reduction in the improved load capacity.

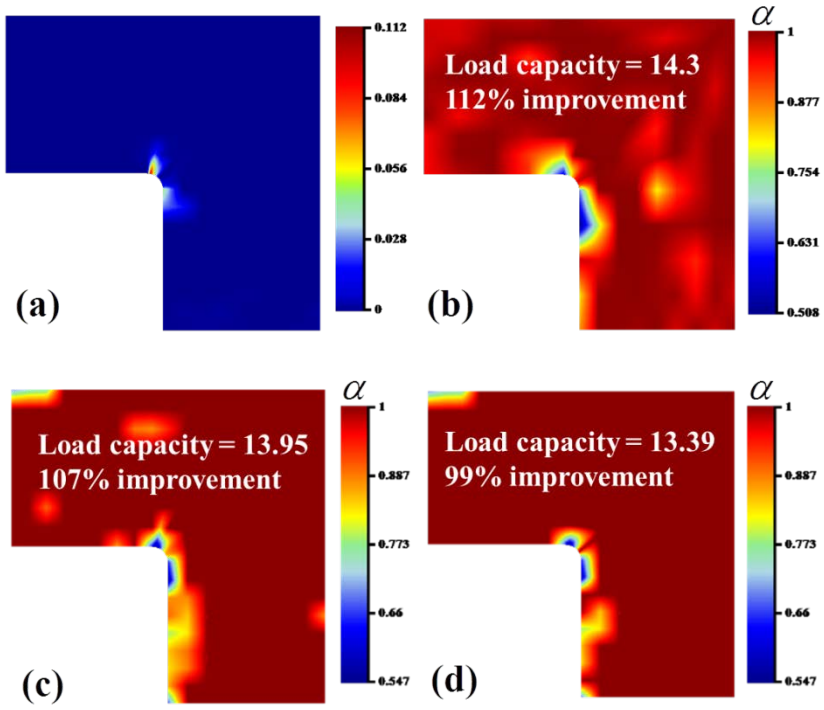

Figure 6.16 Sensitivity of optimal load capacity and its variation for L-Shaped bracket: (a) 5% offset sensitivity, (b) the optimal grading, (c and d) rounding up to 1 of concentration from, respectively, 0.9 and 0.85 in regions of low sensitivity.

6.5 Discussion

Even though we have not made an FGM part for the IPN system selected, the analysis suggests that one may create graded parts out of this system that have over a hundred percent higher load capacity, or, conversely, be over 50% lighter. The challenge is to find a way to print the needed grading so that one can get the predicted enhancements. Fortunately, unlike many other grading methods, the grading of the IPNs can be done continuously with molecular level entanglement of the building networks. This produces tough structures that are not plagued by micro- or meso-structural discrete interfaces, which inherently act as points of weakness and undermine the expected gains from the grading.

The extension of a plate with a hole and an L-shaped bracket were used as demonstrations for calculating the optimal grading for this IPN system. The graded systems both showed over 100% improvement in load capacity in comparison to the best uniform acrylate/epoxy IPN from this system. A study of the sensitivity of the load capacity of the optimal material grading to variations of the grading was conducted, which showed points of the grading that need to be accurately reproduced and places where less accuracy may be possible. A redesign of the part with homogenization of the sections with low sensitivity indicated little variation in the performance of the part. This suggests that high fidelity grading need only be focused on critical grading features.

The material system plays a central role in the effectiveness of grading in a specific problem. The behavior of an IPN system depends both on the ratio of components in the system, and also on each component's characteristics. For example, the specific acrylate/epoxy system considered varied its properties from a soft rubbery acrylate to a hard epoxy, giving the designer two orders of magnitude variation in modulus and one order in strain at failure to work with. This would not necessarily be the case with other IPNs and, thus, the optimal grading and the expected improvements would be closely connected to the IPN system considered.

Finally, even though optimization of grading has been conducted for the plate with a hole under load [93], the inclusion of a realistically varying ultimate stress is new. To the best knowledge of the authors, the potential for such a substantial change in load capacity by using functional grading with IPNs has not yet been reported.

Chapter 7 Optimal material grading in parts with single or multiple cracks

7.1 Introduction

In industrial applications, cracks often happen to working parts and this becomes a main limitation to the parts' lifetime and may even cause a disaster. Adopting FGM near the crack tip can change the part's fracture resistance and thereby potentially increases its load capacity or prolongs its lifetime. . In addition, this allows to design crack-like shapes in the body without introducing adverse effects on load carrying capacity.

Many articles have focused on the fracture behavior in calculating the mechanical responses of FGM parts. FEM computation of fracture parameters of FGM assemblages of arbitrary geometry with stationary cracks was accomplished by Kim et al. [89]. They developed graded elements where the elastic moduli are designed to be smooth functions of the spatial co-ordinates and integrated into the weak formulation to obtain the element stiffness matrix. They used these elements to calculate the stress intensity factors for mixed-mode two-dimensional problems using three different approaches, all tailored for FGMs, showing the accuracy of each of the methods. Long et al. [115] studied the plane elasticity problem of an arbitrarily oriented crack in an FGM layer bonded to a homogeneous half-plane. Fourier transform techniques were used to reduce the problem to the solution of a system of Cauchy-type singular integral equations, which were solved numerically. The results show that crack length, crack orientation and the non-

homogeneity parameter of the strip material (i.e., the grading) have significant effects on the fracture of the FGM layer. Huang et al. [116] derived asymptotic solutions for FGM thin plates with geometrically induced stress singularities. The eigenfunction expansion method was employed to solve the equilibrium equations in the vicinity of a sharp corner. The characteristic equations for determining the stress singularity order at the corner vertex and the corresponding corner functions were explicitly given for different combinations of boundary conditions. Ghajar et al. [117] used a simplified strategy based on the interaction energy integral implemented in FEM to evaluate mixed mode Stress Intensity Factors (SIFs) in 3D arbitrary non-planar cracks. The proposed approach does not require any a priori information about the crack front and it was extended to FGMs with graded Young's modulus and Poisson's ratio.

There are also a number of articles that combine optimization and fracture. Papila et al. [118] examined the minimum-weight design optimization of a composite blade-stiffened panel using a crack propagation constraint related to the stress intensity factor. A low-fidelity approach was used in a closed-form solution for evaluating the stress intensity factor, while a high-fidelity approach was used for evaluating the stress distribution around the crack. Structural optimization was used to minimize weight by low- and high-fidelity approaches for a number of panels configured with different values of the load, crack length, and blade height. Lellep et al. [119] studied inelastic conical shells loaded by a central rigid boss with a vertical load. The thickness of the conical part of the structure was taken as piecewise constant. The connection between the shell and the boss was taken to be weakened with a stable crack. Designs with maximal load-carrying capacity were established under a given amount of material consumption of the

shell. Numerical results revealed the ability of the optimized shell to withstand much higher loads in comparison to shells of constant thickness. Challis et al. [120] used the vertical crack extension technique to optimize the fracture resistance of structures . For these results, a derivative with respect to shape of the fracture-resistance was derived. The optimal structures obtained showed rounded corners with more material at places where the structure is in tension. Based on these results, they propose that fracture resistance may be modeled more easily, but less directly, by including a term proportional to surface area in the objective function. Peng et al. [121] presented a novel approach to shape optimization of three-dimensional damage-tolerant structures for improved fatigue life. A methodology and software were developed to automate damage-tolerance calculations using computer-aided design and Failure Analysis of Structures (FAST) codes. This software is used to evaluate different damage-tolerance objective functions using optimization algorithms. This work confirms, by numerical examples, that a stress-optimized structure does not necessarily give the longest fatigue life.

Not only restricted to shape or dimension, fracture mechanics analysis has also focused on material optimization. For instance, Kim [122] optimizes material properties to prevent crack propagation in a plastic small outline J-lead package with a dimpled diepad under an IR soldering process. The properties of the four parts of the structure were design variables and the J integral was the objective function. The optimized values were determined by applying a constraint optimization technique to the integrated circuit package. However, to the author’s best knowledge, material optimization in FGMs using fracture mechanics analysis has not yet been done.

In this chapter, we study the problem of designing functionally graded parts under fracture conditions for a PMMA/PU IPNs system. The system shows linear elastic response, and by changing the ratio of its components one can change the elastic modulus by a factor of three and the fracture toughness by a factor of one and one half. Due to the linearity of the elastic response before fracture, this allows defining the objective function for optimization as the ratio of the fracture strength to equivalent stress intensity factor. This method is used to demonstrate FGMs that improve the load carrying capacity by a factor of two to three, which may be interpreted also as a potential for substantial reduction in weight. This benefit comes from the competition between changes in modulus and fracture toughness at the crack tip for this IPNs system, and represents a realistic potential that may be achieved if one produces a method to manufacture the proposed grading.

The chapter starts by giving the material and associated properties for the IPNs system. These are presented in terms of the ratio of the components, which in the following section is used as the parameter for variation of functional grading. This is followed by describing the method to calculate the mixed mode stress intensity factor for FGMs and the associated fracture criterion used. A general purpose optimization code is then attached to the finite element method (FEM) solver Abaqus to obtain the optimal grading of parts. This method is used to optimize the grading of FG-IPNs parts in several examples. In each case the part with optimized grading performs substantially better, typically one hundred percent better, than any uniform part made from this IPN system.

7.2 Material model

The material model considered in this paper is for an IPNs system made from poly(methyl methacrylate) (PMMA) and polyurethane (PU). In this system, PMMA is the stiffer component and PU is the more ductile component. This system was synthesized by Bird et al. [123] and the mechanical properties evaluated in Jajam et al. [124]. The reported properties include the Young's modulus, Poisson's ratio, and fracture toughness for samples with component ratios of PMMA:PU of 100:0, 90:10, 85:15, 80:20, 75:25 and 70:30.

The Poisson's ratios were found to be about 0.35 for all samples, which is the value used for this study. The Young's modulus and fracture toughness varied with the fraction of PMMA as shown in Figure 7.1. These variations can be described as a function of the fraction α of PMMA by the relations

$$\begin{aligned} E &= 14.524\,\alpha^2 - 17.69\,\alpha + 6.3732 \ \text{GPa}, \\ K_{Ic} &= -29.524\,\alpha^2 + 50.148\,\alpha - 19.525 \ \text{MPa-m}^{1/2}. \end{aligned} \tag{7.1}$$

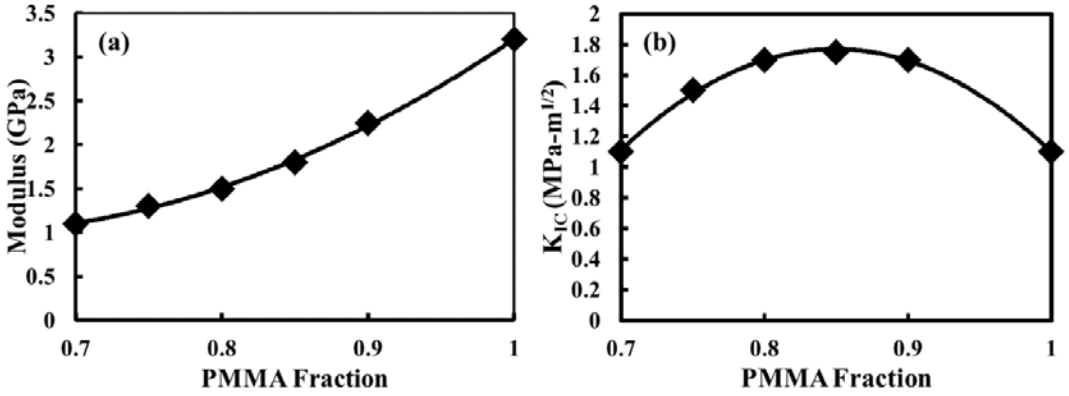

Figure 7.1 Properties of the PMMA/PU IPN as a function of PMMA fraction: (a) Young's modulus, (b) fracture toughness [124].

7.3 Stress intensity factor and fracture criterion evaluation in a graded body

The Displacement Correlation Technique proposed by Tracey [125] was used to numerically evaluate the stress intensity factors at the crack tip and the maximum hoop stress criterion, given by Erdogan and Sih [126], was taken to determine the maximum load capacity of a graded body during mixed mode fracture.

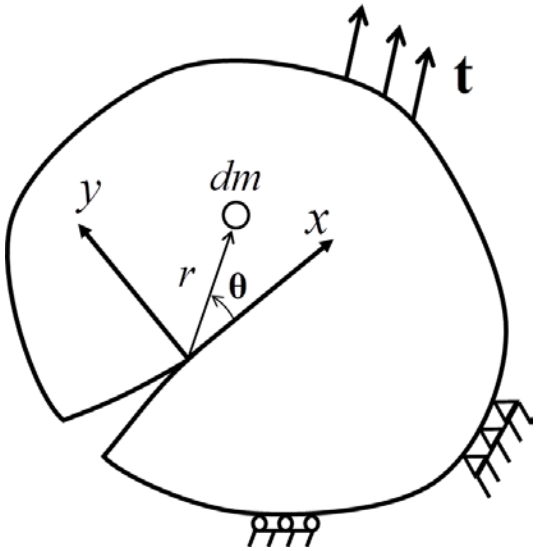

Figure 7.2. 2D nonhomogeneous elastic body with a crack.

Only two-dimensional problems were considered for the following examples. Figure 7.2 shows a crack embedded in a two-dimensional inhomogeneous elastic body under plane stress or plane strain conditions. In the following Cartesian and cylindrical coordinate systems oriented relative to the direction of the crack have been fixed at the crack tip as shown. On the figure, applied tractions and prescribed displacements on the boundary of the body are shown schematically. Body forces are neglected, and the crack faces are assumed to be traction-free. Eischen [127] has applied extension of the Wiliams eigenfunction expansion technique [128] to show that a 2D cracked FGM body has the same form of the near tip stress and displacement fields as for the case of a body with uniform material if the elastic moduli can be expressed as continuous and generally differentiable functions of the spatial coordinates. As a result, the near-tip stresses for the continuously graded material can be given in the form

$$\begin{aligned}
\sigma_{xx} &\cong \frac{K_I}{(2\pi r)^{1/2}} f_{xx}^{I}(\theta) + \frac{K_{II}}{(2\pi r)^{1/2}} f_{xx}^{II}(\theta) + \sigma_{xo} + O\left(r^{1/2}\right) + \cdots, \\
\sigma_{yy} &\cong \frac{K_I}{(2\pi r)^{1/2}} f_{yy}^{I}(\theta) + \frac{K_{II}}{(2\pi r)^{1/2}} f_{yy}^{II}(\theta) + O\left(r^{1/2}\right) + \cdots, \\
\sigma_{xy} &\cong \frac{K_I}{(2\pi r)^{1/2}} f_{xy}^{I}(\theta) + \frac{K_{II}}{(2\pi r)^{1/2}} f_{xy}^{II}(\theta) + O\left(r^{1/2}\right) + \cdots.
\end{aligned} \tag{7.2}$$

In these equations, K_I and K_{II} are the mode I and mode II stress intensity factors. σ_{xo} is named the “nonsingular stress”, which is associated with the crack kinking phenomena. The functions f_{xx}^{I}, f_{xy}^{I}, f_{yy}^{I}, etc. are trigonometric functions of the angle θ and have been derived by Eftis [129]. It should be noted that the terms $O\left(r^{1/2}\right)$ and higher do not exhibit the same spatial dependence as the corresponding terms for a homogeneous material. The integral of the strain displacement relation gives the near-tip displacement fields as

$$
\begin{aligned}
u_x &\cong \frac{K_I}{\mu_{tip}}\left(\frac{r}{2\pi}\right)^{1/2} g_x^I(\theta)+\frac{K_{II}}{\mu_{tip}}\left(\frac{r}{2\pi}\right)^{1/2} g_x^{II}(\theta)+u_{xo}+O(r)+O\left(r^{3/2}\right)+\cdots,\\
u_y &\cong \frac{K_I}{\mu_{tip}}\left(\frac{r}{2\pi}\right)^{1/2} g_y^I(\theta)+\frac{K_{II}}{\mu_{tip}}\left(\frac{r}{2\pi}\right)^{1/2} g_y^{II}(\theta)+u_{yo}+O(r)+O\left(r^{3/2}\right)+\cdots,
\end{aligned}
\tag{7.3}
$$

where μ_{tip} is the shear modulus at the tip, and u_{x0} and u_{y0} are rigid body displacements.

A widely-used method to calculate the stress intensity factor for a problem in elastic fracture mechanics is the displacement correlation technique (DCT), first devised by Tracey [125], that is based on the fact that quadratic isoparametric elements achieve $1/\sqrt{r}$ singularity by placing the mid-side node near the crack tip at the quarter points, as shown in Fig. 7.3. In this case, the stress intensity factors can be calculated from

$$
\begin{aligned}
K_I &= \sqrt{\frac{2\pi}{\Delta a}}\left[4\left(\frac{\mu}{\kappa+1}\right)_{tip} u_{2,i-1}-\left(\frac{\mu}{\kappa+1}\right)_{tip} u_{2,i-2}\right],\\
K_{II} &= \sqrt{\frac{2\pi}{\Delta a}}\left[4\left(\frac{\mu}{\kappa+1}\right)_{tip} u_{1,i-1}-\left(\frac{\mu}{\kappa+1}\right)_{tip} u_{1,i-2}\right],
\end{aligned}
\tag{7.4}
$$

where κ is a material constant equal to $3-4\nu$ for plane strain, and $(3-\nu)/(1+\nu)$ for plane-stress conditions, Δa is the characteristic length of the crack-tip element shown in the figure. The locations of the nodal displacements needed for the calculation are also shown in the figure. Among the methods to obtain stress intensity factors of nonhomogeneous bodies [127, 130], DCT has the advantages of producing sufficient accuracy and is fairly simple to implement.

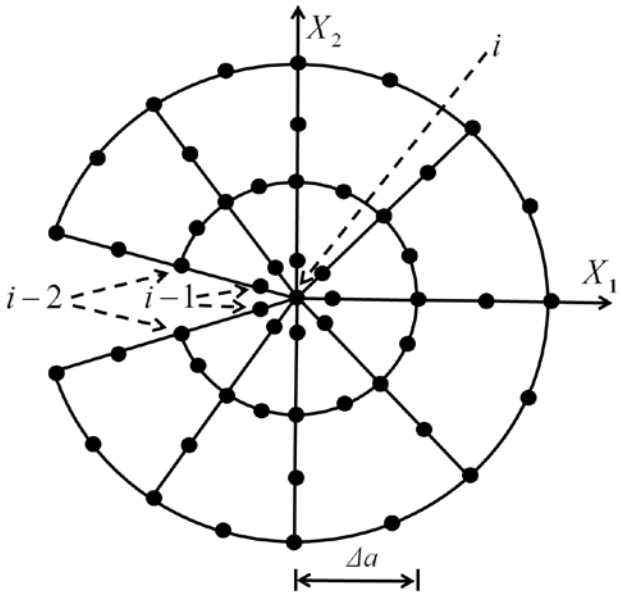

Figure 7.3 Near tip finite element nodes.

There are three well-known fracture criteria to date. These include the maximum hoop stress criterion [126], the maximum strain energy release rate [131], and the minimum strain energy density [132]. Due to the limited availability of data on the fracture toughness for the selected IPN, the maximum hoop stress criterion was selected for this study. This criterion was proposed by Erdogan and Sih [126] to capture mixed-mode fracture when only the first-mode critical fracture toughness is available. The asymptotic stresses for a crack in a linear elastic FGM is given by

$$\begin{aligned}
\sigma_{rr} &= \frac{1}{\sqrt{2\pi r}}\cos\frac{\theta}{2}\left[K_I\left(1+\sin^2\frac{\theta}{2}\right)+\frac{3}{2}K_{II}\left(\sin\theta-2\tan\frac{\theta}{2}\right)\right],\\
\sigma_{\theta\theta} &= \frac{1}{\sqrt{2\pi r}}\cos\frac{\theta}{2}\left(K_I\cos^2\frac{\theta}{2}-\frac{3}{2}K_{II}\sin\theta\right), \qquad (7.5)\\
\sigma_{r\theta} &= \frac{1}{2\sqrt{2\pi r}}\cos\frac{\theta}{2}\left[K_I\sin\theta+K_{II}\left(3\cos\theta-1\right)\right].
\end{aligned}$$

Since the near tip stress distributions for a homogeneous body and an FGM body are of the same form, it is reasonable to adopt the same fracture criteria for the FGM as for the homogenous body. The maximum hoop stress criterion assumes that the crack growth direction is along the direction with maximum hoop stress (i.e., the direction along which the shear stress $\sigma_{r\theta}$ is zero). This then provides the crack initiation angle θ_o from the condition

$$\frac{\partial \sigma_{\theta\theta}}{\partial \theta} = 0 \text{ and } \frac{\partial^2 \sigma_{\theta\theta}}{\partial \theta^2} < 0. \tag{7.6}$$

Substitution of Eq. (7.5) into Eq. (7.6) yields the relation

$$\cos\frac{\theta_0}{2}\left[K_I \sin\theta_0 + K_{II}\left(3\cos\theta_0 - 1\right)\right] = 0. \tag{7.7}$$

This was combined by Erdogan and Sih [126] with the hypothesis of the maximum stress criterion by [133] to obtain the maximum hoop stress as

$$\sqrt{2\pi r}\sigma_{\theta\theta} = \cos\frac{\theta_0}{2}\left[K_I \cos^2\frac{\theta_0}{2} - \frac{3}{2}K_{II}\sin\theta_0\right], \tag{7.8}$$

where the unknown value at failure is fit to K_{Ic} for pure mode-I failure (i.e., by setting both K_{II} and θ_0 equal to zero) to obtain the failure criterion

$$\cos\frac{\theta_0}{2}\left[K_I\cos^2\frac{\theta_0}{2}-\frac{3}{2}K_{II}\sin\theta_0\right]=K_{Ic}(\mathbf{X}). \tag{7.9}$$

For convenience in the following presentation, the left hand side of this equation is defined as the equivalent stress intensity factor $K_{I\_equ}(K_I,K_{II},\theta_o)$.

7.4 Optimization strategy for the grading

In the following examples we consider optimization of the grading around a crack tip using the DCT method given by Eq. (7.4) to evaluate the stress intensities and then use the maximum hoop stress failure criterion given in Eq. (7.9) to determine the load capacity for each grading of the body following a scaling process described below. The use of scaling for the linear elastic problem substantially reduces the number of steps needed for establishing the load capacity of a given grading, and thus substantially accelerates the time taken by the optimizer to find the optimal grading.

The problem considered in each case is of selection of material grading to maximize the load capacity in a body with one or more cracks. This is done by the optimization of material grading in body Ω with the boundary Γ. The grading is assumed to be fully described by giving scalar function $\alpha(\mathbf{X})$, which describes the mass fraction as a function of position $\mathbf{X}\in\Omega$. For the proposed IPNs system, this function will be taken as the mass fraction of PMMA in the system, where zero represents pure

PU and one represents pure PMMA. It is further assumed that all material properties are fully described by the value of α. For the selected system, these values are a fixed Poisson's ratio of 0.35 and Young's modulus and critical stress intensity factors given by the models described in Eq. (7.1).

Since the stress intensity factors are a linear function of the stress field in the problem, and since the stress field linearly scales for problems with scaled boundary conditions, it follows that the stress intensity factors at the crack tips also linearly scale in linear elastic problems that have scaled boundary conditions. This allows one to obtain the load capacity for each material grading of the part from one single solution for a selected reference loading. This follows from the fact that once one has the stress field for a reference loading, one can then calculate all the stress intensity factors, and then can incrementally scale these factors, without obtaining any further solutions, until the first crack tip becomes critical. Applying the scaling factor obtained in this manner to the reference boundary conditions provides the boundary conditions at which the first crack becomes critical, thus providing the load capacity. In problems for which the loading can be described by a sequence of scaled boundary conditions, this allows one to transform the problem of finding the optimal grading that yields the largest load capacity into the problem of finding the optimal grading that yield the largest allowable scaling factor for selected reference boundary conditions. This allows a single solution to be used per material grading to calculate the load capacity. In this case, for the failure criteria described by Eq. (7.9), the optimization of grading of a part with a single crack tip can be written as a minimization problem for the objective function Φ given as

$$\Phi = -\beta = -\frac{K_{Ic}\left[\alpha(\mathbf{X}_c)\right]}{K_{I\_equ}\left[\alpha(\mathbf{X}); \forall \mathbf{X} \in \Omega\right]}. \tag{7.10}$$

In this objective function, K_{Ic} is the critical stress intensity at the crack tip $\mathbf{X}_c$, and K_{I_equ} is the equivalent stress intensity factor at the crack tip. Both K_{Ic} and K_{I_equ} are calculated for the body with a given material grading $\alpha(\mathbf{X})$, and K_{I_equ} is calculated for the body subject to the selected constant reference boundary conditions. For the problem with multiple crack tips, one can calculate the scaling factor to make each crack critical and then select the minimum of these to obtain the objective function. The optimization of the grading was also done using Dlib [112], which is introduced in Chapter 6.

To provide sufficient flexibility in the grading process, the grading in the following demonstrations were introduced by a separate material grading mesh, which was different from the FEM mesh. The variation of properties, the grading, was then controlled by the optimizer by changing the nodal values of α on this material mesh. These nodal concentrations were each denoted as α_i. The array of nodal concentrations, denoted by $\boldsymbol{\alpha}$, were then varied by the optimizer to find the optimal grading. As in finite elements, the value of the grading in each material mesh element was interpolated from the nodal values. In addition, this method of defining the grading allowed the finite element solution mesh to be different from the material grading mesh, which as described below will be selected to be of lower order to avoid known problems and to bound the concentration between zero and one.

As described in Chapter 5 and also in papers by Matsui and Terada [111] and Chen and Negahban [91], meshes that use higher order interpolation for material properties can produce regions of negative modulus values in an element, even when all the nodal moduli are positive. This has been shown to dramatically affect the quality of the graded FEM simulation. To avoid this in the higher order elements, one needs to control the relation between the values of the nodal moduli [91]. Since we would like to use general purpose optimization codes, it is undesirable to do this. A simple solution is to use a close to liner interpolation for the material, which avoids the problem. To achieve this, the material mesh uses either three-node linear triangular elements or four-node bilinear quadrilateral elements.

The optimization procedure is illustrated in the diagram shown in Fig. 7.4. The solution started by selecting the initial IPN grading near the crack tip(s), which was usually selected as uniform. This is transferred to the FEM solver (Abaqus) to calculate the displacement field for the given grading and for the selected reference boundary conditions. The displacements calculated are used to evaluate the stress intensity factors at the crack tip(s), and then the critical scaling factor is evaluated to find the objective function for the optimization step. The objective function is then given to the optimizer, which evaluates the conditions and either changed the grading, in which case the new grading is returned to FEM solver to initiate the next evaluation step, or terminated the process and records the optimal grading.

The general purpose FEM solver Abaqus was used to calculate the stress field. As shown in Fig. 7.4, the optimizer selects the material grading by selecting the nodal

concentration on the material mesh. This grading is then transferred to Abaqus through a user defined material subroutine (UMAT). The UMAT evaluates the material properties at the integration points in the FEM solution by using interpolation of nodal values in the material mesh. The separation of the FEM mesh from the material grading mesh not only solves the problem of potential negative moduli in higher order elements, but also allows the restriction of the grading process to a small region of the body around the crack. This smaller region of grading allows the use of fewer nodal concentrations by the optimizer, a fact that substantially decreases the computational time needed to optimize the grading.

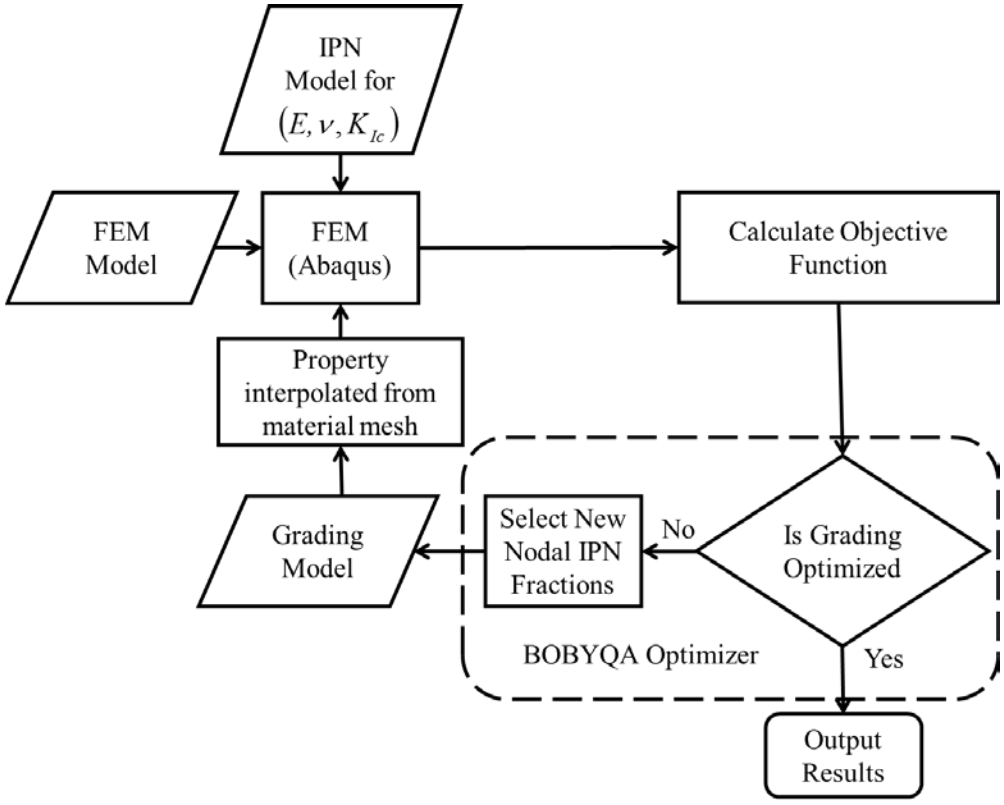

Figure 7.4 Optimization procedure.

7.5 Demonstrated examples

The following shows the potential improvement in load capacity of plates in tension by using FG-IPNs. The demonstrations include a plate with: (a) an orthogonal edge crack, (b) a slanted edge crack, (c) a slanted interior crack, and (d) interacting slanted edge cracks. In each case, the extent of improvement obtained by functional grading is given in terms of the percent improvement relative to the maximum load capacity that can be achieved using any uniform IPN of this PMMA/PU system. Thus, the reported improvements are a result of the grading and are truly beyond the possible improvements without grading.

For simplification of the problem and to reduce the number of parameters used by the optimizer, the material mesh describing the grading only covered a circular area surrounding the crack tip(s). The balance of the body was taken to be a uniform PMMA/PU system. The material mesh typically included 36-55 nodes at which the optimizer could specify the fraction of PMMA in the IPNs system. In the graded area, the material properties at the FEM integration points were interpolated from the nodal properties in the material mesh. To avoid insensitivity of the FEM solution process to changes in the PMMA fractions at the material mesh nodes, the material mesh elements were taken about twice as large as the FEM elements. To evaluate the sensitivity of the optimal load capacity to the size of the graded region, the problem was solved for several different region sizes. No significant change in the optimized capacity was observed for the four demonstrations. In addition, to insure convergence of the FEM solution, for a given material mesh, the FEM element size was reduced to make sure of the convergence of the load capacity calculated from the FEM solution. For all the solutions, the

optimization was done using the beginning trust region of 0.1 and final trust region of 0.01 for the PMMA fraction. Thus, the expected uncertainty in optimal grading is about one percent.

Plate in tension with a perpendicular edge crack: This problem was first proposed and solved analytically by Erdogan and Wu [134]. The problem considered here has a width of $W = 1$ and a crack length of $a = 0.4$ and is shown in Fig. 7.5(a). For the FEM solution, only half of the plate was modeled due to the symmetry of the problem. The FEM mesh used for calculating the displacement is shown in Fig. 7.5(b). The region for which the grading was optimized is indicated in Fig. 7.5(c). The FEM solution used a mesh with 1402 nodes and 1340 plane strain elements. The evaluation of the stress intensity factors using the DCT procedure from the Abaqus generated FEM solution was verified to be no more that 5% by comparison to the known analytic solution for an exponentially changing modulus [134]. The material mesh used for controlling the variation in material properties used 6 nodes along the radius and 7 nodes along the half circle, resulting in 36 nodes. The optimizer varied the concentration at these nodes to get the grading that produced the maximum load capacity.

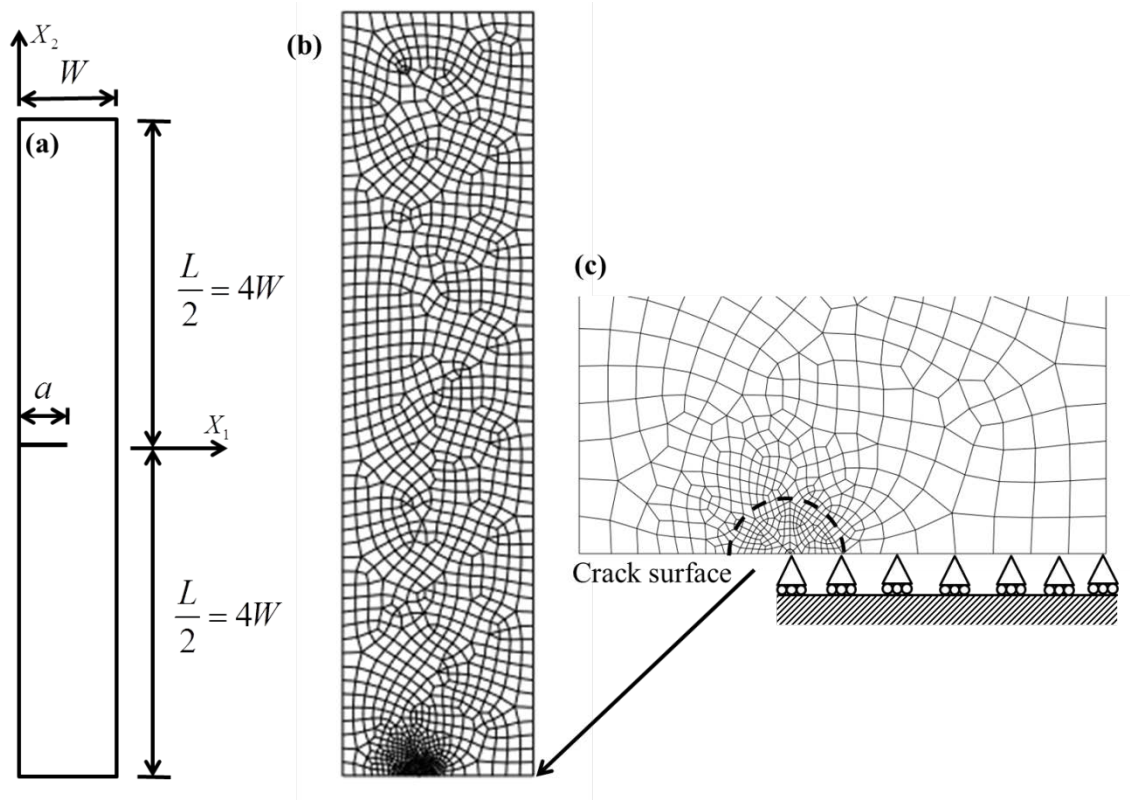

Figure 7.5. The plate with an edge crack under tension: (a) problem geometry, (b) FEM mesh made for top half, and (c) near-tip circular region in which the grading was varied.

Plate in tension with a slanted edge crack: Fig. 7.6(a) shows the problem considered. For the calculations, a length $L = 2$, width $W = 1$, crack length $a = 0.4\sqrt{2}$, and crack angle of 45^o to the horizontal direction were selected. The FEM mesh is shown in Fig. 7.6(b), and its magnification is shown in Fig. 7.6(c). The FEM mesh contained 508 nodes and 459 plane stress elements. The stress intensity factors obtained using the DCT method from the FEM solutions using the general purpose solver Abaqus were validated against Eischen's solution [127] for exponentially changing modulus. The material mesh controlling the material property distribution had 5 nodes along the radius and 9 nodes around the circumference, resulting in 37 total nodes on which the fraction of PMMA could be varied by the optimizer.

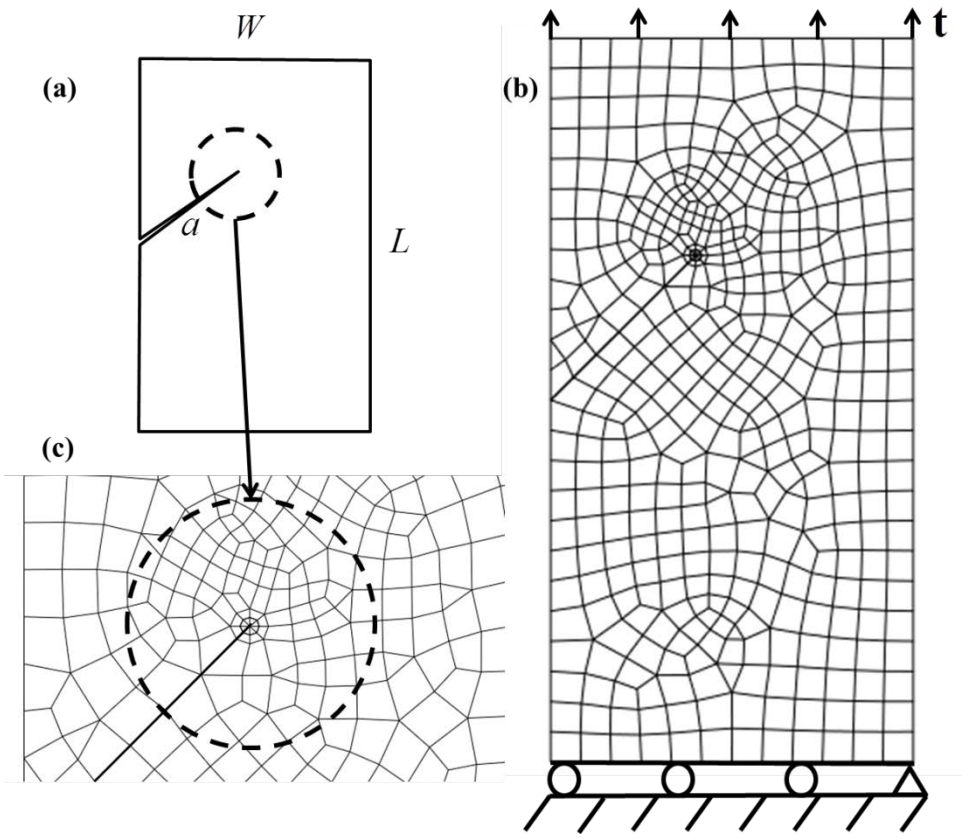

Figure 7.6 Plate with a slanted edge crack in tension: (a) geometry, (b) FEM mesh and boundary conditions, (c) near-tip mesh and the area used for grading optimization.

A plate in tension with a slanted interior crack: An inclined interior crack of length 2*a* was centered in the sample and rotated from 0^o to 72^o relative to the horizontal as shown in Fig. 7.7(a) for a plate under a vertical tensile load. The dimensions were selected as *W* = *L* = 10 and half crack length was taken as *a* = 1. The FEM mesh for the case of $\theta = 18^o$ is shown in Fig. 7.7(b), on which the area graded around the two crack tips is also shown. The number of elements used to conduct the FEM solution with Abaqus varied for the different θ, but the DCT method for calculating the stress intensity factors for each case were validated using Konda and Erdogan's solution [135] assuming the modulus and the

traction change exponentially. The material mesh controlling the material property distribution had 5 nodes along the radius and 9 nodes around the circumference, leading to 37 variables in the optimization. The same grading was assumed at each crack tip due to the symmetry of the problem. The node and element numbers used in the FEM solution are given for the different crack inclinations θ in Table 1.

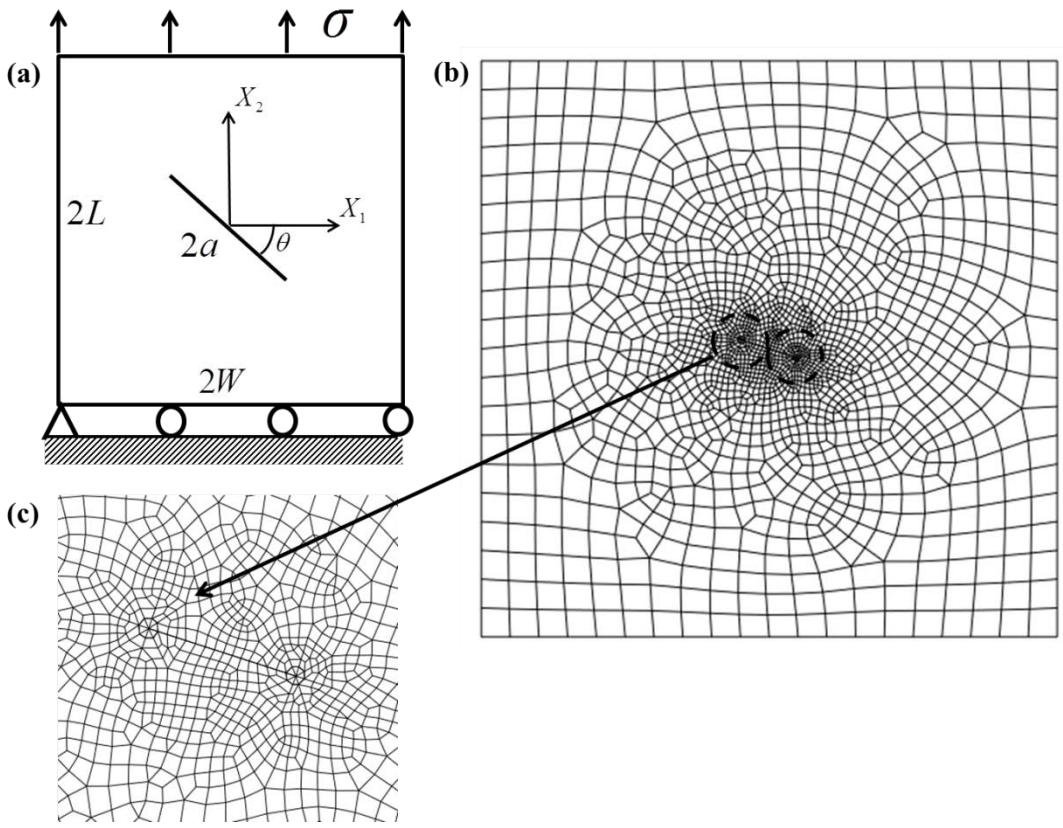

Figure 7.7. An interior slanted crack in a plate in tension: (a) geometry and boundary conditions, (b) FEM mesh, (c) expanded view of mesh around crack.

Table 7.1. Number of FEM nodes and element used for the slanted internal crack demonstration.

θ	0^o	18^o	36^o	54^o	72^o
Number of nodes	2183	1769	1953	1746	1343

Number of elements	2141	1714	1903	1695	1294

Plates in tension with interacting edge cracks: Fig. 7.8 shows the two cases of interacting edge cracks considered. The first, shown in Fig. 7.8(a), is for two orthogonal cracks, while the second, shown in Fig. 7.8(b), is for two 45^o inclined cracks. In each case $W = 2$ and the crack length was selected to result in the crack tips reaching the centerline of the plate. Fig. 7.8(c) and Fig. 7.8(d) show the FEM mesh around the crack tips and the circular region of material grading. The material mesh controlling the material property distribution used 5 nodes along radius and 9 nodes around the circumference, leading to 37 optimization variables. Only one material grid was employed due to the point symmetry of the problem. For the orthogonal cracks, the number of FEM nodes and elements used were, respectively, 2105 and 1983, while for the inclined cracks they were, respectively, 1796 and 1671.

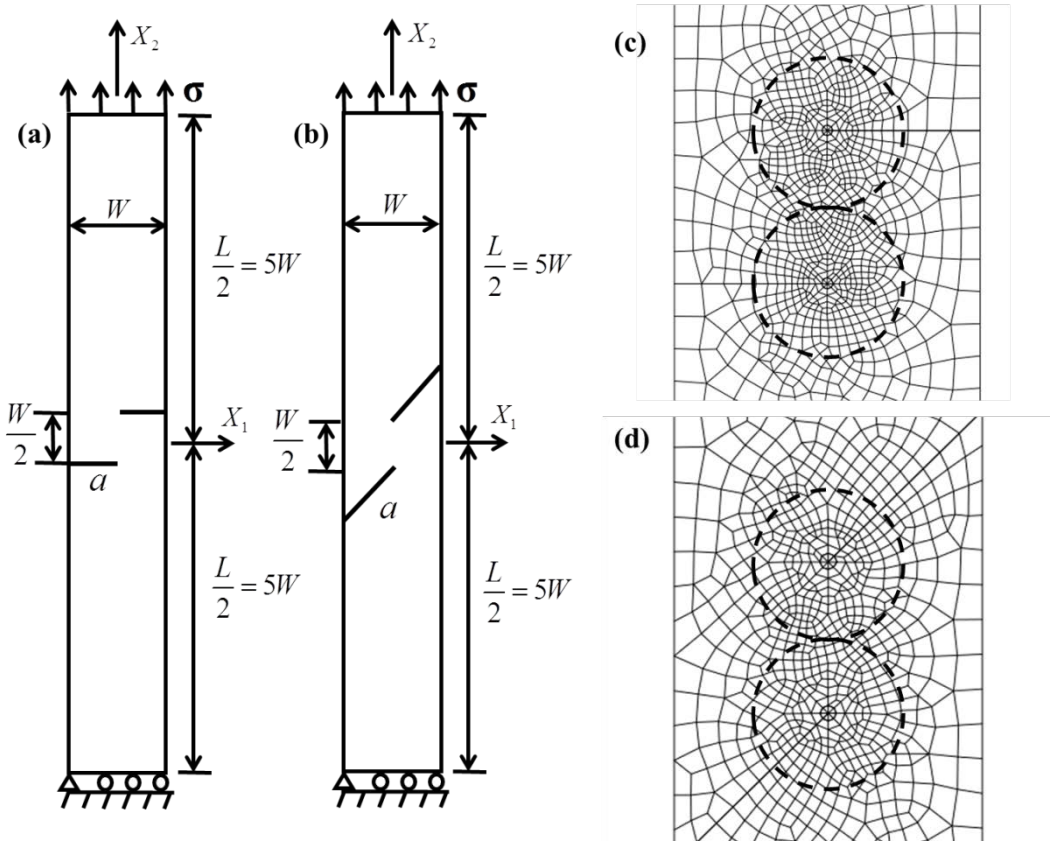

Figure 7.8. Plates in tension with interacting edge cracks: (a) orthogonal interacting cracks, (b) inclined interacting cracks, (c) near tip mesh for orthogonal cracks and area graded, (d) near tip mesh for slanted cracks and area graded.

7.6 Discussion

For each example, the specific results of optimizing the grading around the tip are shown below. The optimized load capacity in all cases were compared to the best load capacity possible using a uniform mixture of the selected PMMA/PU system. As expected, and shown in Table 7.2, the highest load capacity for a uniform PMMA/PU IPN system occurs for each example at $\alpha = 0.85$ when the fraction of PMMA corresponds to the case of maximum critical stress intensity factor K_{Ic}. Yet, as also shown in Table 7.2, this capacity can always be increased by functional grading of a

region around the crack. As can be seen, this improvement in capacity is typically more than one hundred percent, and sometimes is as high as 200%.

Table 7.2. Comparison of the improvement in load capacity for the FG-IPN compared to the uniform IPN.

Problem	**Edge crack**		**Internal slanted crack (angle)**					**Interacting Cracks**	
	0°	45°	0°	18°	36°	54°	72°	0°	45°
PMMA Fraction	**Load Capacity for Uniform PMMA/PU IPN**								
0.70	0.52	0.67	1.14	1.06	1.16	1.53	2.95	0.42	0.49
0.75	0.66	0.89	1.51	1.41	1.54	2.03	3.92	0.56	0.60
0.80	0.79	1.02	1.74	1.62	1.77	2.33	4.50	0.64	0.69
0.85	**0.83**	**1.06**	**1.81**	**1.69**	**1.84**	**2.43**	**4.69**	**0.67**	**0.71**
0.90	0.73	1.02	1.73	1.62	1.76	2.32	4.49	0.64	0.68
0.95	0.69	0.88	1.51	1.41	1.53	2.02	3.90	0.55	0.59
1.00	0.52	0.67	1.13	1.05	1.14	1.51	2.91	0.42	0.44
Functionally Grading PMMA/PU IPN Around Crack Tip									
Capacity	**1.69**	**2.09**	**3.78**	**3.50**	**3.91**	**5.57**	**14.41**	**1.13**	**1.26**
Improvement	**104%**	**97%**	**108%**	**107%**	**113%**	**129%**	**207%**	**69%**	**77%**
Tip Fraction	0.795	0.800	0.796	0.797	0.805	0.811	0.819	0.799	0.807

The improvement of load capacity is controlled not only by the functional grading around the crack tip, but also by the characteristics of the uniform material outside this region. Table 7.3 shows the optimal load capacity after functional grading around the tip for different selections of uniform PMMA/PU outside this zone. As can be seen, the highest load capacity is achieved when outside the area of grading one uses pure PMMA. This is expected since PMMA is the more rigid component of the PMMA/PU IPN system and thus pure PMMA functions on the outside of the graded region to maximally limit the deformation imposed on the crack. Thus, the part with a graded region around the crack and pure PMMA outside this region takes advantage of both the rigidity of pure

PMMA outside the zone around the crack and the functional grading inside the zone around the crack tip to achieve the maximum load capacity. Yet, as seen in the table, the optimization suggests a grading at the crack tip of about $\alpha = 0.8$, which is slightly below the fraction for the highest K_{Ic}. Since the DCT method using the Abaqus FEM solution showed up to 5% variation in the calculated K_I and K_{II} compared to the published analytical values, the solution suggests that the optimization pushed the grading at the crack tip toward the fraction of PMMA/PU with the highest K_{Ic}. This clearly indicates that away from the crack tip higher rigidity of the material, indicated by a higher modulus, is preferred, while at the tip higher toughness, indicated by higher K_{Ic}, is desirable. The details of the specific functional grading for each example follow

Table 7.3 Influence of the fraction of PMMA outside the graded region on the maximum load capacity of the FG-IPN.

Problem	**Edge crack**		**Internal slanted crack (angle)**					**Interacting Cracks**	
PMMA Fraction (Outside Grading)	0°	45°	0°	18°	36°	54°	72°	0°	45°
	Load Capacity for Functionally Grading PMMA/PU IPN Around Crack Tip								
0.70	1.056	1.446	2.361	2.287	2.511	3.44	9.123	0.913	1.054
0.75	1.124	1.516	2.489	2.399	2.643	3.635	9.732	0.94	1.08
0.80	1.212	1.606	2.665	2.55	2.822	3.89	10.5	0.975	1.112
0.85	1.317	1.712	2.884	2.74	3.042	4.205	11.38	1.013	1.149
0.90	1.433	1.829	3.144	2.961	3.298	4.56	12.338	1.053	1.186
0.95	1.559	1.955	3.442	3.214	3.59	4.961	13.354	1.093	1.224
1.00	**1.692**	**2.087**	**3.778**	**3.5**	**3.91**	**5.57**	**14.417**	**1.132**	**1.261**
Maximum Load Capacity Configuration									
Load Capacity	**1.69**	**2.09**	**3.78**	**3.50**	**3.91**	**5.57**	**14.41**	**1.13**	**1.26**
Outside Fraction	1.00	1.00	1.00	1.00	1.00	1.00	1.00	1.00	1.00
Tip Fraction	0.795	0.800	0.796	0.797	0.805	0.811	0.819	0.799	0.807

Plate in tension with a perpendicular edge crack: As shown in Table 7.2, one obtains the maximum load capacity of 0.83 for the uniform concentration of 85% PMMA, which can be increased to 1.69 by functional grading. This 104% improvement was achieved by using a pure PMMA outside the circular zone of grading, and grading it as shown in Fig. 7.9, which also shows the maximum principal stress for the uniform and functionally graded cases. As can be seen, the optimization put higher PU content behind the crack tip, higher PMMA material ahead of the crack tip, and approximately the highest toughness material at the crack tip. As can be seen from the principal stresses, the grading redistributes the stress. This, in effect, reduces the intensity of the singularity at the crack tip and thus allows the plate to carry about twice the load.

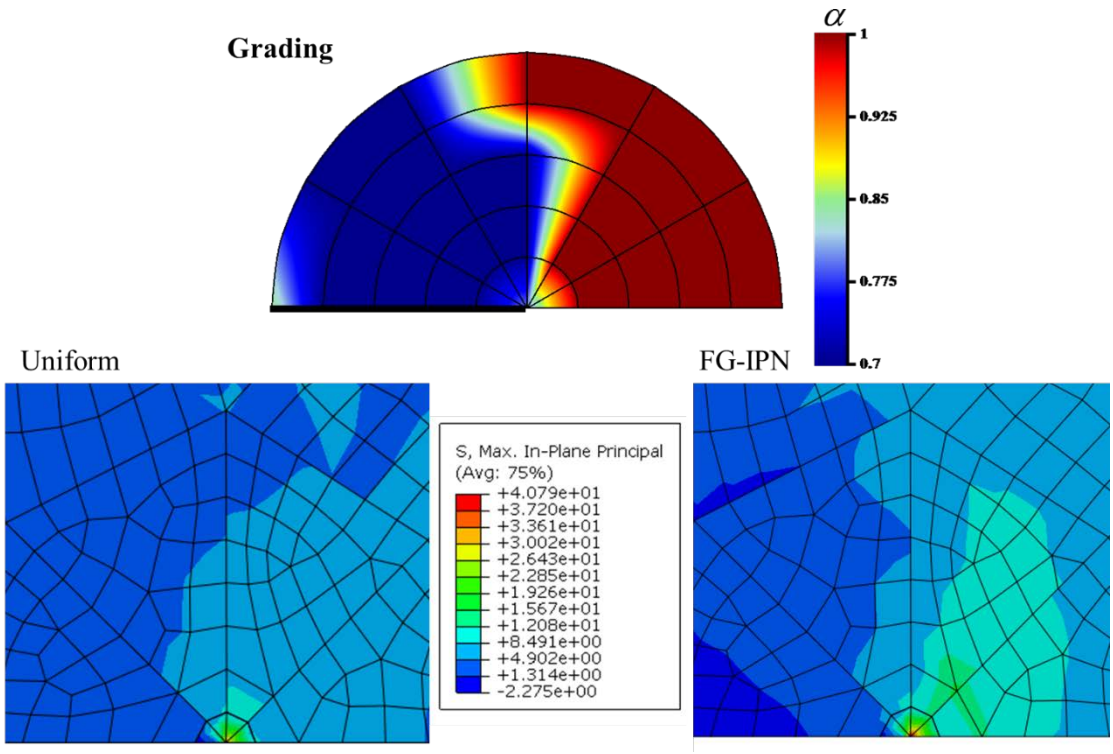

Figure 7.9 The plate with an edge crack under tension: Optimized material distribution (top), maximum principal stress before optimization (bottom left) and after optimization (bottom right).

Plate in tension with a slanted edge crack: For uniform plates made from the PMMA/PU system, the maximum load capacity was calculated as 1.06 for a uniform PMMA fraction of 85%. After optimizing the grading around the crack tip, this load capacity increased to 2.09, indicating 97% improvement by functional grading. The optimized grading is displayed in Fig. 7.10. As can be seen, again the optimizer recommends increasing the PU content behind the crack tip and increasing PMMA content ahead of the crack tip, while putting the toughest material at the crack tip. The maximum principal stress at fracture before and after optimization of grading, also shown in Fig. 7.10, indicates that the grading redistributes the stress allowing more of the

material to carry higher loads. This, in effect, reduces the load on the crack tip and, thus, softens the singularity.

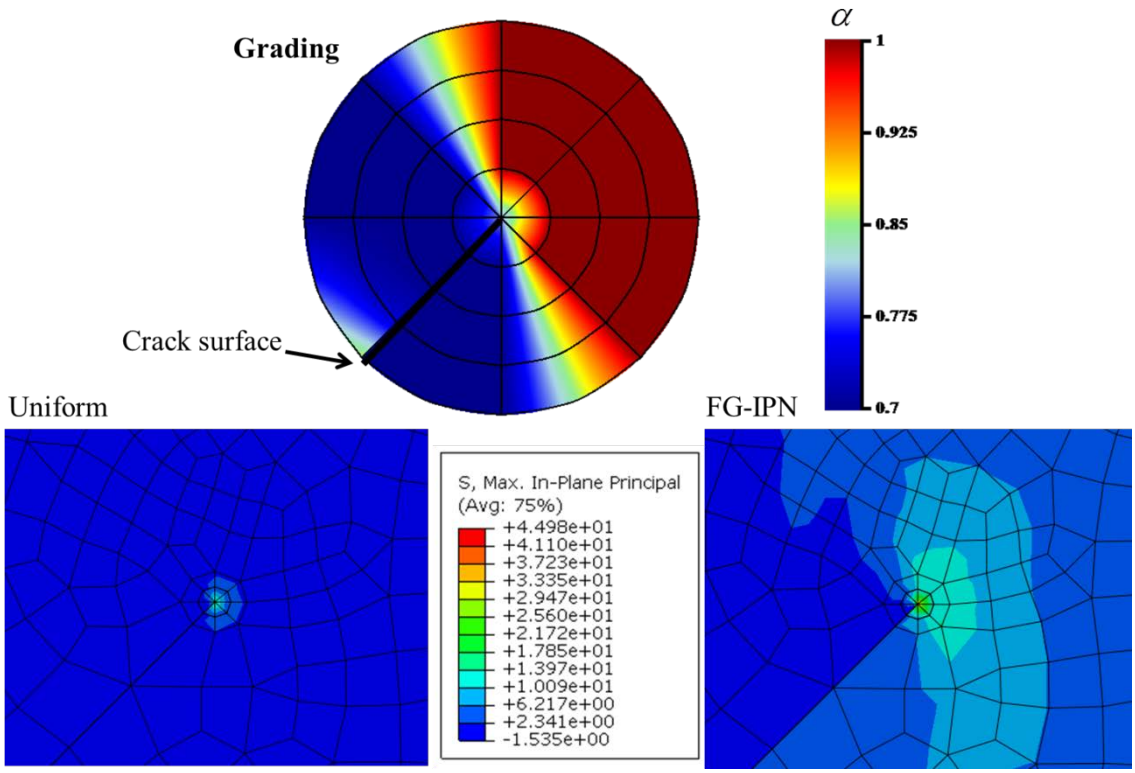

Figure 7.10 Plate with a slanted edge crack in tension: Optimized material distribution top, maximum principal stress before optimization (bottom left) and after optimization (bottom right).

A plate in tension with a slanted interior crack: In comparison to uniform plates, Table 7.2 indicates that the improvement by grading in this case is significant and varies from 108% to 207% depending on the crack inclination. It was assumed that the grading would be similar, up to a reflection, for the left and right crack tips so that only one grading is displayed in the following. For the horizontal crack, the material distribution for the left crack tip and maximum principal stress before and after grading are shown in Fig. 7.11.

For the other orientations, the optimized material distributions for the left crack tip is displayed in Fig. 7.12. As previous demonstrations showed, an increase in PU content around the crack surface helps reduce the strength of the singularity and thus increase the load capacity. With increasing orientation, K_{II} plays a more important role in the fracture model. The maximum principal stress in each case for a uniform and graded IPN plate, each calculated at the associated maximum load capacity, are shown in Fig. 7.13 and Fig. 7.14. As before, the grading reduces the strength of the singularity by increasing the load carried by other portions of the material.

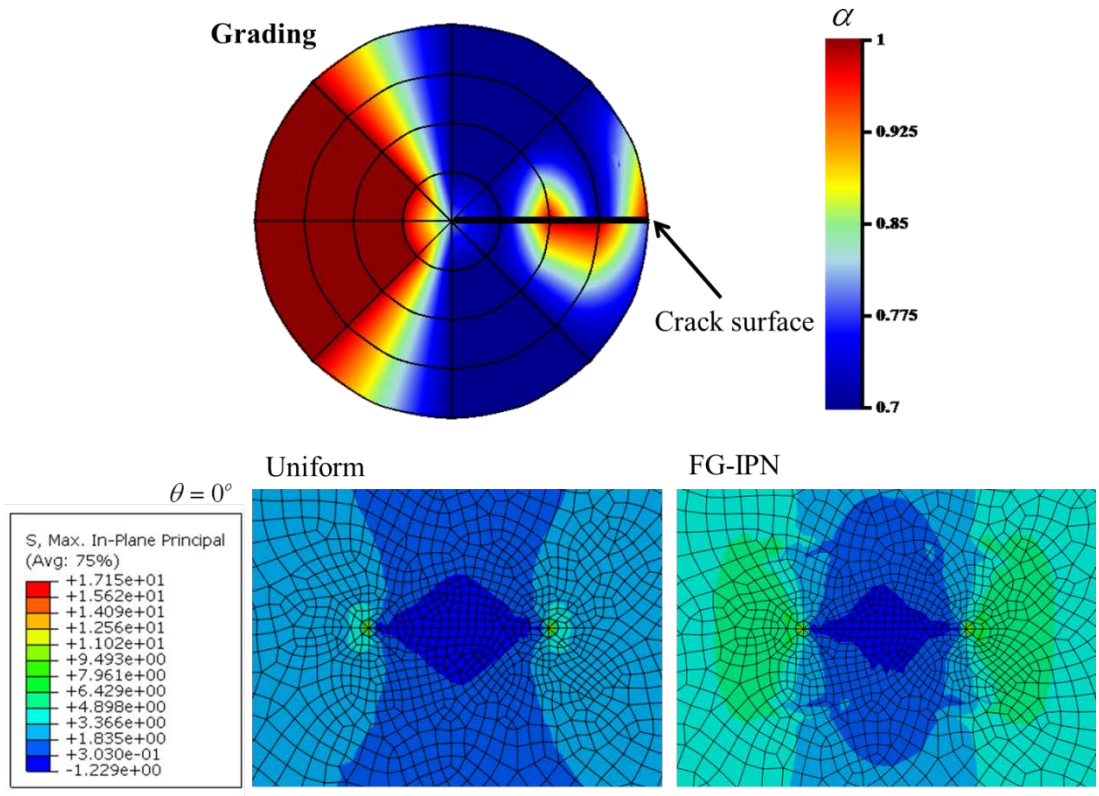

Figure 7.11 Optimized material distribution for plate with interior crack of angle 0°.

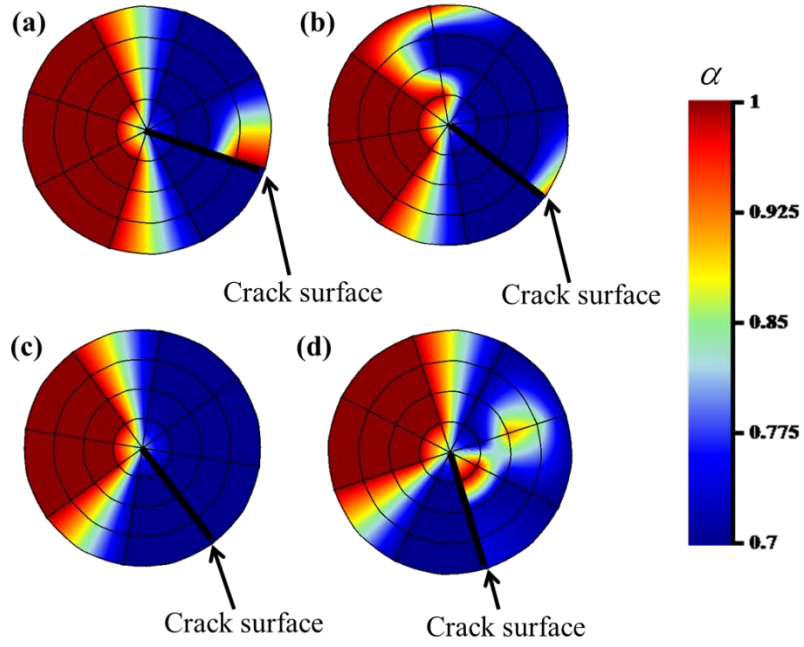

Figure 7.12 Optimized material distribution for plates with inclined interior cracks: (a) 18º, (b) 36º, (c) 54º, and (d) 72º.

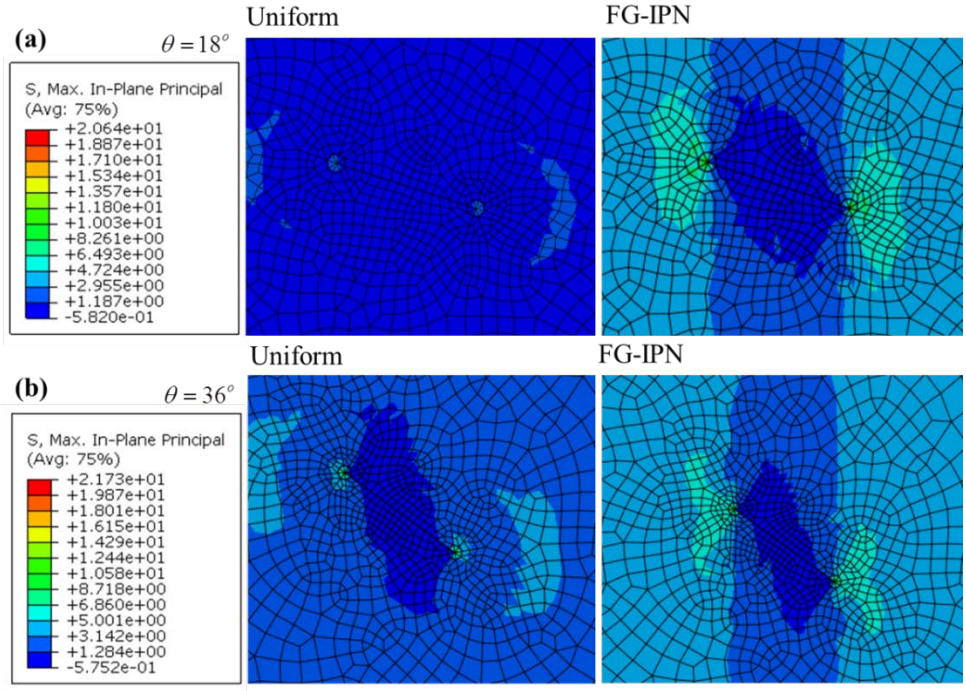

Figure 7.13 Principal stress for uniform and FG-IPN plate with inclined cracks of angle 18º and 36º.

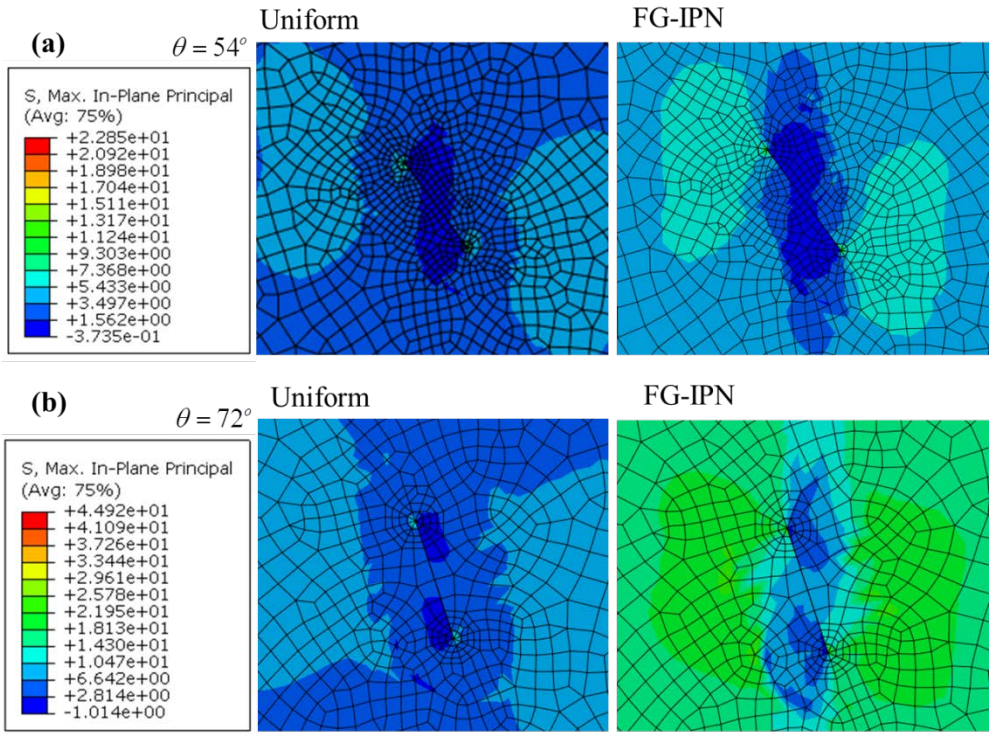

Figure 7.14 Principal stress for uniform and FG-IPN plate with inclined cracks of angle 54º and 72º.

Plates in tension with interacting edge cracks: For these cases, the interaction of two orthogonal or two inclined edge cracks were considered. It was determined that the grading improved the highest capacity obtained for a uniform plate by, respectively, 69% and 77%. The solution assumed the grading at the two crack tips to be similar up to a reflection so only one grading is shown in each case. Fig. 7.15 shows the optimal grading for the right crack and the maximum principal stress distribution before and after grading. Fig. 7.16 shows the same for the two inclined cracks.

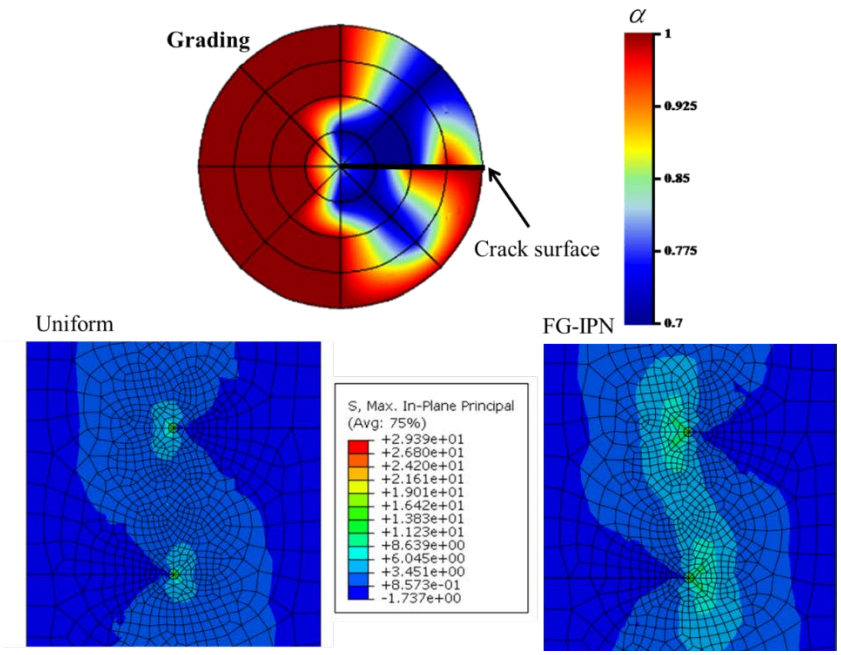

Figure 7.15 Optimal grading for two interacting orthogonal edge cracks and principal stresses before and after grading.

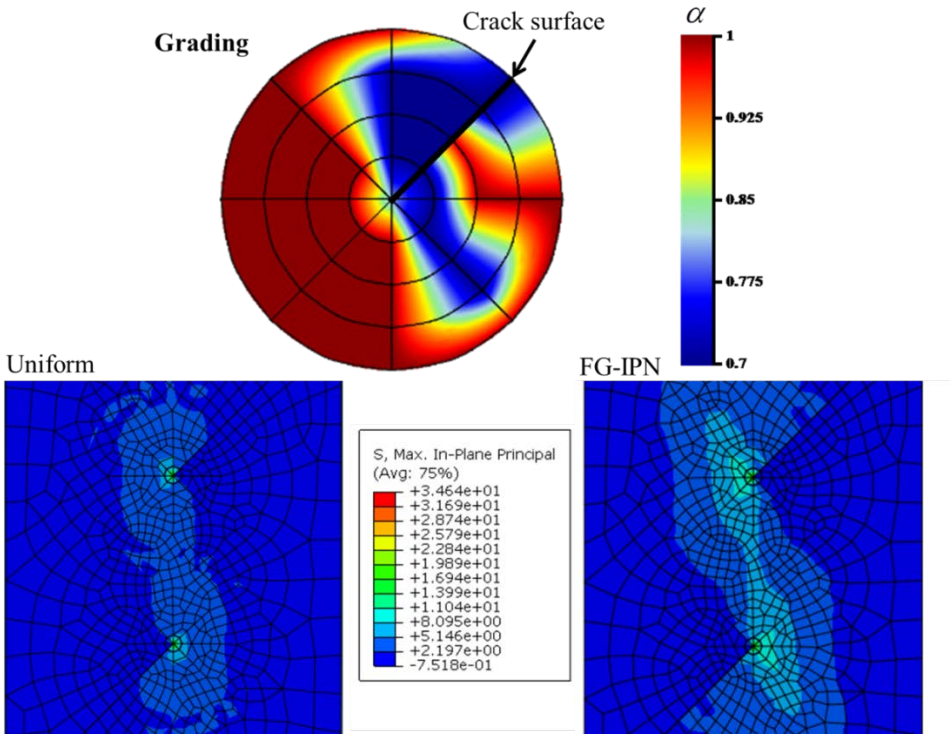

Figure 7.16 Optimal grading for two interacting inclined edge cracks and principal stresses before and after grading.

In addition to optimal grading around the crack, one might ask how other simpler design solutions might compare to the optimized grading. The improvements obtained for two such designs are shown in Table 7.4. As before, in each case the improvements are reported relative to the load capacity of the best uniform PMMA/PU system (i.e., relative to uniform 0.85 PMMA fraction). The optimal solutions suggest that high rigidity away from the crack tip helps shield the tip from excessive loading, while the high toughness at the crack tip allows it to carry higher loads before it becomes critical. Motivated by this, the first alternate solution uses the most rigid material (pure PMMA) outside the circular region around the crack tip and the toughest material (uniform 0.85 PMMA fraction) inside this region. As shown in the table, this design improves the load capacity by only 9 to 29% depending on the problem, which is substantially less than what is achieved by the optimal grading (69 to 207% improvement). The second design again takes the outside region to be pure PMMA, but linearly grades this in the circular region around the crack to the tougher 0.85 PMMA fraction at the tip. This linear grading improves the capacity relative to that of the uniform 0.85 PMMA fraction by between 18 to 32% based on the problem, yet still shows substantially less improvement compared to the optimal grading. This suggests that the more complex details of the grading play a significant role in the substantial improvements of 69 to 207% seen in the optimally graded examples.

Table 7.4. Comparison of optimally graded region near the crack tip to uniform or linearly graded regions.

Problem	Edge crack		Internal slanted crack (angle)					Interacting Cracks	
	0º	45º	0º	18º	36º	54º	72º	0º	45º
	Optimal Uniform PMMA/PU IPN (85% PMMA) Base Capacity								
Load Capacity	0.83	1.06	1.81	1.69	1.84	2.43	4.69	0.67	0.71
	Uniform 100% PMMA Outside, Uniform 85% PMMA Inside								
Load Capacity	1.04	1.27	2.34	2.18	2.36	3.10	6.05	0.73	0.77
Improvement	**26%**	**20%**	**29%**	**29%**	**28%**	**28%**	**29%**	**9%**	**9%**
	Uniform 100% PMMA Outside, Linear Grading, 85% PMMA Tip								
Load Capacity	1.09	1.33	2.39	2.21	2.37	3.09	5.91	0.80	0.84
Improvement	**31%**	**26%**	**32%**	**31%**	**29%**	**27%**	**26%**	**20%**	**18%**
	Uniform 100% PMMA Outside, Optimal Grading Inside								
Load Capacity	1.69	2.09	3.78	3.50	3.91	5.57	14.41	1.13	1.26
Improvement	**104%**	**97%**	**109%**	**107%**	**113%**	**129%**	**207%**	**69%**	**77%**

By combining the DCT method for calculating stress intensity factors from FEM solutions, development of an Abaqus UMAT subroutine to directly introduce grading into the Abaqus FEM solution, and linear scaling to reduce the number of calculations, we were able to efficiently use a bound-constrained optimization program to study the effect of functionally optimized grading around crack tips in PMMA/PU IPN parts. Using the load capacity of the part as the objective function and taking the response of the best possible uniform PMMA/PU part as the reference in each case, it was shown that by functional grading of a circular region around the tip of the crack while at the same time maximizing the rigidity of the material outside this region, one obtains optimal gradings that improve the load capacity from 69 to 207% for the edge, internal, and interacting cracks considered. Surprisingly, replacing the optimized grading of the circular region around the crack tip with either a uniform tough PMMA/PU IPN or linearly grading the outside of the region to the toughest PMMA/PU ratio at the crack tip produced a

substantially lower improvement (between 9 and 31% as opposed to the optimal improvement that was between 69 and 207%). This suggests that simply toughening the material at the tip and/or simply linearly grading it is not as significantly advantageous as optimally grading this region. Even though slightly different in each case, the optimal grading qualitatively suggests using high rigidity material ahead of the crack tip, which is cushioned by high toughness material at the crack tip and softer material behind the tip.

Chapter 8 Conclusion and future work

8.1 Summary conclusion

This dissertation is on the potential application of IPNs for substantially improving FGM parts made with optimally designed variations of the IPNs' mixture.

The presentation starts by introducing FG-IPNs, including their definition, properties, classifications, applications and modelling methods. Then the modelling methods for grading used in FEM are closely investigated.

One widely used method is to assign properties to the nodes in the FEM model and to include their FEM-based interpolation in the integrations of the weak form over the body to get a modified stiffness matrix. However, even if all nodal values are positive, there is still a chance that the interpolated values change sign and become negative in some regions of the element. This issue was studied in the context of 3-node elements and it was shown that there can be substantial deterioration in the solution quality when these regions appear in the element. In this case the ranges of parameters that produce these regions in the element were evaluated and their effect was established by providing tables of expected solution quality.

As specific examples of how FG-IPNs can substantially improve the effectiveness of a part, the problem of material optimization for parts with stress concentration and with cracks is studied under different conditions. Compositional fractions of FG-IPNs, which control the IPNs' elastic modulus and failure, are graded by optimally assigning the composition to the control nodes of using an optimization routine. This grading was

assigned to nodes in the entire part or to a select region, such as around a crack. Significant improvement, over one hundred percent in load capacity, was observed after optimization of the grading.

The method to get the optimum grading can depend on the IPN system used and the loading conditions. Fortunately, the systems considered here showed close to linear elastic response up to failure under quasi-static loading. This was used to justify using linear scaling as a simplifying step for calculating the ultimate load. This substantially accelerated the solution process, allowing us to obtain the optimal grading for a realistic number of nodal concentrations. Other IPN systems may show much more complex response, including nonlinear elastic, plastic, viscoelastic, and viscoplastic characteristics. In such cases, a more complex incremental process of loading may need to be used to capture the objective function.

Stereolithography using IPNs is one method to construct graded parts in 3D printing and these improvements load capacity suggest the possibility to use graded IPNs to substantially improve the load capacity of some polymer components. This study shows the potential of graded IPNs in building vastly improved parts with stress concentration or cracks and also is a marker for the importance of finding methods to manufacture spatial variations of properties, such as by graded 3D printing [8]. On-demand manufacturing of continuous grading, such as proposed in [9, 11, 12], can create a new paradigm for designing substantially better, much more functional or vastly lighter, parts.

8.2 Future work

The focus of my research has been on optimization of material grading using theories of solid mechanics and methods of computation. This field has produced many excellent results and is quite promising due to the astonishing progress in computational facilities and the possibility of using 3D-printing techniques to print optimized grading designs. My immediate interest is in finding materials with potential in making optimized grading and applications that promise substantial improvement. In addition to the grading made possible by interpenetrating polymer networks, other material systems can provide a method for controlled grading. These methods to grade include the introduction of grading in powder sintering, grading by thermally induced phase transformations, and grading by nano-fiber distribution, among others. The possible applications include optimizing load capacity, fracture and fatigue, controlling load transmission, load damping, and the design of metamaterials. My current work shows that the methods developed for full optimization through nodal property control in FEM promise much better grading and functionality than have been proposed up to now. I intend to use these and new methodologies to extend the effectiveness of material grading in engineering applications. Several topics that I am considering are:

Grading for fatigue life optimization: Material distribution of a part with a crack can be optimized to prolong its fatigue life. Paris' law can be employed in each material grading distribution to evaluate the number of cycles to initiate the crack propagation. Optimization of grading is expected to allow parts to sustain more cycles of loading.

Grading optimization in multi-scale strategies: Material properties in a multi-scale strategy are obtained at the mesoscopic scale from representative volume elements and passed to the macroscopic scale to calculate response and evaluate the objective function, for instance, load capacity. A potential strategy for meso-structure design can be to allow optimization of the grading in the volume element.

Multi-physics problems in material design: There are also a number of potential problems in multi-physics that are of interest of material optimization. These include the thermo-elastic coupled problems in, for example, compliance minimization under certain force and temperature boundary conditions, or electric-elastic coupled problems in, for example, electrical energy maximization of a piezoelectric beam under constant loading, or chemical-elastic-coupled problems in, for example, fatigue life maximization considering chemical corrosion.

Grading optimization for meso-structured metamaterials for stress wave propagation: Development of a systematic plan to look at structure position, dimension and material optimization for metamaterials deserves more research. This extends the classic discrete material design to that of a heavy metal imbedded in a graded acrylate/epoxy matrix. The goal would be to study the attenuation of stress wave at different frequencies. For example, a two-step optimization can be used: first optimize size and position of the repeated units and then to use optimal grading to further improve the response of the system. The stress attenuation effect of the combined optimization steps is expected to be improved significantly.

Nonlinear and viscoelastic modeling of metamaterials: To date, nearly all research on metamaterials adopted the linear elastic material model, which may not be quite accurate to simulate materials such as epoxy or rubber. I plan to introduce viscoelasticity into metamaterial modelling. I already have developed a user-defined subroutine UMAT in Abaqus describing viscoelastic constitutive relation in the Prony series formulation, which allows me to introduce grading of viscoelastic properties in Abaqus. I want to use this capability to study stress attenuation in viscoelastic metamaterials for designs that include material damping.

Combined shape and material optimization: I have an interest in extending my research in material optimization to shape and topology optimization. For instance, I am interested in topology optimization steps combined with material optimization to investigate the combined effect.

Parallel computing for material design: An area of current growth and opportunity is parallel computing and big data. Many computational models and methods can simulate the physical world quite well but need tremendous CPU time. Rapid development of supercomputers makes the solutions of such problems promising. I am looking at adapting materials design algorithms for parallel computing.

Bibliography

1. Miserez, A., T. Schneberk, C.J. Sun, F.W. Zok, and J.H. Waite, *The transition from stiff to compliant materials in squid beaks.* Science, 2008. **319**(5871): p. 1816-1819.
2. Suresh, S., *Graded Materials for Resistance to Contact Deformation and Damage.* Science, 2001. **292**(5526): p. 2447-2451.
3. Claussen, K.U., T. Scheibel, H.-W. Schmidt, and R. Giesa, *Polymer Gradient Materials: Can Nature Teach Us New Tricks?* Macromolecular Materials and Engineering, 2012. **297**(10): p. 938-957.
4. Sokolowski, J. and J.-P. Zolesio, *Introduction to shape optimization*. 1992: Springer.
5. Suzuki, K. and N. Kikuchi, *A homogenization method for shape and topology optimization.* Computer methods in applied mechanics and engineering, 1991. **93**(3): p. 291-318.
6. Rozvany, G.I., M. Zhou, and T. Birker, *Generalized shape optimization without homogenization.* Structural optimization, 1992. **4**(3-4): p. 250-252.
7. Haftka, R.T. and R.V. Grandhi, *Structural shape optimization—a survey.* Computer methods in applied mechanics and engineering, 1986. **57**(1): p. 91-106.
8. Bartlett, N.W., M.T. Tolley, J.T. Overvelde, J.C. Weaver, B. Mosadegh, K. Bertoldi, G.M. Whitesides, and R.J. Wood, *A 3D-printed, functionally graded soft robot powered by combustion.* Science, 2015. **349**(6244): p. 161-165.
9. Shin, K.-H., H. Natu, D. Dutta, and J. Mazumder, *A method for the design and fabrication of heterogeneous objects.* Materials & Design, 2003. **24**(5): p. 339-353.
10. Shah, K., I.u. Haq, A. Khan, S.A. Shah, M. Khan, and A.J. Pinkerton, *Parametric study of development of Inconel-steel functionally graded materials by laser direct metal deposition.* Materials & Design (1980-2015), 2014. **54**: p. 531-538.
11. Mahamood, R.M. and E.T. Akinlabi, *Laser metal deposition of functionally graded Ti6Al4V/TiC.* Materials & Design, 2015. **84**: p. 402-410.
12. Carvalho, O., M. Buciumeanu, G. Miranda, S. Madeira, and F.S. Silva, *Development of a method to produce FGMs by controlling the reinforcement distribution.* Materials & Design, 2016. **92**: p. 233-239.
13. Li, W., M. Bakhtiary Noodeh, N. Delpouve, J.M. Saiter, L. Tan, and M. Negahban, *Printing Continuously Graded Interpenetrating Polymer Networks of Acrylate/Epoxy by Manipulating Cationic Network Formation during Stereolithography.* Express Polymer Letters, 2016. **(in press)**.

14. Mahmud, A.S., Y. Liu, and T. Nam, *Design of functionally graded NiTi by heat treatment.* Physica Scripta, 2007. **2007**(T129): p. 222.
15. Qu, D., Z. Zhou, J. Tan, and J. Aktaa, *Characterization of W/Fe functionally graded materials manufactured by resistance sintering under ultra-high pressure.* Fusion Engineering and Design, 2015. **91**: p. 21-24.
16. Tokita, M. *Development of large-size ceramic/metal bulk FGM fabricated by spark plasma sintering*. in *Materials Science Forum*. 1999. Trans Tech Publ.
17. Tang, X., H. Zhang, D. Du, D. Qu, C. Hu, R. Xie, and Y. Feng, *Fabrication of W–Cu functionally graded material by spark plasma sintering method.* International Journal of Refractory Metals and Hard Materials, 2014. **42**: p. 193-199.
18. Sperling, L.H., *Interpenetrating Polymer Networks*, in *Encyclopedia of Polymer Science and Technology*. 2002, John Wiley & Sons, Inc.
19. Kim, S.C. and L.H. Sperling, *IPNs around the world : science and engineering*. 1997, Chichester; New York: John Wiley.
20. Touhsaent, R.E., D.A. Thomas, and L.H. Sperling, *Epoxy/acrylic simultaneous interpenetrating networks.* Journal of Polymer Science: Polymer Symposia, 1974. **46**(1): p. 175-190.
21. L. H. Sperling, R.H., *Interpenetrating Polymer Networks*, in *Polymer Blends Handbook*, C.A.W. L.A. Utracki, Editor. 2014, Springer Science. p. 677-724.
22. Gupta, N. and A.K. Srivastava, *Interpenetrating polymer networks: A review on synthesis and properties.* Polymer International, 1994. **35**(2): p. 109-118.
23. Frisch, K.C., D. Klempner, and H.L. Frisch, *Recent advances in polymer alloys and IPN technology.* Materials & Design, 1983. **4**(4): p. 821-827.
24. Frisch, K.C., D. Klempner, and H.L. Frisch, *Recent advances in polymer alloys and IPN technology.* Materials & Design, 1983. **4**(5): p. 855-862.
25. Schwahn, E.S., *Using Controlled Curing in a Custom Stereolithography-based 3D Printing Machine to Obtain Graded Property Variations.* 2015.
26. Karabanova, L.V., S.V. Mikhalovsky, and A.W. Lloyd, *Gradient semi-interpenetrating polymer networks based on polyurethane and poly(2-hydroxyethyl methacrylate) for biomedical applications.* Journal of Materials Chemistry, 2012. **22**(16): p. 7919-7928.
27. Mallikarjuna, B., K.M. Rao, K. Pallavi, K.C. Rao, and M.C.S. Subha, *Biodegradable interpenetrating polymer network hydrogel membranes for controlled release of anticancer drug.* Asian Journal of Pharmaceutics, 2015. **9**(2): p. 129-136.

28. Esen, H., C.C. Barghorn, and X. Allonas, *Light induced gradient refractive index materials.* Polymers for Advanced Technologies, 2016. **27**(1): p. 66-72.
29. M, N., K. A, W. R, and D.O.I. Y, *Fabrication of a high pressure thrust chamber by the CIP forming method*, in *20th Joint Propulsion Conference*. 1984, American Institute of Aeronautics and Astronautics.
30. Almasi, D., M. Sadeghi, W.J. Lau, F. Roozbahani, and N. Iqbal, *Functionally graded polymeric materials: A brif review of current fabrication methods and introduction of a novel fabrication method.* Materials Science and Engineering: C, 2016. **64**: p. 102-107.
31. Bruck, H.A. and B.H. Rabin, *Evaluation of Rule-of-Mixtures Predictions of Thermal Expansion in Powder-Processed Ni–Al2O3 Composites.* Journal of the American Ceramic Society, 1999. **82**(10): p. 2927-2930.
32. Kawasaki, A., H. Hirose, H. Hashimoto, and R. Watanabe, *Fabrication of Sintered Functionally Gradient Material by Powder Spray Forming Process.* Journal of the Japan Society of Powder and Powder Metallurgy, 1990. **37**(7): p. 922-928.
33. Miller, D.P., J.J. Lannutti, and R.N. Yancey, *Functionally Gradient Nial/Al2O3 Structures*, in *Proceedings of the 16th Annual Conference on Composites and Advanced Ceramic Materials: Ceramic Engineering and Science Proceedings*. 2008, John Wiley & Sons, Inc. p. 365-373.
34. Khor, K.A., Z.L. Dong, and Y.W. Gu, *Plasma sprayed functionally graded thermal barrier coatings.* Materials Letters, 1999. **38**(6): p. 437-444.
35. Mortensen, A. and S. Suresh, *Functionally graded metals and metal-ceramic composites: Part 1 Processing.* International Materials Reviews, 1995. **40**(6): p. 239-265.
36. KATOH, #160, M., OKAMOTO, #160, K., HORITA, #160, H., IGARASHI, #160, and T., *Re/W/Mo and Ir/W/Ta graded-structure emitters of thermionic energy converter*. Vol. 308-311. 1999, Stafa-Zurich, SUISSE: Trans Tech. XXII, 1068 p.
37. Neubrand, A., R. Jedamzik, and J. Rödel, *Functionally graded materials by electrochemical modification of porous preforms*. 1997, Elsevier Science.
38. Watanabe, Y., S.H. Kang, J.W. Chan, and J.J.W. Morris, *Fabrication of Magnetically Graded Material by Rolling Deformation of Wedge-shaped 304 Stainless Steel.* Materials Transactions, JIM, 1999. **40**(9): p. 961-966.
39. Yang, S.-C. and R.M. German, *Gravitational limit of particle volume fraction in liquid-phase sintering.* Metallurgical Transactions A, 1991. **22**(3): p. 786-791.
40. Jayakumar, E., J.C. Jacob, T.P.D. Rajan, M.A. Joseph, and B.C. Pai, *Processing and Characterization of Functionally Graded Aluminum (A319)—SiCp Metallic Composites*

by Centrifugal Casting Technique. Metallurgical and Materials Transactions A, 2016. **47**(8): p. 4306-4315.

41. Yakovlev, A., E. Trunova, D. Grevey, M. Pilloz, and I. Smurov, *Laser-assisted direct manufacturing of functionally graded 3D objects.* Surface and Coatings Technology, 2005. **190**(1): p. 15-24.
42. Hao, L., M.M. Savalani, Y. Zhang, K.E. Tanner, and R.A. Harris, *Selective laser sintering of hydroxyapatite reinforced polyethylene composites for bioactive implants and tissue scaffold development.* Proc Inst Mech Eng H, 2006. **220**(4): p. 521-31.
43. Leu, M.C., L. Tang, B. Deuser, R.G. Landers, G.E. Hilmas, S. Zhang, and J. Watts. *Freeze-form extrusion fabrication of composite structures*. in *Proceedings of the Solid Freeform Fabrication Symposium. Austin, TX*. 2011.
44. Shumiya, H., K. Kato, and H. Okubo. *Fabrication and prediction techniques for FGM (functionally graded materials) application to solid insulators*. in *CEIDP '05. 2005 Annual Report Conference on Electrical Insulation and Dielectric Phenomena, 2005.* 2005.
45. Mouchon, E. and P. Colomban, *Microwave absorbent: preparation, mechanical properties and r.f.-microwave conductivity of SiC (and/or mullite) fibre reinforced Nasicon matrix composites.* Journal of Materials Science, 1996. **31**(2): p. 323-334.
46. Miyamoto, Y., W.A. Kaysser, B.H. Rabin, A. Kawasaki, and R.G. Ford, *Applications*, in *Functionally Graded Materials: Design, Processing and Applications*, Y. Miyamoto, et al., Editors. 1999, Springer US: Boston, MA. p. 247-313.
47. Gasik, M., L. Heikinheimo, and M. Siren, *Al2O3 to Ni-superalloy Diffusion bonded FG-joints for High Temperature Applications*. 1997. p. 313-318.
48. Shi, Y., H. Yao, and Y.-w. Gao, *A functionally graded composite cantilever to harvest energy from magnetic field.* Journal of Alloys and Compounds, 2017. **693**: p. 989-999.
49. Aylsworth, J.W., *Plastic composition*. 1914, US Patent.
50. Amos, J.L., *The SPE international award address—1973 the development of impact polystyrene–a review*. Polymer Engineering & Science, 1974. **14**(1): p. 1-11.
51. Solt, G.S., P. British, Editor. 1955.
52. Staudinger, J.J. and H.M. Hutchinson, U.S. Patent, Editor. 1951.
53. Millar, J.R., *263. Interpenetrating polymer networks. Styrene-divinylbenzene copolymers with two and three interpenetrating networks, and their sulphonates.* Journal of the Chemical Society (Resumed), 1960(0): p. 1311-1317.

54. Dragan, E.S., *Design and applications of interpenetrating polymer network hydrogels. A review.* Chemical Engineering Journal, 2014. **243**: p. 572-590.

55. Signori, F., R. Solaro, E. Chiellini, P.A.M. Lips, P.J. Dijkstra, and J. Feijen, *Multifunctional polyesters as new candidate materials for biomedical applications. Synthesis and structural characterization.* Macromolecular Symposia, 2003. **197**(1): p. 289-302.

56. Twaites, B., C. de las Heras Alarcon, and C. Alexander, *Synthetic polymers as drugs and therapeutics.* Journal of Materials Chemistry, 2005. **15**(4): p. 441-455.

57. Graham, N.B. and M.E. McNeill, *Biointeractions '84 Materials/Interactions-Conference Hydrogels for controlled drug delivery.* Biomaterials, 1984. **5**(1): p. 27-36.

58. Mandal, B.B., S. Kapoor, and S.C. Kundu, *Silk fibroin/polyacrylamide semi-interpenetrating network hydrogels for controlled drug release.* Biomaterials, 2009. **30**(14): p. 2826-2836.

59. Silan, C., A. Akcali, M.T. Otkun, N. Ozbey, S. Butun, O. Ozay, and N. Sahiner, *Novel hydrogel particles and their IPN films as drug delivery systems with antibacterial properties.* Colloids and Surfaces B: Biointerfaces, 2012. **89**: p. 248-253.

60. Gallego Ferrer, G., J.M. Soria Meliá, J. Hernández Canales, J.M. Meseguer Dueñas, F. Romero Colomer, M. Monleón Pradas, J.L. Gómez Ribelles, P. Pissis, and G. Polizos, *Poly(2-hydroxyethyl acrylate) hydrogel confined in a hydrophobous porous matrix.* Colloid and Polymer Science, 2005. **283**(6): p. 681-690.

61. Liu, Y. and M.B. Chan-Park, *Hydrogel based on interpenetrating polymer networks of dextran and gelatin for vascular tissue engineering.* Biomaterials, 2009. **30**(2): p. 196-207.

62. Liu, W., C. Deng, C.R. McLaughlin, P. Fagerholm, N.S. Lagali, B. Heyne, J.C. Scaiano, M.A. Watsky, Y. Kato, R. Munger, N. Shinozaki, F. Li, and M. Griffith, *Collagen–phosphorylcholine interpenetrating network hydrogels as corneal substitutes.* Biomaterials, 2009. **30**(8): p. 1551-1559.

63. Brigham, M.D., A. Bick, E. Lo, A. Bendali, J.A. Burdick, and A. Khademhosseini, *Mechanically robust and bioadhesive collagen and photocrosslinkable hyaluronic acid semi-interpenetrating networks.* Tissue Eng Part A, 2009. **15**(7): p. 1645-53.

64. Ho, J.E., T.A. Barber, A.S. Virdi, D.R. Sumner, and K.E. Healy, *The effect of enzymatically degradable IPN coatings on peri-implant bone formation and implant fixation.* J Biomed Mater Res A, 2007. **81**(3): p. 720-7.

65. Shikanov, A., M. Xu, T.K. Woodruff, and L.D. Shea, *Interpenetrating fibrin–alginate matrices for in vitro ovarian follicle development.* Biomaterials, 2009. **30**(29): p. 5476-5485.

66. Chirila, T.V., C.R. Hicks, P.D. Dalton, S. Vijayasekaran, X. Lou, Y. Hong, A.B. Clayton, B.W. Ziegelaar, J.H. Fitton, S. Platten, G.J. Crawford, and I.J. Constable, *Artificial cornea.* Progress in Polymer Science, 1998. **23**(3): p. 447-473.

67. Liu, L. and H. Sheardown, *Glucose permeable poly (dimethyl siloxane) poly (N-isopropyl acrylamide) interpenetrating networks as ophthalmic biomaterials.* Biomaterials, 2005. **26**(3): p. 233-244.

68. Vallittu, P.K., *Interpenetrating Polymer Networks (IPNs) in Dental Polymers and Composites.* Journal of Adhesion Science and Technology, 2009. **23**(7-8): p. 961-972.

69. Shaw, M.T. and W.J. MacKnight, *Introduction to Polymer Viscoelasticity*. 2005: Wiley.

70. Panchal, J.H., S.R. Kalidindi, and D.L. McDowell, *Key computational modeling issues in Integrated Computational Materials Engineering.* Computer-Aided Design, 2013. **45**(1): p. 4-25.

71. Birman, V. and L.W. Byrd, *Modeling and Analysis of Functionally Graded Materials and Structures.* Applied Mechanics Reviews, 2007. **60**(5): p. 195-216.

72. Gupta, A. and M. Talha, *Recent development in modeling and analysis of functionally graded materials and structures.* Progress in Aerospace Sciences, 2015. **79**: p. 1-14.

73. Charalambakis, N., *Homogenization Techniques and Micromechanics. A Survey and Perspectives.* Applied Mechanics Reviews, 2010. **63**(3): p. 030803-030803.

74. Voigt, W., *Ueber die Beziehung zwischen den beiden Elasticitätsconstanten isotroper Körper.* Annalen der Physik, 1889. **274**(12): p. 573-587.

75. Cho, K. and J. Gurland, *The law of mixtures applied to the plastic deformation of two-phase alloys of coarse microstructures.* Metallurgical Transactions A, 1988. **19**(8): p. 2027-2040.

76. Eshelby, J.D., *The Determination of the Elastic Field of an Ellipsoidal Inclusion, and Related Problems.* Proceedings of the Royal Society of London. Series A. Mathematical and Physical Sciences, 1957. **241**(1226): p. 376-396.

77. Hill, R., *A self-consistent mechanics of composite materials.* Journal of the Mechanics and Physics of Solids, 1965. **13**(4): p. 213-222.

78. Budiansky, B., *On the elastic moduli of some heterogeneous materials.* Journal of the Mechanics and Physics of Solids, 1965. **13**(4): p. 223-227.

79. Mori, T. and K. Tanaka, *Average stress in matrix and average elastic energy of materials with misfitting inclusions.* Acta Metallurgica, 1973. **21**(5): p. 571-574.
80. Benveniste, Y., *A new approach to the application of Mori-Tanaka's theory in composite materials.* Mechanics of Materials, 1987. **6**(2): p. 147-157.
81. Reiter, T., G.J. Dvorak, and V. Tvergaard, *Micromechanical models for graded composite materials.* Journal of the Mechanics and Physics of Solids, 1997. **45**(8): p. 1281-1302.
82. Kou, X.Y., G.T. Parks, and S.T. Tan, *Optimal design of functionally graded materials using a procedural model and particle swarm optimization.* Computer-Aided Design, 2012. **44**(4): p. 300-310.
83. Reddy, J.N., *Analysis of functionally graded plates.* International Journal for Numerical Methods in Engineering, 2000. **47**(1-3): p. 663-684.
84. Kim, J. and J.N. Reddy, *A general third-order theory of functionally graded plates with modified couple stress effect and the von Kármán nonlinearity: theory and finite element analysis.* Acta Mechanica, 2015. **226**(9): p. 2973-2998.
85. Kant, T., D.K. Jha, and R.K. Singh, *A higher-order shear and normal deformation functionally graded plate model: some recent results.* Acta Mechanica, 2014. **225**(10): p. 2865-2876.
86. Apetre, N.A., B.V. Sankar, and D.R. Ambur, *Low-velocity impact response of sandwich beams with functionally graded core.* International Journal of Solids and Structures, 2006. **43**(9): p. 2479-2496.
87. Hao, Y.X., W. Zhang, and X.L. Ji, *Nonlinear Dynamic Response of Functionally Graded Rectangular Plates under Different Internal Resonances.* Mathematical Problems in Engineering, 2010. **2010**: p. 12.
88. Anlas, G., M. Santare, and J. Lambros, *Numerical calculation of stress intensity factors in functionally graded materials.* International Journal of Fracture, 2000. **104**(2): p. 131-143.
89. Kim, J.-H. and G.H. Paulino, *Finite element evaluation of mixed mode stress intensity factors in functionally graded materials.* International Journal for Numerical Methods in Engineering, 2002. **53**(8): p. 1903-1935.
90. Santare, M. and J. Lambros, *Use of graded finite elements to model the behavior of nonhomogeneous materials.* TRANSACTIONS-AMERICAN SOCIETY OF MECHANICAL ENGINEERS JOURNAL OF APPLIED MECHANICS, 2000. **67**(4): p. 819-822.

91. Chen, Z. and M. Negahban, *Avoiding negative elastic moduli when using Lagrange interpolation for material grading in finite element analysis.* Acta Mechanica, 2015: p. 1-14.

92. Kim, J.-H. and G. Paulino, *Isoparametric graded finite elements for nonhomogeneous isotropic and orthotropic materials.* Journal of Applied Mechanics, 2002. **69**(4): p. 502-514.

93. Kubair, D. and B. Bhanu-Chandar, *Stress concentration factor due to a circular hole in functionally graded panels under uniaxial tension.* International journal of mechanical sciences, 2008. **50**(4): p. 732-742.

94. Asemi, K., H. Ashrafi, M. Salehi, and M. Shariyat, *Three-dimensional static and dynamic analysis of functionally graded elliptical plates, employing graded finite elements.* Acta Mechanica, 2013. **224**(8): p. 1849-1864.

95. Cho, J. and D. Ha, *Volume fraction optimization for minimizing thermal stress in Ni–Al 2 O 3 functionally graded materials.* Materials Science and Engineering: A, 2002. **334**(1): p. 147-155.

96. Goupee, A.J. and S.S. Vel, *Two-dimensional optimization of material composition of functionally graded materials using meshless analyses and a genetic algorithm.* Computer methods in applied mechanics and engineering, 2006. **195**(44): p. 5926-5948.

97. Hassanzadeh Taheri, A. and B. Hassani, *Thermo-elastic optimization of material distribution of functionally graded structures by an isogeometrical approach.* International Journal of Solids and Structures, 2013. **51**.

98. Kou, X., G. Parks, and S. Tan, *Optimal design of functionally graded materials using a procedural model and particle swarm optimization.* Computer-Aided Design, 2012. **44**(4): p. 300-310.

99. Carvalho, O., M. Buciumeanu, S. Madeira, D. Soares, F.S. Silva, and G. Miranda, *Optimization of AlSi–CNTs functionally graded material composites for engine piston rings.* Materials & Design, 2015. **80**: p. 163-173.

100. Arsha, A.G., E. Jayakumar, T.P.D. Rajan, V. Antony, and B.C. Pai, *Design and fabrication of functionally graded in-situ aluminium composites for automotive pistons.* Materials & Design, 2015. **88**: p. 1201-1209.

101. Huang, C.-Y. and Y.-L. Chen, *Design and impact resistant analysis of functionally graded Al2O3–ZrO2 ceramic composite.* Materials & Design, 2016. **91**: p. 294-305.

102. Brodlie, K., P. Mashwama, and S. Butt, *Visualization of surface data to preserve positivity and other simple constraints.* Computers & graphics, 1995. **19**(4): p. 585-594.

103. Park, C.-H., S.-W. Lee, J.-W. Park, and H.-J. Kim, *Preparation and characterization of dual curable adhesives containing epoxy and acrylate functionalities.* Reactive and Functional Polymers, 2013. **73**(4): p. 641-646.

104. Chen, F. and W.D. Cook, *Curing kinetics and morphology of IPNs from a flexible dimethacrylate and a rigid epoxy via sequential photo and thermal polymerization.* European Polymer Journal, 2008. **44**(6): p. 1796-1813.

105. Butterfield, L.R., *Developing and Characterizing a Rapid Prototyping Stereo-Lithography Machine to Produce Interpenetrating Polymer Network Systems*. 2013, University of Nebraska-Lincoln.

106. Butterfield, L., E. Bobo, W. Li, S. Henning, N. Delpouve, L. Tan, J.-M. Saiter, and M. Negahban, *Morphology and thermomechanical properties in epoxy acrylate interpenetrated networks.* Under review, 2016.

107. Berryman, J.G., *Long-wavelength propagation in composite elastic media II. Ellipsoidal inclusions.* The Journal of the Acoustical Society of America, 1980. **68**(6): p. 1820-1831.

108. Goupee, A.J. and S.S. Vel, *Multi-objective optimization of functionally graded materials with temperature-dependent material properties.* Materials & Design, 2007. **28**(6): p. 1861-1879.

109. Negahban, M., *The Mechanical and Thermodynamical Theory of Plasticity*. 2012: CRC Press.

110. Negahban, M., A. Goel, P. Marchon, and A. Azizinamini, *Geometrically Exact Nonlinear Extended-Reissner/Mindlin Shells: Fundamentals, Finite Element Formulation, Elasticity.* International Journal for Computational Methods in Engineering Science and Mechanics, 2009. **10**(6): p. 430-449.

111. Matsui, K. and K. Terada, *Continuous approximation of material distribution for topology optimization.* International Journal for Numerical Methods in Engineering, 2004. **59**(14): p. 1925-1944.

112. King, D.E., *Dlib-ml: A machine learning toolkit.* The Journal of Machine Learning Research, 2009. **10**: p. 1755-1758.

113. Powell, M.J., *The BOBYQA algorithm for bound constrained optimization without derivatives.* Cambridge NA Report NA2009/06, University of Cambridge, Cambridge, 2009.

114. Kirsch, G., *Die theorie der elastizität und die bedürfnisse der festigkeitslehre*. 1898: Springer.

115. Long, X. and F. Delale, *The mixed mode crack problem in an FGM layer bonded to a homogeneous half-plane.* International Journal of Solids and Structures, 2005. **42**(13): p. 3897-3917.

116. Huang, C.S. and M.J. Chang, *Corner stress singularities in an FGM thin plate.* International Journal of Solids and Structures, 2007. **44**(9): p. 2802-2819.

117. Ghajar, R., A. Shaghaghi Moghaddam, and M. Alfano, *An improved numerical method for computation of stress intensity factors along 3D curved non-planar cracks in FGMs.* International Journal of Solids and Structures, 2011. **48**(1): p. 208-216.

118. Papila, M. and R.T. Haftka, *Implementation of a crack propagation constraint within a structural optimization software.* Structural and Multidisciplinary Optimization, 2003. **25**(5): p. 327-338.

119. Lellep, J. and E. Puman, *Optimization of inelastic conical shells with cracks.* Structural and Multidisciplinary Optimization, 2006. **33**(3): p. 189-197.

120. Challis, V.J., A.P. Roberts, and A.H. Wilkins, *Fracture resistance via topology optimization.* Structural and Multidisciplinary Optimization, 2007. **36**(3): p. 263-271.

121. Peng, D. and R. Jones, *A CAD-based on biological method for designing optimal fatigue life.* Structural and Multidisciplinary Optimization, 2008. **37**(3): p. 295-304.

122. Kim, G.W. and K.Y. Lee, *Applying material optimization to fracture mechanics analysis to improve the reliability of the plastic IC package in reflow soldering process.* IEEE Transactions on Components and Packaging Technologies, 2006. **29**(1): p. 47-53.

123. Bird, S.A., D. Clary, K.C. Jajam, H.V. Tippur, and M.L. Auad, *Synthesis and characterization of high performance, transparent interpenetrating polymer networks with polyurethane and poly(methyl methacrylate).* Polymer Engineering & Science, 2013. **53**(4): p. 716-723.

124. Jajam, K.C., S.A. Bird, M.L. Auad, and H.V. Tippur, *Tensile, fracture and impact behavior of transparent Interpenetrating Polymer Networks with polyurethane-poly(methyl methacrylate).* Polymer Testing, 2013. **32**(5): p. 889-900.

125. Tracey, D.M., *Finite elements for determination of crack tip elastic stress intensity factors.* Engineering Fracture Mechanics, 1971. **3**(3): p. 255-265.

126. Erdogan, F. and G.C. Sih, *On the Crack Extension in Plates Under Plane Loading and Transverse Shear.* Journal of Basic Engineering, 1963. **85**(4): p. 519-525.

127. Eischen, J.W., *Fracture of nonhomogeneous materials.* International Journal of Fracture, 1987. **34**(1): p. 3-22.

128. Williams, M.L., *On the stress distribution at the base of a stationary crack.* Journal of Applied Mechanics, 1957. **24**: p. 109-114.

129. Eftis, J., N. Subramonian, and H. Liebowitz, *Crack border stress and displacement equations revisited.* Engineering Fracture Mechanics, 1977. **9**(1): p. 189-210.

130. Rybicki, E.F. and M.F. Kanninen, *A finite element calculation of stress intensity factors by a modified crack closure integral.* Engineering Fracture Mechanics, 1977. **9**(4): p. 931-938.

131. Hussain, M.A., S.L. Pu, J.H. Underwood, and W. Arsenal, *Strain Energy Release Rate for a Crack Under Combined Mode I and Mode II*. Vol. 560. 1973, ASTM STP: Defense Technical Information Center.

132. Sih, G.C., *Strain-energy-density factor applied to mixed mode crack problems.* International Journal of Fracture, 1974. **10**(3): p. 305-321.

133. Barenblatt, G.I., *The Mathematical Theory of Equilibrium Cracks in Brittle Fracture*, in *Advances in Applied Mechanics*, T.v.K.G.K.F.H.v.d.D. H.L. Dryden and L. Howarth, Editors. 1962, Elsevier. p. 55-129.

134. Erdogan, F. and B.H. Wu, *The Surface Crack Problem for a Plate With Functionally Graded Properties.* Journal of Applied Mechanics, 1997. **64**(3): p. 449-456.

135. Konda, N. and F. Erdogan, *The mixed mode crack problem in a nonhomogeneous elastic medium.* Engineering Fracture Mechanics, 1994. **47**(4): p. 533-545.